



ΠΑΝΕΠΙΣΤΗΜΙΟ ΙΩΑΝΝΙΝΩΝ  
ΣΧΟΛΗ ΘΕΤΙΚΩΝ ΕΠΙΣΤΗΜΩΝ  
ΤΜΗΜΑ ΦΥΣΙΚΗΣ



---

Ελαστική σκέδαση και μηχανισμοί  
αντιδράσεων κοντά στο φράγμα  
Coulomb για το σύστημα  ${}^7\text{Be} + {}^{28}\text{Si}$

---

*Συγγραφέας:*

Ονούφριος Σγούρος

*Επιβλέπουσα:*

Καθηγήτρια Αθηνά Πάκου

ΔΙΔΑΚΤΟΡΙΚΗ ΔΙΑΤΡΙΒΗ

ΙΩΑΝΝΙΝΑ 2017





UNIVERSITY OF IOANNINA  
SCHOOL OF NATURAL SCIENCE  
PHYSICS DEPARTMENT



---

Elastic scattering and reaction  
mechanisms for the system  ${}^7\text{Be} + {}^{28}\text{Si}$  at  
near barrier energies

---

*Author:*

Onoufrios Sgouros

*Supervisor:*

Prof. Athina Pakou

PHD THESIS

IOANNINA 2017



## **Advisory committee:**

1. Athina Pakou (Supervisor)  
Emeritus Professor  
Physics Department  
University of Ioannina
2. Nicolas Alamanos  
Professor  
Deputy Director of IRFU  
Research Director at CEA-SACLAY  
France
3. Efstathios Stiliaris  
Associate Professor  
Physics Department  
University of Athens

## **Review committee:**

1. Athina Pakou: Emeritus Professor - Physics Department - University of Ioannina
2. Nicolas Alamanos: Professor - Deputy Director of IRFU - Research Director at CEA-SACLAY, France
3. Efstathios Stiliaris: Associate Professor - Physics Department - University of Athens
4. Dimitra Pierroutsakou: Senior Researcher - INFN Napoli, Italy
5. Nicholas Keeley: Associate Professor - NCBJ, Poland
6. Nikolaos Nicolis: Associate Professor - Physics Department - University of Ioannina
7. Nikolaos Patronis: Assistant Professor - Physics Department - University of Ioannina

**ΠΡΑΚΤΙΚΟ ΠΑΡΟΥΣΙΑΣΗΣ, ΕΞΕΤΑΣΗΣ  
ΚΑΙ ΑΞΙΟΛΟΓΗΣΗΣ ΔΙΔΑΚΤΟΡΙΚΗΣ ΔΙΑΤΡΙΒΗΣ**

Σήμερα Πέμπτη 4 Μαΐου 2017, ώρα 9:00, στην αίθουσα σεμιναρίων του Τμήματος Φυσικής του Πανεπιστημίου Ιωαννίνων, πραγματοποιήθηκε σύμφωνα με το άρθρο 12, παρ. 5 του Ν.2083/92 η διαδικασία της δημόσιας παρουσίασης, εξέτασης και αξιολόγησης της διδακτορικής διατριβής του υποψηφίου διδάκτορα κ. Ονουφρίου Σγούρου.

Την Επταμελή Εξεταστική Επιτροπή, που συγκροτήθηκε με απόφαση της Γενικής Συνέλευσης Ειδικής Σύνοψης του Τμήματος Φυσικής (συν. 477/10-2-2017) αποτελούν τα κάτωθι μέλη :

1. Αθηνά Πάκου-Ομότιμη Καθηγήτρια - Τμήμα Φυσικής, Πανεπιστήμιο - Ιωαννίνων (Επιβλέπουσα Καθηγήτρια)
2. Nicolas Alamanos-Professor-Deputy Director of IRFU-Research Director at CEA -SACLAY-France
3. Ευστάθιος Στυλιάρης-Αναπληρωτής Καθηγητής-Τμήμα Φυσικής-ΕΚΠΑ
4. Nicholas Keeley-Associate Professor- NCBJ, Poland
5. Dimitra Pierrotsakou-Senior Researcher- INFN Napoli-Italy
6. Νικόλαος Νικολής- Αναπληρωτής Καθηγητής-Τμήμα Φυσικής-Πανεπιστήμιο Ιωαννίνων
7. Νικόλαος Πατρώνης-Επίκουρος Καθηγητής- Τμήμα Φυσικής-Πανεπιστήμιο Ιωαννίνων

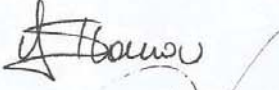
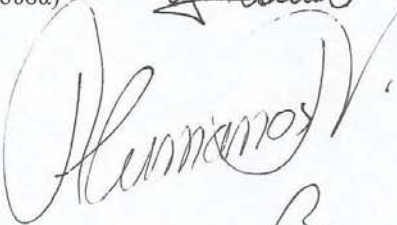
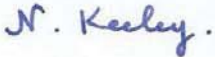
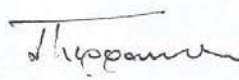
Παρόντα ήταν τα 6 μέλη της εξεταστικής επιτροπής επειδή ο κ. Ν. Νικολής απουσιάζει με εκπαιδευτική άδεια. Το θέμα της διδακτορικής διατριβής που εκπόνησε ο κ. Σγούρος και παρουσίασε σήμερα είναι : 'Ελαστική Σκέδαση και μηχανισμοί αντιδράσεων κοντά στο φράγμα Coulomb για το σύστημα  ${}^7\text{Be}+{}^{28}\text{Si}$ '

Ο Υποψήφιος αφού παρουσίασε διεξοδικά το θέμα, απάντησε σε ερωτήσεις των μελών της επιτροπής και του ακροατηρίου. Στη συνέχεια η επιτροπή αποσύρθηκε και μετά από εκτεταμένη συζήτηση στην οποία εκφράστηκαν από όλα τα μέλη εξαιρετικοί έπαινοι τόσο για τη διατριβή όσο και για τον υποψήφιο κατέληξε στα ακόλουθα

1. Το περιεχόμενο της διατριβής είναι πρωτότυπο, υψηλής ποιότητας και αποτελεί ουσιαστική συμβολή στην επιστήμη. Από την εργασία αυτή έχουν προκύψει δύο δημοσιευμένες εργασίες σε έγκριτα περιοδικά που έγιναν από τον υποψήφιο, ενώ υπήρξε ουσιαστική συμμετοχή του και σε άλλες δώδεκα δημοσιευμένες εργασίες.
2. Η παρουσίαση και ανάπτυξη του θέματος της διατριβής από τον υποψήφιο και οι απαντήσεις στις ερωτήσεις που του τέθηκαν έδειξαν την ωριμότητα του υποψηφίου και την εξαιρετική κατάρτιση του τόσο στα σχετικά πειραματικά θέματα όσο και στη θεωρία.

Με βάση τα ανωτέρω η επιτροπή εγκρίνει ομόφωνα την εργασία και εισηγείται θερμά και ανεπιφύλακτα την απονομή Διδακτορικού Διπλώματος στον κ. **Ονούφριο Σγούρο** με βαθμό **Άριστα**

Το πρακτικό αυτό συντάχθηκε την ίδια μέρα και υπογράφεται από τα μέλη της Εξεταστικής Επιτροπής.

1. Αθηνά Πάκου (Επιβλέπουσα) 
2. Nicolas Alamanos 
3. Ευστάθιος Στυλιάρης 
4. Nicolas Keeley 
5. Dimitra Pierroutsakou 
6. Νικόλαος Νικολής 
7. Νικόλαος Πατρώνης 



*To my parents*  
Giorgo and Maria



# Contents

|   |           |
|---|-----------|
| Acknowledgements . . . . .  | 1         |
| Εκτεταμένη Περίληψη . . . . .                                       | 3         |
| Abstract . . . . .  | 9         |
| Introduction . . . . .  | 13        |
| <b>1 Theory</b>   | <b>19</b> |
| 1.1 Elastic Scattering . . . . .                                    | 19        |
| 1.1.1 Scattering by a short range central potential . . . . .       | 20        |
| 1.1.2 Continuum Discretized Coupled Channels Calculations . . . . . | 23        |
| 1.1.3 Optical Model . . . . .                                       | 27        |
| 1.1.4 Threshold Anomaly and Dispersion Relations . . . . .          | 31        |
| 1.2 Reaction Mechanisms . . . . .                                   | 32        |
| 1.2.1 Direct Reactions . . . . .                                    | 33        |
| 1.2.2 Compound Nucleus Reactions . . . . .                          | 40        |
| <b>2 Experimental Details</b>                                       | <b>45</b> |
| 2.1 The EXOTIC facility . . . . .                                   | 45        |
| 2.1.1 The dipole . . . . .  | 46        |
| 2.1.2 The Wien filter . . . . .                                     | 47        |
| 2.2 Detection systems and electronics . . . . .                     | 48        |
| 2.2.1 Silicon detectors . . . . .                                   | 49        |

|          |  |            |
|----------|--|------------|
| 2.2.2    | Parallel Plate Avalanche Counters . . . . .                        | 49         |
| 2.2.3    | Double Sided Silicon Strip Detectors (DSSSD) and the EXPADES array | 53         |
| 2.2.4    | The trigger of the experiment . . . . .                            | 56         |
| 2.3      | Experimental setup and procedure . . . . .                         | 56         |
| <b>3</b> | <b>Data Reduction</b>  | <b>61</b>  |
| 3.1      | Energy calibration . . . . .                                       | 61         |
| 3.2      | Determination of the elastic scattering cross sections . . . . .   | 63         |
| 3.3      | Determination of the reaction cross sections . . . . .             | 67         |
| 3.3.1    | $\alpha$ - particle production cross sections . . . . .            | 68         |
| 3.3.2    | $^3\text{He}$ production cross sections . . . . .                  | 70         |
| <b>4</b> | <b>Theoretical Analysis</b>  | <b>77</b>  |
| 4.1      | Elastic Scattering . . . . .                                       | 77         |
| 4.1.1    | Optical Model Analysis . . . . .                                   | 77         |
| 4.1.2    | Energy evolution of the optical potential parameters . . . . .     | 81         |
| 4.1.3    | Total reaction cross sections . . . . .                            | 82         |
| 4.1.4    | Continuum Discretized Coupled Channels Calculations . . . . .      | 86         |
| 4.2      | Reaction Mechanisms . . . . .                                      | 91         |
| 4.2.1    | Fusion Cross Sections . . . . .                                    | 91         |
| 4.2.2    | Direct Reactions Cross Sections . . . . .                          | 97         |
| 4.2.3    | DWBA Calculations . . . . .  | 99         |
| <b>5</b> | <b>Conclusions - Summary</b>                                       | <b>105</b> |
|          | <b>References</b>  | <b>109</b> |
| <b>A</b> | <b>Event by event analysis code</b>                                | <b>119</b> |
| <b>B</b> | <b>Simulation Code</b>   | <b>123</b> |

|   |                            |     |
|---|----------------------------|-----|
| C | Tabulated cross sections   | 127 |
| D | Error calculation formulas | 133 |
| E | $\Delta E$ -E technique    | 137 |



# Acknowledgements

I would like to thank all of those who have supported and assisted me during my PhD studies.

First of all, I would like to express my sincere gratitude to Professor of Nuclear Physics Athina Pakou, my supervisor, for her precious guidance and help throughout my studies, for proposing the subject of my PhD thesis and for supporting my efforts during my studies. I feel honored for being a student of Professor A. Pakou all these years, starting with my undergraduate diploma thesis until my PhD studies, where she generously shared her knowledge by introducing me to the appropriate experimental and theoretical techniques, necessary in the Nuclear Physics field, while she still keeps motivating me to bring the best out of myself.

Also, I would like to express my sincere thanks to the members of the advisory committee, Professor Nicolas Alamanos and Associate Professor Efstathios Stiliaris for the generous assistance they provided.

I would like also to thank the EXOTIC group for their substantial contribution during the experiment and in particular Prof. Cosimo Signorini and the head of the EXOTIC group Dr. Dimitra Pierroutsakou for hosting this experiment and for making available the EXOTIC facility, Dr. Marco Mazzocco who was responsible for the production of the secondary  $^7\text{Be}$  radioactive beam and Dr. Alfonso Boiano and Dr. Ciro Boiano for setting up the electronic chain of the experiment and for their continuous assistance with the emerging problems in the electronics during the experiment. Also, I would like to thank Assoc. Prof. Marco La Commara, Dr. Tina Parascandolo, Dr. Emanuele Strano, Dr. Domenico Torresi and all the rest of the participants for their unreserved assistance during the experiment.

I would like to extend my sincere and warm thanks to Professor Krzysztof Rusek and Associate Professor Nicholas Keeley for the theoretical support and in particular, for introducing me to the CDCC calculations with the code FRESCO during an one week seminar in Warsaw. Working with them has been a very profitable experience. Also, I would like to thank Professor Krzysztof Rusek for his generous hospitality in the dormitories of the Heavy Ion Laboratory during my staying in Warsaw. I could not omit the Associate Professor Nikolaos Nicolis from the Nuclear Physics Laboratory of the University of Ioannina, who provided the theoretical support regarding the compound nucleus calculations, performed via code PACE2.

Also, I would like to thank Associate Professor Efstathios Stiliaris and his group for introducing me to Geant simulations using the program GATE .

Moreover, I am grateful to Dr. Ángel Miguel Sánchez-Benítez and Dr. Gloria Marquínez-Durán for their help regarding the pixel analysis.

I would like to extend my sincere thanks to Prof. Francesco Cappuzzello who provided me the opportunity to get familiar with the analysis of experimental data acquired with the MAGNEX spectrometer in conjunction with the neutron detector array EDEN, during a three-month ERASMUS traineeship in Catania (LNS). Collaborating with him and his group helped me to broaden further my skills from various perspectives.

Furthermore, I would like to thank my fellow team members Dr. Konstantina Zerva and Ms. Chrysoula Betsou for their collaborative and friendly spirit but especially my friend and fellow worker Dr. Vasileio Soukera for the thoughtful discussions not only in the field of Physics and for being a nice company at the office all these years.

In addition, I would like to thank the members of the review committee for reading carefully this manuscript and for the insightful comments/corrections they made.

Last but not least, I would like to thank my family, my parents Giorgio and Maria and my brother Gianni but especially my parents, for supporting my efforts all these years and never stopped to have faith on me.

## Εκτεταμένη Περίληψη

Η παρούσα διδακτορική διατριβή αφορά τη μελέτη της ελαστικής σκέδασης και των μηχανισμών αντιδράσεων για το σύστημα  ${}^7\text{Be} + {}^{28}\text{Si}$  σε ενέργειες κοντά στο φράγμα Coulomb και συγκεκριμένα στα 13.2, 17.2, 19.8 και 22.0 MeV ( $E/V_{C.b.} = 1.14, 1.48, 1.71, 1.90$ ). Στόχος της παρούσας μελέτης είναι ο προσδιορισμός της ενεργειακής εξάρτησης του οπτικού δυναμικού καθώς και ο προσδιορισμός της συνεισφοράς των άμεσων αντιδράσεων και των αντιδράσεων σύνθετου πυρήνα στην αντίδραση  ${}^7\text{Be} + {}^{28}\text{Si}$ . Το πειραματικό μέρος της μελέτης αυτής πραγματοποιήθηκε στην γραμμή EXOTIC του Εθνικού Εργαστηρίου του Legnaro (INFN-LNL) της Ιταλίας. Η ραδιενεργή δέσμη  ${}^7\text{Be}$  παρήχθη μέσω της τεχνικής “in-flight” χρησιμοποιώντας την αντίδραση  ${}^1\text{H}({}^7\text{Li}, {}^7\text{Be})n$ , όπου η πρωτογενής δέσμη  ${}^7\text{Li}$  εντάσεως (100-150)pnA προσέπιπτε σε ένα στόχο αερίου υδρογόνου. Η δευτερογενώς παραγόμενη δέσμη  ${}^7\text{Be}$  διαχωρίστηκε από τα πιθανά υπολείμματα της πρωτογενούς δέσμης  ${}^7\text{Li}$  μέσω της συνδυασμένης δράσης ενός μαγνητικού διπόλου και ενός φίλτρου ταχυτήτων (Wien filter). Στο παρών πείραμα, για την κύρια μέτρηση χρησιμοποιήθηκαν στόχοι πυριτίου ( ${}^{28}\text{Si}$ ) πάχους 400 και 600 μικρογραμμάρων ανά τετραγωνικό εκατοστό καθώς και ένας στόχος μολύβδου ( ${}^{208}\text{Pb}$ ) πάχους 2000 μικρογραμμάρων ανά τετραγωνικό εκατοστό για την μέτρηση που αφορά στον προσδιορισμό της στερεάς γωνίας των ανιχνευτών. Τα διάφορα προϊόντα της αντίδρασης  ${}^7\text{Be} + {}^{28}\text{Si}$  ανιχνεύτηκαν χρησιμοποιώντας έξι ΔΕ-Ε τηλεσκόπια από την ανιχνευτική διάταξη EXPADES. Τα τηλεσκόπια είχαν τοποθετηθεί στο θάλαμο σκέδασης σε συμμετρικές θέσεις γύρω από το στόχο για τον έλεγχο της συμμετρίας της δέσμης. Το πρώτο μέρος του κάθε τηλεσκοπίου αποτελούνταν από έναν μικρολωριδιακό ανιχνευτή πυριτίου διπλής όψεως (DSSSD) πάχους (40-60) μικρομέτρων, ενώ το δεύτερο μέρος του τηλεσκοπίου ήταν ένας ίδιου τύπου ανιχνευτής πάχους 300 μικρομέτρων. Επίσης, η πειραματική μας διάταξη περιελάμβανε δύο πολυσυρματικούς ανιχνευτές αερίου (PPAC's) που χρησιμοποιήθηκαν για τον έλεγχο του προφίλ της δέσμης κατά τη διάρκεια των μετρήσεων καθώς επίσης παρείχαν και την απαραίτητη πληροφορία για την ανακατασκευή των τροχιών των σωματιδίων της προσπίπτουσας στο στόχο δέσμης αλλά και των τροχιών των σχεδάζομενων σωματιδίων.

Η ανάλυση των δεδομένων της ελαστικής σκέδασης πραγματοποιήθηκε με την τεχνική event by event με τη χρήση ενός κώδικα σε γλώσσα προγραμματισμού C και του πακέτου ανάλυσης δεδομένων ROOT. Ο κώδικας αυτός χρησιμοποιεί την πληροφορία που παρέχεται από τους ανιχνευτές αερίου καθώς και από τα ΔΕ-Ε τηλεσκόπια, προκειμένου να προσδιορίσουμε τις συντεταγμένες της προσπίπτουσας δέσμης στο στόχο καθώς και τις συντεταγμένες των μικρολωριδιακών ανιχνευτών στους οποίους ανιχνεύονται τα ελαστικώς σχεδάζομενα σωματάρια  ${}^7\text{Be}$ . Ως εκ τούτου, μπορούμε να προσδιορίσουμε με μεγαλύτερη ακρίβεια την γωνία της ελαστικής σκέδασης για κάθε γεγονός (Παράρτημα Α). Εν συνεχεία, ο κώδικας αθροίζει τα γεγονότα που σχεδιάζονται

στην ίδια γωνία ή μέσα σε ένα γωνιακό εύρος που αντιστοιχεί στις διαστάσεις ενός μικρολωριδικού ανιχνευτή. Η διαδικασία αυτή πραγματοποιείται για τη σκέδαση των πυρήνων  ${}^7\text{Be}$  από τους στόχους πυριτίου και μολύβδου και κατόπιν προσδιορίζονται οι διαφορικές ενεργές διατομές.

Η ανάλυση των γωνιακών κατανομών της ελαστικής σκέδασης έγινε στα πλαίσια του Οπτικού Μοντέλου με τη χρήση του υπολογιστικού κώδικα ECIS ακολουθώντας την ίδια τεχνική όπως είχε εφαρμοστεί για τα συστήματα  ${}^6,7\text{Li} + {}^{28}\text{Si}$ . Το πραγματικό μέρος του οπτικού δυναμικού περιγράφηκε υιοθετώντας την μικροσκοπική BDM3Y1 αλληλεπίδραση. Κάνοντας την υπόθεση ότι το φανταστικό μέρος του οπτικού δυναμικού παρουσιάζει την ίδια ακτινική εξάρτηση με το αντίστοιχο πραγματικό μέρος, για την περιγραφή του φανταστικού μέρους του οπτικού δυναμικού υιοθετήθηκε η ίδια μικροσκοπική αλληλεπίδραση όπως στην περίπτωση του πραγματικού μέρους αλλά χρησιμοποιώντας ένα διαφορετικό παράγοντα νορμαλισμού. Οι παράγοντες νορμαλισμού του πραγματικού και του φανταστικού μέρους του οπτικού δυναμικού προσδιορίστηκαν στις διάφορες ενέργειες από την προσαρμογή των θεωρητικών κατανομών στα πειραματικά δεδομένα. Δεδομένης της μεγάλης αβεβαιότητας στον προσδιορισμό των προαναφερθέντων παραγόντων, δεν ήταν εφικτό να προβούμε σε ασφαλή συμπεράσματα μόνο βάσει των αποτελεσμάτων της ελαστικής σκέδασης παρά μόνο σε συνδυασμό με τα αποτελέσματα της ανάλυσης των δεδομένων της παραγωγής σωματίων άλφα. Το φανταστικό μέρος του οπτικού δυναμικού όπως προσδιορίστηκε από την ανάλυση των δεδομένων της ελαστικής σκέδασης, παρουσιάζει μια πτωτική τάση καθώς προσεγγίζουμε το φράγμα Coulomb με κατεύθυνση από τις μεγαλύτερες προς τις μικρότερες ενέργειες, μια συμπεριφορά συμβατή με την τυπική ανωμαλία κατωφλίου όπως αυτή συναντάται στην σκέδαση των σταθερών πυρήνων. Όσον αφορά το πραγματικό μέρος του οπτικού δυναμικού, δεν μπορούμε να πούμε με βεβαιότητα ότι συνδέεται με το αντίστοιχο φανταστικό μέρος μέσω των σχέσεων διασποράς καθώς στην περιοχή γύρω από το φράγμα Coulomb, όπου με βάση τις σχέσεις διασποράς αναμένεται μια αύξηση στο μέτρο του πραγματικού δυναμικού, διαθέτουμε μόλις ένα πειραματικό σημείο. Από την άλλη, αν λάβουμε υπ' όψιν μας τα αντίστοιχα πειραματικά αποτελέσματα για τα συστήματα  ${}^6,7\text{Li} + {}^{28}\text{Si}$ , τα οποία αναλύθηκαν με την ίδια μέθοδο όπως τα δεδομένα του υπό μελέτη συστήματος, μπορούμε να πούμε ότι το οπτικό δυναμικό των δυο κατοπτρικών πυρήνων  ${}^7\text{Be}$ ,  ${}^7\text{Li}$  παρουσιάζει την ίδια ενεργειακή εξάρτηση. Συνδυάζοντας το αποτέλεσμα αυτό με τα αποτελέσματα της ανάλυσης των δεδομένων της παραγωγής σωματίων άλφα, μπορούμε να πούμε με κάποια βεβαιότητα ότι ο πυρήνας  ${}^7\text{Be}$  συμπεριφέρεται όπως ο κατοπτρικός του πυρήνας  ${}^7\text{Li}$  και όχι όπως ο πυρήνας του  ${}^6\text{Li}$ .

Η ανάλυση των δεδομένων της ελαστικής σκέδασης υπό το πρίσμα του Οπτικού Μοντέλου, οδήγησε και στον προσδιορισμό της ολικής ενεργού διατομής της αντίδρασης για τις 4 ενέργειες. Οι τιμές αυτές βρέθηκαν να είναι σε εξαιρετική συμφωνία με τις αντίστοιχες τιμές όπως αυτές

προσδιορίστηκαν από την ανάλυση των σωματίων  $^{3,4}\text{He}$ , με τις τιμές που προβλέπονται από ένα φαινομενολογικό μοντέλο καθώς και με τις τιμές όπως προέκυψαν από τους CDCC υπολογισμούς οι οποίοι λαμβάνουν υπ' όψιν την σύζευξη του ελαστικού καναλιού με τις καταστάσεις του συνεχούς. Οι CDCC υπολογισμοί πραγματοποιήθηκαν με τη χρήση του υπολογιστικού κώδικα FRESCO από τους οποίους και συμπεραίνουμε ότι η επίδραση της σύζευξης του ελαστικού καναλιού με την βασική και την πρώτη διεγερμένη κατάσταση του  $^7\text{Be}$  είναι ασθενής. Παρότι οι CDCC υπολογισμοί προβλέπουν πολύ μικρή ολική ενεργό διατομή για την αντίδραση διάσπασης, η επίδραση της σύζευξης του ελαστικού καναλιού με τις καταστάσεις του συνεχούς βρέθηκε να είναι σημαντική αλλά όχι πάρα πολύ ισχυρή. Τέλος, όσον αφορά τις τιμές της ολικής ενεργού διατομής της αντίδρασης, η πολύ καλή συμφωνία με τις προβλεπόμενες τιμές ενός φαινομενολογικού μοντέλου καθώς και με τις υπολογιζόμενες τιμές όπως προκύπτουν από τους CDCC υπολογισμούς, ενισχύουν την εγκυρότητα των μετρήσεων μας. Επίσης ενισχύει περαιτέρω τα αποτελέσματα που αφορούν στην ενεργειακή εξάρτηση του οπτικού δυναμικού, καθώς η ολική ενεργός διατομή της αντίδρασης χρησιμοποιείται σαν ένα μέγεθος για τον περιορισμό του μέτρου του φανταστικού μέρους του οπτικού δυναμικού.

Όσον αφορά τους μηχανισμούς αντιδράσεων, η ανάλυση των σχετικών δεδομένων αφορά στην παραγωγή των ελαφρών σωματίων  $^{3,4}\text{He}$  είτε μέσω άμεσων αντιδράσεων είτε μέσω αντιδράσεων σύνθετου πυρήνα. Σε αντίθεση με τους πυρήνες  $^7\text{Be}$ , τα δύο αυτά ελαφρά ιόντα μπορούν και περνούν στο δεύτερο μέρος του τηλεσκοπίου και γι' αυτό ο διαχωρισμός τους έγινε με βάση τη γνωστή ΔΕ-Ε τεχνική. Ο αριθμός των γεγονότων  $^{3,4}\text{He}$  προσδιορίστηκε από την ανάλυση των δισδιάστατων φασμάτων ΔΕ-Ε. Παρόλα αυτά, λόγω του πεπερασμένου πάχους των ΔΕ ανιχνευτών, υπεισέρχεται ένα ενεργειακό κατώφλι στην ανίχνευση των δύο αυτών ιόντων. Τα γεγονότα τα οποία σταματούν στο πρώτο μέρος του τηλεσκοπίου ανακτήθηκαν από την σύγκριση των πειραματικών ενεργειακών φασμάτων με τα αντίστοιχα φάσματα που προέκυψαν από προσομοιώσεις. Η προσομοίωση των φασμάτων για τα γεγονότα που προέρχονται από διεργασίες σύνθετου πυρήνα έγινε μέσω του κώδικα PACE2. Η προσομοίωση των φασμάτων για τα γεγονότα που προέρχονται από άμεσες αντιδράσεις έγιναν μέσω ενός Monte Carlo κώδικα που αναπτύχθηκε για τις ανάγκες της παρούσας εργασίας (Παράρτημα Β). Μετά την ανάκτηση των γεγονότων που σταματούν στο πρώτο μέρος του τηλεσκοπίου, υπολογίστηκαν οι διαφορικές ενεργές διατομές για την παραγωγή σωματίων  $^{3,4}\text{He}$ .

Η ενεργός διατομή για την παραγωγή σωματίων άλφα μέσω διεργασιών σύνθετου πυρήνα εκτιμήθηκε από την προσαρμογή των θεωρητικών γωνιακών κατανομών που αφορούν στην εξάχνωση σωματιδίων άλφα από τον σύνθετο πυρήνα, στα πειραματικά δεδομένα των πίσω γωνιών. Οι εν λόγω θεωρητικές γωνιακές κατανομές υπολογίστηκαν με τη χρήση του κώδικα PACE2. Εν

συνεχεία, λαμβάνοντας υπ' όψιν τις πολλαπλότητες για την εξάχνωση σωματιδίων άλφα από τον σύνθετο πυρήνα, υπολογίσθηκαν οι ενεργές διατομές σύντηξης. Δεδομένου ότι οι πολλαπλότητες εξαρτώνται άμεσα από την επιλογή του οπτικού δυναμικού που χρησιμοποιείται για να περιγράψει την εξάχνωση των σωματιδίων άλφα από τον σύνθετο πυρήνα, πραγματοποιήσαμε δοκιμές με τρία διαφορετικά οπτικά δυναμικά για την εξάχνωση των σωματιδίων άλφα προκειμένου να εκτιμήσουμε το σφάλμα στον υπολογισμό της πολλαπλότητας και κατ' επέκταση το σφάλμα που υπεισέρχεται στον υπολογισμό της ενεργού διατομής σύντηξης. Τα αποτελέσματα των ενεργών διατομών σύντηξης όπως προσδιορίστηκαν από την παρούσα μέτρηση, ύστερα από την αναγωγή τους στις λεγόμενες καμπύλες σύντηξης, συγκρίθηκαν με παρόμοια δεδομένα που αφορούν αλλά ασθενικά δέσμια (σταθερά ή ραδιενεργά) βλήματα και βρέθηκαν σε εξαιρετική συμφωνία μεταξύ τους καθώς και με την Καθολική Καμπύλη Σύντηξης (UFF) μέσα σε ένα εύρος 10% με 20%. Επιπλέον, προσδιορίστηκαν οι λόγοι των καμπύλων σύντηξης του  ${}^6\text{Li}$  ως προς εκείνες για το  ${}^7\text{Li}$  και το  ${}^7\text{Be}$ . Οι λόγοι αυτοί παρουσιάζουν μια αυξητική τάση στην ενεργειακή περιοχή του φράγματος Coulomb και κάτω από αυτό, υποδεικνύοντας μια ελάττωση της ενεργού διατομής σύντηξης για τους πυρήνες  ${}^7\text{Li}$  και  ${}^7\text{Be}$  ως προς τις αντίστοιχες τιμές για το  ${}^6\text{Li}$ . Η ίδια ελάττωση είχε παρατηρηθεί και σε προηγούμενες μετρήσεις για τον πυρήνα του  ${}^7\text{Li}$  με διαφορετικούς στόχους. Η συστηματική αυτή συμπεριφορά του λόγου των καμπύλων σύντηξης σε συνδυασμό με τα αποτελέσματα της ενεργειακής εξάρτησης του οπτικού δυναμικού, αποτελούν μια ισχυρή απόδειξη ότι ο πυρήνας  ${}^7\text{Be}$  συμπεριφέρεται όπως ο κατοπτρικός του πυρήνας  ${}^7\text{Li}$  και όχι όπως ο πυρήνας του  ${}^6\text{Li}$ .

Οι γωνιακές κατανομές για την παραγωγή σωματιδίων άλφα από άμεσες αντιδράσεις εκτιμήθηκαν αφαιρώντας από τις πειραματικές γωνιακές κατανομές της συνολικής παραγωγής σωματιδίων άλφα, τις προσαρμοσμένες στις πίσω γωνίες θεωρητικές καμπύλες για την εξάχνωση σωματιδίων άλφα από τον σύνθετο πυρήνα. Από την σύγκριση των πειραματικών δεδομένων με τις θεωρητικές γωνιακές κατανομές για την παραγωγή σωματιδίων άλφα μέσω της αντίδρασης αρπαγής ενός νετρονίου, της αντίδρασης απογύμνωσης ενός νετρονίου καθώς και της αντίδρασης διάσπασης, συμπεράναμε ότι οι διαδικασίες αυτές υποεκτιμούν την παραγωγή σωματιδίων άλφα από άμεσες αντιδράσεις. Ως εκ τούτου, το υπολειπόμενο μέρος της παραγωγής σωματιδίων άλφα αποδόθηκε στην αντίδραση απογύμνωσης ενός σωματιδίου  ${}^3\text{He}$  αν και η υπόθεση αυτή δεν επαληθεύτηκε με κάποιο θεωρητικό υπολογισμό στα πλαίσια της Προσέγγισης Born Παραμορφωμένου Κύματος (DWBA) λόγω έλλειψης των κατάλληλων τιμών για τους φασματοσκοπικούς συντελεστές (Spectroscopic Factors). Όσον αφορά την παραγωγή σωματιδίων  ${}^3\text{He}$ , οι μόνες διεργασίες που συνεισφέρουν είναι η αντίδραση διάσπασης και η αντίδραση απογύμνωσης ενός σωματιδίου  ${}^4\text{He}$ . Λόγω της χαμηλής στατιστικής καθώς και της γεωμετρικής απόδοσης της ανιχνευτικής μας διάταξης, δεν μπορέσαμε να καταγράψουμε γεγονότα σύμπτωσης μεταξύ σωματιδίων  ${}^3\text{He}$ - ${}^4\text{He}$  ώστε

να παρέχουμε την πειραματική τιμή για την ενεργό διατομή διάσπασης. Επομένως, ολοκληρώνοντας τις πειραματικές γωνιακές κατανομές των  $^3\text{He}$ , παρέχουμε την ενεργό διατομή για την παραγωγή  $^3\text{He}$  από την συνεισφορά και των δύο διεργασιών. Όμως λαμβάνοντας υπ' όψιν ότι η τιμή για την ενεργό διατομή της αντίδρασης διάσπασης, όπως προβλέπεται από τον CDCC υπολογισμό είναι πολύ μικρή, ο κύριος μηχανισμός για την παραγωγή των σωματιδίων  $^3\text{He}$  είναι η αντίδραση απογύμνωσης ενός σωματιδίου  $^4\text{He}$ .

Τέλος, έχοντας στη διάθεση μας τις ενεργές διατομές για την παραγωγή σωματιδίων  $^3\text{He}$  καθώς και για την παραγωγή σωματιδίων  $^4\text{He}$  από άμεσες αντιδράσεις και αντιδράσεις σύνθετου πυρήνα, υπολογίσαμε το λόγο της ενεργού διατομής των άμεσων αντιδράσεων ως προς την ολική ενεργό διατομή της αντίδρασης που υπολογίστηκε ως το άθροισμα της ενεργού διατομής από άμεσες αντιδράσεις και της ενεργού διατομής σύντηξης. Η ενεργειακή εξάρτηση του λόγου για το υπό μελέτη σύστημα συγκρίθηκε με την αντίστοιχη ενεργειακή εξάρτηση του λόγου για τους πυρήνες  $^6\text{Li}$  και  $^7\text{Li}$  στον ίδιο στόχο. Και για τα τρία βλήματα, ο λόγος παρουσιάζει την ίδια συμπεριφορά. Δηλαδή, προσεγγίζοντας το φράγμα Coulomb με κατεύθυνση από τις μεγαλύτερες προς τις μικρότερες ενέργειες, παρατηρείται μια αυξητική τάση στην συνεισφορά από ευθείς αντιδράσεις. Για την περίπτωση του πυρήνα  $^7\text{Li}$ , η τιμή του λόγου είναι μεγαλύτερη από ότι η αντίστοιχη τιμή για τον πυρήνα του  $^6\text{Li}$ . Οι τιμές του λόγου για το σύστημα  $^7\text{Be} + ^{28}\text{Si}$  ακολουθούν σε ένταση τις αντίστοιχες τιμές του λόγου για το σύστημα  $^7\text{Li} + ^{28}\text{Si}$  υποδεικνύοντας την ομοιότητα των δύο κατοπτρικών πυρήνων. Η αύξηση της ενεργού διατομής των άμεσων αντιδράσεων ως προς τις αντιδράσεις σύνθετου πυρήνα για το  $^7\text{Li}$  και το  $^7\text{Be}$  είναι άρρηκτα συνδεδεμένη με την ελάττωση της ενεργού διατομής σύντηξης για τους δυο αυτούς πυρήνες όπως αναφέρθηκε παραπάνω.



# Abstract

The present work refers to the study of elastic scattering and reaction products for the system  ${}^7\text{Be} + {}^{28}\text{Si}$  at near barrier energies, namely 13.2, 17.2, 19.8 and 22.0 MeV ( $E/V_{C.b.} = 1.14, 1.48, 1.71, 1.90$ ). The goal of this work is to probe the energy dependence of the optical potential as well as the interplay between direct and compound nucleus mechanisms. The experiment was visualized at the EXOTIC beam line of the **Istituto Nazionale di Fisica Nucleare - Laboratori Nazionali di Legnaro (INFN-LNL)** in Italy. The  ${}^7\text{Be}$  secondary beam was produced via the in-flight technique through the  ${}^1\text{H}({}^7\text{Li}, {}^7\text{Be})\text{n}$  reaction, where a  ${}^7\text{Li}$  primary beam with an intensity of (100-150)pnA, delivered by the LNL XTU-TANDEM Van de Graaff accelerator, impinged on a primary hydrogen gas target. The produced  ${}^7\text{Be}$  beam was separated from other contaminants by means of a bending dipole and a Wien filter and it was directed into the scattering chamber, impinging on a  ${}^{28}\text{Si}$  target. A  ${}^{208}\text{Pb}$  target was also used for normalization purposes. The various ejectiles were collected by six  $\Delta E$ -E telescopes of the detector array of the EXOTIC facility, **EXPADES (EXotic Particle DEtection System)**, placed at symmetrical position to balance any beam divergence and to improve the statistics of the measurement. The  $\Delta E$  stage of the telescopes was a **Double Sided Silicon Strip Detector (DSSSD)** (45-60) $\mu\text{m}$  thick, while the E stage was a DSSSD  $\sim 300 \mu\text{m}$  thick. Also, our experimental setup included two X-Y position sensitive **Parallel Plate Avalanche Counters (PPAC's)** for monitoring the secondary beam profile and providing information for an event by event reconstruction of the beam particle and elastic scattering trajectories.

The analysis of the elastic scattering data was performed by means of an event by event analysis code using the two PPAC signals to enable reconstruction of the beam ray and elastic scattering trajectories. The position of the reaction vertex on the target and of the DSSSD X-Y strip struck by the elastically scattered nucleus were thus unambiguously defined for each event, leading to a more precise assignment of angle (see Appendix A). Events with the same angle or with an angle inside an angular range corresponding to the dimensions of a particular strip of each EXPADES detector ( $\Delta\theta \sim 2^\circ$ ) were summed up and were appropriately normalized for the deduction of differential cross sections.

The elastic scattering data were analyzed into the optical model framework following the same method as adopted previously for  ${}^6,7\text{Li} + {}^{28}\text{Si}$  using the code ECIS. The real part of the optical potential was derived in a double folding model using the microscopic BDM3Y1 interaction. Although the microscopic BDM3Y1 interaction is purely real, assuming that the imaginary part of the optical potential presents the same radial shape as the real one, the

same folded potential was adopted but with a different normalization factor. The normalization factors for the real and the imaginary part were fitted to the data and the energy evolution of these parameters was deduced. Due to the large errors, it was not possible to draw firm conclusions solely from the elastic scattering data but only in conjunction with the  $\alpha$  - particle production ones. In principle the trend of the imaginary part obtained from the elastic scattering data, seems to be compatible with a standard threshold anomaly, with a decreasing magnitude as we approach the barrier from higher to lower energies. The agreement of the present data with a dispersion relation cannot be confirmed, as in the critical position of the real potential, where a peak should appear, we possess only one datum. On the other hand, taking into account all information relevant to previous data of  ${}^6,{}^7\text{Li} + {}^{28}\text{Si}$ , analyzed in the same framework as is the present case, we can in principle conclude that both mirror nuclei,  ${}^7\text{Li}$  and  ${}^7\text{Be}$  present the same energy dependence of the optical potential. This is close to the standard threshold anomaly, from the point of view of the decreasing imaginary potential but where possibly the dispersion relation does not hold and the real part is consistent with a flat line independent of energy. This evidence, if combined with the results of the  $\alpha$  - production data, collected at the same experiment, indicates with some confidence the similarity between the two mirror nuclei.

Our optical model analysis yielded also total reaction cross sections which were found in very good agreement with the total reaction cross sections deduced from the  ${}^3,{}^4\text{He}$ -particle production, global phenomenological predictions and our CDCC calculations. The last were performed with the code FRESKO and it was found that the effect of coupling to the ground state reorientation and excitation of the first excited state of  ${}^7\text{Be}$  is weak. Despite a very small breakup cross section the coupling to continuum was found to be significant but not very strong. As far as the total reaction cross sections, the compatibility with the phenomenological predictions and the CDCC calculations indicates the validity of our measurements. It also supports our results for the energy dependence of the optical potential, since total reaction cross sections are traditionally used to restrict the imaginary part of the optical potential.

Regarding the reaction mechanisms, the analysis of the data refers to the  ${}^3\text{He}$  and  ${}^4\text{He}$  particle production either through a direct or a compound nucleus process. These light reaction products were able to pass through the  $\Delta E$  stage of the telescopes and thus, they were well-discriminated via the  $\Delta E$ -E technique. The  ${}^3\text{He}$  and  ${}^4\text{He}$  yields were obtained by applying the appropriate energy windows on the two dimensional  $\Delta E$ -E plots. However, due to the thickness of the  $\Delta E$  stage of the telescopes, an energy threshold in the detection of the two ions was introduced. The missing counts were retrieved by comparing the experimental energy spectra

with the simulated ones. The simulated energy spectra for the direct processes were generated by a Monte Carlo code (see Appendix B), while the compound nucleus spectra were produced via the code PACE2 (**P**rojection **A**ngular-momentum **C**oupled **E**vaporation). Then, direct and the compound nucleus spectra were summed using various assumptions for the ratio direct to compound nucleus contributions until the best fit to the experimental data was obtained. After correcting for the missing counts, the differential cross sections for  ${}^3\text{He}$  and  ${}^4\text{He}$  particle production were deduced.

The compound nucleus contribution to the  ${}^4\text{He}$ -particle production was estimated by re-normalizing the theoretical angular distributions from evaporated  $\alpha$ -particles, calculated via the statistical model code PACE2, to the data of the backward angle detectors. Subsequently, using the  $\alpha$ -particle multiplicities, obtained with the same statistical model code, fusion cross sections were deduced. The  $\alpha$ -particle multiplicities are sensitive on the choice of the optical model parameters for the evaporation of  $\alpha$ -particles and this may introduce further uncertainties in the fusion cross sections. In this direction, the error in the calculated multiplicities was estimated adopting three different sets of optical model parameters for the evaporation of  $\alpha$ -particles. The deduced fusion cross sections (appropriately reduced to fusion functions) were considered in a systematic framework with other stable, weakly bound and radioactive projectiles on the same or similar mass targets and were found in good agreement between each other as well as the **U**niversal **F**usion **F**unction (UFF) to within an uncertainty band of 10% to 20%. Moreover, ratios of fusion functions for  ${}^6\text{Li}$  to those for  ${}^7\text{Li}$  and  ${}^7\text{Be}$  were formed, indicating a hindrance of fusion for  ${}^7\text{Li}$  and  ${}^7\text{Be}$  with respect to those of  ${}^6\text{Li}$  below the barrier rather than an enhancement. This hindrance was also observed before for  ${}^7\text{Li}$  on various targets and together with the results obtained from our optical model analysis present a strong evidence for the similarity of  ${}^7\text{Be}$  with its mirror nucleus  ${}^7\text{Li}$  and not the  ${}^6\text{Li}$  one.

The angular distributions for the direct component of the  $\alpha$ -production were obtained after subtracting from the total  $\alpha$  experimental angular distributions, the re-normalized theoretical compound nucleus ones. Comparisons between experimental data and the theoretical angular distributions for the single neutron pickup, single neutron stripping and breakup showed that these processes are unable to describe the bulk of the observed  $\alpha$ -particle cross sections. Therefore, the remaining part was attributed to the  ${}^3\text{He}$  stripping reaction although this was not confirmed via DWBA calculations, due to the lack of the appropriate spectroscopic factors. Regarding the  ${}^3\text{He}$  production, the only two contributing mechanisms are the  ${}^4\text{He}$  stripping and the breakup. Due to the low statistics and the geometrical efficiency of our detector setup, coincidence events between  ${}^3\text{He}$  and  ${}^4\text{He}$  particles, a clear signature of an exclusive breakup

event, were not recorded. Therefore, integrating the  $^3\text{He}$  angular distributions, we can provide an inclusive cross section for both reaction channels although the breakup is predicted in CDCC calculations to be very small and therefore this cross section is described mainly by the  $^4\text{He}$  stripping process. DWBA theoretical calculations are in reasonable qualitative agreement with the experimental data but underestimate them in absolute magnitudes. The last was attributed to the fact that absolute spectroscopic factors for  $\alpha$  transfer reactions are ambiguously determined, with factors of 5 or more between values for the same target obtained with different reactions and at different bombarding energies being common.

Finally, total reaction cross sections were formed as the sum of the direct and fusion cross sections and the ratio of direct to total reaction cross sections as a function of energy was deduced. These ratio's were compared with previous ones for  $^{6,7}\text{Li}$  on  $^{28}\text{Si}$ , where an increasing trend approaching the barrier from higher to lower energies is seen. For  $^7\text{Li}$  larger ratio's than in  $^6\text{Li}$  are observed and our data for  $^7\text{Be}$  are in quantitative agreement with the data of  $^7\text{Li}$  and not  $^6\text{Li}$ , pointing out to a similarity between the two mirror nuclei. This enhancement of direct channels versus compound for  $^7\text{Li}$  and  $^7\text{Be}$  acts at the expense of fusion resulting in the fusion hindrance mentioned above.

# Introduction

This work is part of the curriculum of the Postgraduate Program of the Department of Physics, University of Ioannina. The research area belongs to the basic direction of Nuclear Physics and in particular on the subject of elastic scattering and reaction mechanisms at near barrier energies involving weakly bound nuclei.

Elastic scattering is the simplest process in the nucleus-nucleus collisions. But even in such “simple” case, the nuclear interactions are far too complicated since the interacting nuclei are composite systems of many nucleons. A solution to the complex many-body problem of the interaction of two nuclei may be given by the **O**ptical **M**odel (OM), which approximates the interaction of two nuclei by the interaction of two structureless particles through an effective potential. In the Optical Model framework the interaction between two nuclei is represented by a complex potential, where the real part accounts for the refraction of the incident particles by the target, while the imaginary part for the absorption of flux out of the elastic channel via the different reaction mechanisms. Both terms of the optical potential are energy dependent and in this direction, many studies over the past decades have been devoted to study the energy dependence of the optical potential through elastic scattering measurements.

At energies well above Coulomb barrier, the energy evolution of the optical potential is almost energy independent. However, this independence no longer holds while approaching the vicinity of Coulomb barrier. A first indication for an unusual behavior of the potential in the vicinity of Coulomb barrier was provided by optical model analyses of elastic scattering for  $^{16}\text{O} + ^{208}\text{Pb}$  [1] and  $^{32}\text{S} + ^{40}\text{Ca}$  [2]. Subsequently, the term “**T**hreshold **A**nomaly” (TA) [3–5] was applied to such cases, where a rapid and localized variation with energy  $E$  of the heavy-ion optical potential appears at barrier. This variation is visualized as a localized peak in the strength of the real potential, associated with a sharp decrease in the strength of the imaginary potential as it becomes more and more unimportant to remove flux from the reaction in this low energy region. The advent of **R**adioactive **I**on **B**eam (RIB) facilities moved the interest to predecessor cases with weakly bound but stable projectiles, since direct processes like breakup and transfer are enhanced for such systems [6–11]. It was believed [4, 12, 13] that the polarization potential which is produced by the breakup, as it is repulsive in nature, will compensate the attractive term,  $\Delta V$ , of the real potential ( $V = V_0 + \Delta V$ ) which is connected through a dispersion relation [4, 5] with the imaginary part and which is responsible for the threshold anomaly. Otherwise, as it is suggested by Satchler [4], the dispersion relation may be of no use for weakly bound systems, since according to theoretical calculations [12, 13], the

repulsive contribution of the real part of the potential, is almost independent of beam energy, while the associated imaginary potential is very small. Indeed, the pioneering experimental work of elastic scattering with the weakly bound but stable projectiles  ${}^6\text{Li}$  and  ${}^7\text{Li}$  on  ${}^{208}\text{Pb}$  and  ${}^{138}\text{Ba}$  targets [14, 15] traced an unusual behavior for  ${}^6\text{Li}$  but not with  ${}^7\text{Li}$ . It should be taken into account that the breakup threshold for the first nucleus is only 1.47 MeV, while for the second is 2.47 MeV. Later on the new manifestation of the anomaly for  ${}^6\text{Li}$ , is observed for  ${}^6\text{Li} + {}^{28}\text{Si}$  [16] and is interpreted in terms of dispersion relations in Ref. [17]. With the aid of a re-analysis of previous data, it was pointed out in these articles [16, 17] the increasing trend of the imaginary potential approaching the barrier from higher to lower energies for  ${}^6\text{Li}$ , but not for  ${}^7\text{Li}$ . This increasing behavior is related via dispersion relations with an almost flat evolution of the real part of the potential (with a shallow valley at barrier), developing the bell shape peak at very low energies well below barrier [17–20]. The new manifestation of the anomaly for  ${}^6\text{Li}$  is discussed later in Ref. [21] and named as **Breakup Threshold Anomaly** (BTA). By today the new anomaly for  ${}^6\text{Li}$  but not for  ${}^7\text{Li}$  is well established although not fully understood and verified in numerous articles for various targets as  ${}^{27}\text{Al}$  [22],  ${}^{28}\text{Si}$  [16, 17],  ${}^{58}\text{Ni}$  [23],  ${}^{59}\text{Co}$  [24],  ${}^{64}\text{Zn}$  [25],  ${}^{80}\text{Se}$  [26],  ${}^{90}\text{Zr}$  [27],  ${}^{112,116}\text{Sn}$  [28],  ${}^{138}\text{Ba}$  [15],  ${}^{144}\text{Sm}$  [29],  ${}^{208}\text{Pb}$  [14],  ${}^{209}\text{Bi}$  [30] and  ${}^{232}\text{Th}$  [31]. A review of these measurements can be found in Ref. [32].

The situation is less clear for radioactive projectiles. Existing measurements are reviewed in Ref. [8] and concern mainly the neutron rich nucleus  ${}^6\text{He}$  and the proton rich nuclei  ${}^8\text{B}$  and  ${}^7\text{Be}$ . Comprehensive work on the energy dependence of the potential via angular distributions measurements is achieved for  ${}^6\text{He}$  on both  ${}^{208}\text{Pb}$  [33, 34] and  ${}^{209}\text{Bi}$  [35] targets. The conclusion is that the potential behavior of  ${}^6\text{He}$  is the same as for  ${}^6\text{Li}$ , and it can be attributed to the very low binding energy of the two neutrons to an alpha core of 0.973 MeV. Elastic scattering measurements with the cocktail radioactive beam ( ${}^8\text{B}$ ,  ${}^7\text{Be}$ ,  ${}^6\text{Li}$ ) on  ${}^{58}\text{Ni}$  were performed in Notre Dame and the results of the analysis are reported in Ref. [36]. The first conclusion, although it is given with caution due to the large uncertainties assigned to the potential parameters, is that both proton rich nuclei,  ${}^8\text{B}$  and  ${}^7\text{Be}$  present the same trend as  ${}^6\text{Li}$  which was measured and analyzed simultaneously with the radioactive ones. This conclusion is later re-confirmed for  ${}^8\text{B}$  in Ref. [37]. However, the re-analysis of  ${}^7\text{Be}$  data [38], including elastic scattering combined with fusion data, showed that  ${}^7\text{Be}$  resembles rather its mirror nucleus than  ${}^6\text{Li}$ , presenting both the usual threshold anomaly. The last measurement appearing in the literature concerning radioactive projectiles is related again with the proton rich  ${}^7\text{Be}$  nucleus, but on elastic scattering from  ${}^{27}\text{Al}$  [39]. The data were collected in two RIB facilities of the Universities of São Paulo and Notre Dame. Due to the low beam flux the researchers of [39] had to use very thick targets. Their optical model results suggest an energy independent

optical potential around barrier, but this conclusion is given as susceptible to the use of very thick targets.

In principle the variations of TA for the optical potential should be connected with variations in reaction mechanisms appearing strong at near and below barrier. Investigations of collisions involving weakly bound nuclei create an interesting field to study reaction mechanisms and coupling effects, since direct reactions like breakup or transfer are enhanced. As it was mentioned above, elastic scattering is a process that can be easily described into the optical model framework by neglecting the structure effects of the interacting nuclei. However, in case of the weakly bound nuclei, exhibiting pronounced cluster structure and low binding energies, breakup might play an important role on the description of elastic scattering data [19]. In this respect, studies for the  $^{11}\text{Be} + ^{64}\text{Zn}$  system [40] or the  $^{11}\text{Li}$  [41, 42] and  $^6\text{He}$  [33, 43, 44] on the heavier  $^{208}\text{Pb}$  target, showed a suppression of the Coulomb rainbow and via CDCC calculations this effect was attributed to coupling to breakup. Also, selected transfer reactions are favoured and this may affect the elastic scattering like in case of  $^9\text{Be} + ^{208}\text{Pb}$  system [45], where it was found that coupling to the single neutron stripping has a strong influence on the theoretical elastic scattering angular distribution leading to a reduction of the pronounced Coulomb rainbow, in the same way like the couplings to breakup. Given the interesting nature of the weakly bound nuclei, several studies have been performed in such systems the past decades to investigate the reaction mechanisms through the light particles production. Large  $\alpha$  yields have been observed for most of the weakly bound projectiles either stable like  $^{6,7}\text{Li}$  and  $^9\text{Be}$  or radioactive like  $^{6,8}\text{He}$ . Exclusive measurements have been reported, mainly for stable weakly bound projectiles, e.g.,  $^6\text{Li}$  on  $^{28}\text{Si}$  [46],  $^{59}\text{Co}$  [47–49],  $^{208}\text{Pb}$  [50, 51],  $^{209}\text{Bi}$  [52],  $^6\text{He}$  on  $^{209}\text{Bi}$  [53],  $^7\text{Li}$  on  $^{28}\text{Si}$  [54],  $^{58}\text{Ni}$  [55],  $^{65}\text{Cu}$  [56],  $^{93}\text{Nb}$  [57] and  $^{208}\text{Pb}$  [51, 58]. Relevant inclusive measurements for stable [59–62] as well as radioactive projectiles [34, 40, 63–67] display significant contributions from direct channels including breakup.

Besides the influence of the direct reactions on elastic channel, it is also interesting the interplay between direct reactions and fusion, which might shed more light to the question of the enhancement or suppression of fusion near and below barrier. Quantifying the energy evolution of the direct contribution to the total cross sections, the authors in Ref. [68] predict a significant direct contribution at the barrier of the order of 50% to 80% for  $^{28}\text{Si}$  and  $^{208}\text{Pb}$  targets, respectively. This prediction is supported by **Coupled Reaction Channels (CRC)** calculations [68]. The direct contribution, according to the prediction, is enhanced up to  $\sim 100\%$  below the barrier, while it is saturated to  $\sim 20\%$  above the barrier. Knowledge of the energy evolution of the ratio with respect to the projectile and target mass, provides important

information for an understanding of the question of the enhancement or suppression of fusion in these systems. It should be noted that fusion cross section enhancements have been reported for various projectiles and targets (see, e.g., the measurements for  ${}^6\text{He} + {}^{209}\text{Bi}$  [69] and  ${}^7\text{Be} + {}^{58}\text{Ni}$  [70]). However, comprehensive measurements disentangling the direct from the compound contribution to the total cross section for  ${}^{6,8}\text{He}$  on  ${}^{238}\text{U}$  [71] and  ${}^{197}\text{Au}$  [72] and  ${}^7\text{Be}$  on  ${}^{238}\text{U}$  [73], show that fusion is not enhanced but follows rather closely a single-barrier penetration model prediction [74].

The team of **Nuclear Physics Laboratory (NPL)** (group leader: Prof. A. Pakou) at the Physics Department of the University of Ioannina in recent years is dealing with the study of elastic scattering and nuclear reactions at near barrier energies in interplay between them, for obtaining the optical potential [16–20, 46, 54, 59, 60, 75–79]. This research is systematic and devoted so far, to studies with the weakly bound stable projectiles  ${}^{6,7}\text{Li}$  on the same target  ${}^{28}\text{Si}$ . Extending these studies to radioactive projectiles, it was proposed the study of the elastic scattering and relevant reaction mechanisms for the system  ${}^7\text{Be} + {}^{28}\text{Si}$  in order to probe the energy dependence of the optical potential. The proton rich  ${}^7\text{Be}$  is a weakly bound radioactive nucleus, with a  ${}^4\text{He} + {}^3\text{He}$  cluster structure, mirror of the weakly bound stable  ${}^7\text{Li}$ . The breakup threshold for  ${}^7\text{Be}$  is 1.59 MeV, lower than the corresponding 2.47 MeV of  ${}^7\text{Li}$  but similar to the 1.47 MeV of  ${}^6\text{Li}$ . The above system was chosen because comprehensive studies already exist for the related systems  ${}^{6,7}\text{Li} + {}^{28}\text{Si}$  and it will be an interesting point to investigate whether the  ${}^7\text{Be}$  resembles more its mirror nucleus,  ${}^7\text{Li}$ , or the  ${}^6\text{Li}$  one, using the information from both elastic as well as reaction channels. From the point of view of reaction channels, a large hindrance of the fusion cross sections for  ${}^7\text{Li}$  compared to  ${}^6\text{Li}$  were reported previously for  ${}^{6,7}\text{Li} + {}^{59}\text{Co}$  [80],  ${}^{6,7}\text{Li} + {}^{28}\text{Si}$  [78],  ${}^{6,7}\text{Li} + {}^{64}\text{Zn}$  [81],  ${}^{6,7}\text{Li} + {}^{24}\text{Mg}$  [82] and  ${}^{6,7}\text{Li} + {}^{28}\text{Si}$  [83]. In more detail, the reported ratios of  ${}^6\text{Li}$  to  ${}^7\text{Li}$  fusion cross sections exhibited an increasing trend approaching the barrier from higher to lower energies, according to some measurements, while the increasing behavior was obvious only well below the barrier for some other measurements. However, within the error bars all measurements were compatible and supported hindrance of fusion for  ${}^7\text{Li}$  compared to  ${}^6\text{Li}$ . Therefore, it will be useful and enlightening to perform such comparisons between fusion cross sections for  ${}^7\text{Be}$  to those for  ${}^6\text{Li}$  and  ${}^7\text{Li}$  in order to investigate the similarity between  ${}^7\text{Be}$  and the two lithium isotopes, in conjunction with the elastic scattering data. The relevant experiment was performed at the EXOTIC facility at the Laboratori Nazionali di Legnaro, Italy, at the beam energies of 22.0, 19.8, 17.2 and 13.2 MeV. The analysis of the data was completed at the NPL-Ioannina and the results are discussed in the present work, which includes the following chapters:

- Chapter 1: Includes the theoretical background that is a brief description of the elastic scattering and reaction mechanisms as well as the main principles of the Optical Model, the **C**ontinuum **D**iscretized **C**oupled **C**hannels (CDCC) method and the **D**istorted **W**ave **B**orn **A**pproximation (DWBA).
- Chapter 2: Includes details of the experimental setup that is a short description of the beam line with the main focus on the **P**arallel **P**late **A**valanche **C**ounters (PPAC's) and the **D**ouble **S**ided **S**ilicon **S**trip **D**etectors (DSSSD's) and their utility in our experimental apparatus.
- Chapter 3: Includes the data reduction, where elastic scattering as well as  ${}^{3,4}\text{He}$  reaction cross sections are determined.
- Chapter 4: Includes the theoretical analysis of the elastic scattering data into the Optical Model framework and the theoretical analysis of the  ${}^{3,4}\text{He}$  reaction data in the statistical model (only for  ${}^4\text{He}$  data), DWBA and CDCC frameworks.
- Chapter 5: Conclusion and summary.



# Chapter 1

## Theory

The interaction between two nuclei can give place to a nuclear reaction. We can distinguish four major categories of nuclear reactions:

- Elastic Scattering
- Inelastic Scattering
- Direct Reactions
- Compound Nucleus Reactions

The present work focuses on the study of elastic scattering and the light particle production either through direct or compound nucleus processes. Therefore, the main characteristics for each process are presented below, together with the theories that have been developed to describe them.

### 1.1 Elastic Scattering

Elastic scattering is the simplest process among the nuclear reactions. The nuclei at the entrance channel are identical to those at the exit channel. The amount of energy released in such process (Q-value) is zero, therefore the total kinetic energy of the system is conserved. The study of the elastic scattering is very useful as it provides information, between other aspects, about the projectile-target nucleus potential which is necessary to perform accurate theoretical calculations for non-elastic processes. At low energies, well-below the Coulomb

barrier, incident particles interact with the target mainly via Coulomb interactions. **Coulomb scattering**, also known as Rutherford scattering, is a well known scattering problem and the differential cross section in the center of mass system in such case is given by the following expression [84]:

$$\frac{d\sigma(\theta)}{d\Omega} = \left( \frac{Z_p Z_t e^2}{4\pi\epsilon_0} \right)^2 \left( \frac{1}{4E_{c.m.}} \right)^2 \frac{1}{\sin^4(\theta/2)}, \quad (1.1)$$

where  $Z_p$  and  $Z_t$  are the atomic numbers of the projectile and the target respectively and  $E_{c.m.}$  is the energy of the projectile in the center of mass frame. However, as the energy of the projectile increases, nuclear forces start to be important and thus, the scattering of the incident particles is determined by the interference between Coulomb and nuclear scattering. As an example, below it is presented the scattering of beam particles by a short range central potential  $V(r)$ , reflecting the short range nature of nuclear forces.

### 1.1.1 Scattering by a short range central potential

In order to describe the scattering of the projectile by the target [85], we have to solve the Schrödinger equation:

$$\left[ -\frac{\hbar^2}{2\mu}\nabla^2 + V(\vec{r}) \right] \Psi(\vec{r}) = E\Psi(\vec{r}), \quad (1.2)$$

where  $\mu$  is the reduced mass,  $E$  is the energy in the center of mass frame and  $V(\vec{r})$  the potential that describes the interaction between the projectile and the target. At large distances from the target, the wave function  $\Psi(\vec{r})$  obeys asymptotically the following expression [86]:

$$\Psi(r, \theta, \phi) \longrightarrow e^{ikz} + f(\theta, \phi) \frac{e^{ikr}}{r}, \quad (1.3)$$

where the first term represents the incoming plane waves which are considered along  $Z$  axis, while the second term represents the scattered particles described by a spherical waves. The quantity  $f(\theta, \phi)$  is called **scattering amplitude** and is the fraction of the incident waves that are scattered at angles  $(\theta, \phi)$ . The scattering amplitude is related to the differential cross section by the well-known formula:

$$\frac{d\sigma(\theta, \phi)}{d\Omega} = |f(\theta, \phi)|^2 \quad (1.4)$$

This is a fundamental relation between scattering theory and scattering experiment as it binds the differential cross section, a purely experimental quantity, with the scattering amplitude which characterizes the wave function at large distances from the target. If the interaction between the projectile and the target is described by a central potential, the system is invariant under rotation around the Z axis and the wave function does not depend on the azimuthal angle  $\phi$ . Then, the wave function  $\Psi(r, \theta)$  can be decomposed in its radial and angular parts [85] and with the partial wave expansion, the wave function may be written as:

$$\Psi(r, \theta) = \frac{1}{r} \sum_{L=0}^{\infty} A_L u_L(r) Y_{L0}(\theta), \quad (1.5)$$

with L being the angular momentum between the projectile and the target,  $A_L$  being the amplitude of each partial wave and  $Y_{L0}$  being the spherical harmonic functions. As it was mentioned above, the total wave function does not depend on the azimuthal angle  $\phi$ . This is the reason why in spherical harmonic functions  $Y_{Lm}$ ,  $m=0$ . Subsequently, the Schrödinger equation can be written as [85, 87]:

$$\left[ -\frac{\hbar^2}{2\mu} \frac{d^2}{dr^2} + \frac{\hbar^2 L(L+1)}{2\mu r^2} + V(r) \right] u_L(r) = E u_L(r). \quad (1.6)$$

For a short range potential (decays faster than  $1/r$ ),  $V(r)$  goes to zero at very large distances from the target. The same is also true for the second term of Equation 1.6. Therefore, the equation above is reduced to:

$$\frac{d^2 u_L(r)}{dr^2} + k^2 u_L(r) = 0, \quad E = \frac{\hbar^2 k^2}{2\mu}. \quad (1.7)$$

The solution for this equation is a linear combination of the Bessel and Neumann functions and for large values of  $r$ , it takes the form of:

$$u_L(r) \longrightarrow B_L \sin \left( kr - \frac{L\pi}{2} + \delta_L \right). \quad (1.8)$$

where  $B_L$  is a constant and  $\delta_L$  is the phase shift. Using Equations 1.5 and 1.8, we are leading to the asymptotic form for  $\Psi(r, \theta)$  given by the following expression [85]:

$$\begin{aligned}\Psi(r, \theta) &= \frac{1}{r} \sum_{L=0}^{\infty} C_L \sin \left( kr - \frac{L\pi}{2} + \delta_L \right) Y_{L0}(\theta) \\ \Psi(r, \theta) &= \sum_{L=0}^{\infty} C_L \left[ (-i)^L e^{i\delta_L} \frac{e^{ikr}}{2ikr} - e^{-i\delta_L} \frac{e^{-i(kr - \frac{L\pi}{2})}}{2ikr} \right] Y_{L0}(\theta)\end{aligned}\tag{1.9}$$

where  $C_L = A_L B_L$ . Working in the same way as previously for  $\Psi(r, \theta)$ , we may expand in partial waves the incident plane waves as follows [85]:

$$\begin{aligned}e^{ikz} &= \sum_{L=0}^{\infty} \sqrt{4\pi(2L+1)} i^L j_L(kr) Y_{L0}(\theta) \\ e^{ikz} &= \sum_{L=0}^{\infty} \sqrt{4\pi(2L+1)} \left[ \frac{e^{ikr}}{2ikr} - \frac{i^L e^{-i(kr - \frac{L\pi}{2})}}{2ikr} \right] Y_{L0}(\theta), r \rightarrow \infty\end{aligned}\tag{1.10}$$

where  $j_L(kr)$  is the Bessel function. Using Equations 1.3 and 1.10, we can write the asymptotic form for  $\Psi(r, \theta)$  as:

$$e^{ikz} + f(\theta) \frac{e^{ikr}}{r} = \sum_{L=0}^{\infty} \sqrt{4\pi(2L+1)} \left[ \frac{e^{ikr}}{2ikr} - \frac{i^L e^{-i(kr - \frac{L\pi}{2})}}{2ikr} \right] Y_{L0}(\theta) + f(\theta) \frac{e^{ikr}}{r}.\tag{1.11}$$

We can see that Equations 1.9 and 1.11 are referred both on the same quantity, the asymptotic behavior of the wave function  $\Psi(r, \theta)$  at large distances from the target. By comparing this two expressions we obtain the coefficient  $C_L$ ,  $C_L = \sqrt{4\pi(2L+1)} i^L e^{i\delta_L}$  and finally, the scattering amplitude is evaluated as:

$$\begin{aligned}
f(\theta) &= \frac{\sqrt{4\pi}}{2ik} \sum_{L=0}^{\infty} \sqrt{2L+1} (e^{2i\delta_L} - 1) Y_{L0}(\theta) \\
f(\theta) &= \frac{\sqrt{4\pi}}{k} \sum_{L=0}^{\infty} \sqrt{2L+1} e^{i\delta_L} \sin(\delta_L) Y_{L0}(\theta).
\end{aligned} \tag{1.12}$$

Having obtained the scattering amplitude, the differential cross section is determined through the following relation:

$$\begin{aligned}
\frac{d\sigma(\theta)}{d\Omega} &= |f(\theta)|^2 \\
\frac{d\sigma(\theta)}{d\Omega} &= \frac{4\pi}{k^2} \left| \sum_{L=0}^{\infty} \sqrt{2L+1} e^{i\delta_L} \sin(\delta_L) Y_{L0}(\theta) \right|^2.
\end{aligned} \tag{1.13}$$

This was a brief description for the elastic scattering of beam particles by a central potential. However, during a nuclear collision besides elastic scattering, other reactions may also take place having an impact on the elastic scattering cross sections. Therefore, to describe in a more accurate way the elastic scattering, we have to take into account the effects of the possible reaction channels via coupling channel theories [88, 89]. Below we give some aspects of the CDCC (Continuum Discretized Coupled Channel) approach most suitable for weakly bound nuclei as is the present case. Otherwise in a more simplistic form the problem can be described into an Optical Model framework which will be discussed also below.

### 1.1.2 Continuum Discretized Coupled Channels Calculations

The **C**ontinuum **D**iscretized **C**oupled **C**hannels (CDCC) method [8, 90–93], is used to describe the elastic scattering taking into account couplings to the continuum states of the weakly bound nucleus (usually the projectile), both resonant and non-resonant ones. The projectile is assumed to be a composite system with an internal cluster structure of a core nucleus and a valence nucleon (or a cluster of nucleons). Therefore, in a CDCC calculation, the (core + target) and the (valence + target) potentials are introduced which may be obtained from an optical model analysis of elastic scattering data of these systems [94–96]. These potentials are very important as they are introduced in the “construction” of the central potential in the  ${}^7\text{Be} + {}^{28}\text{Si}$  entrance as well as in the “construction” of the couplings potentials by means of a single-folding method as [94]:

$$U_{i \rightarrow f}^{SF}(R) = \langle \Phi_f(r) | U_{v-t} \left( \left| \vec{R} + \frac{2}{3} \vec{r} \right| \right) + U_{c-t} \left( \left| \vec{R} - \frac{1}{3} \vec{r} \right| \right) | \Phi_i(r) \rangle, \quad (1.14)$$

where  $R$  is the separation between the projectile and the target,  $r$  is the distance between the two clusters in the projectile and  $U_{c-t}$  and  $U_{v-t}$  are the (core + target) and the (valence + target) potentials respectively.

The continuum phase space above the breakup threshold of the projectile is discretized into a finite number of states. The most widespread methods for the discretization of continuum phase space are the pseudo-states and continuum bins method [8, 97]. In the present work, we have adopted the continuum bins method, since the code FRESKO [98], used to perform our CDCC calculations, is based on that method. In this method, the continuum phase space above the breakup threshold is discretized into a finite number of momentum bins of certain width ( $\Delta k$ ). The wave function of each state is obtained by averaging over the width of bin as [8, 98]:

$$\Phi(r) = \sqrt{\frac{2}{\pi N}} \int_{k_1}^{k_2} w(k) \phi_k(r) dk, \quad (1.15)$$

where

$$N = \int_{k_1}^{k_2} |w(k)|^2 dk, \quad (1.16)$$

$w(k)$  is a weight function and  $\phi_k(r)$  are the single energy-energy eigenstates of the (valence + core) continuum [8]. The choice of the  $k_{max}$  and the width  $\Delta k = (k_2 - k_1)$  of the bins are adjusted empirically by checking the convergence of the calculation. Besides the truncation of the momentum space, the continuum is also truncated in  $L$ , the relative orbital angular momentum between the valence and the core nucleus, where the maximum value of  $L$  is also adjusted empirically. For the calculation of the  $\phi_k(r)$ , the (valence + core) binding potential is necessary. The geometry of this potential is adjusted such as to reproduce quantities like the static quadrupole moment of the ground state or the  $B(E2)$  values for other transitions, while the depth of the potential is adjusted in order to reproduce the binding energy for the bound states or the resonance energy in case of a resonant bin [8].

After the wave functions  $\phi_k(r)$  are obtained, couplings to the continuum states are taken into

account in the standard coupled channels scheme, in order to obtain the angular distributions for the elastic channel as well as for the breakup [8]. As an example of the continuum space truncation, in Figure 1.1 is illustrated the discretization of the continuum phase space as it was considered in the present work for the system  ${}^7\text{Be} + {}^{28}\text{Si}$ , at the energy of 22.0 MeV.

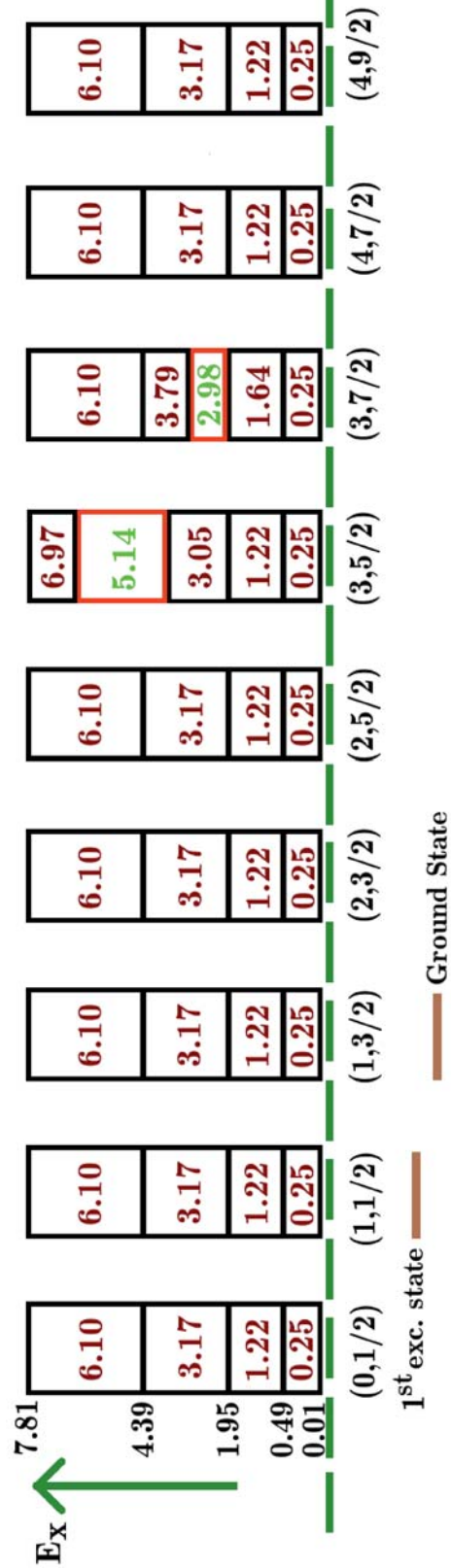


Figure 1.1: Discretization of the continuum phase space using the continuum bins method [8, 97] as it was considered in the CDCC calculation for the system under study at the energy of 22.0 MeV. The values in the center of each box correspond to the mean excitation energy of each bin with respect to the breakup threshold, denoted with the dashed green line. The two bins which are designated with the red boxes correspond to the the  $5/2^-$  and  $7/2^-$  resonances. The pairs of numbers inside the parentheses correspond to the pairs of quantum numbers (L, J).

### 1.1.3 Optical Model

The Optical Model (OM) is one of the simplest and most successful models which is used to describe scattering. The OM provides a solution to the complex many-body problem, approximating the interaction of two nuclei by the interaction of two structureless particles through an effective potential. In the OM framework the interaction between two nuclei is represented by a complex potential, where both real and imaginary parts are energy dependent. The real part is referred to the refraction while the imaginary part accounts for the loss of flux in the elastic channel (non-elastic processes). The imaginary part of the potential interacts with the incident wave and attenuates it [87, 99]. At low energies, it is expected that this attenuation is dominant near the nuclear surface, but as the bombarding energy increases, the absorption of the incident wave may take place throughout the whole volume of the nucleus. So, in the optical model analysis, both surface and volume absorption terms are adopted. Based on that, the full optical potential is given by the expression:

$$U(r) = U_C(r) + U_R(r) + i[W_V(r) + W_S(r)] + U_{S.O}(r), \quad (1.17)$$

where  $U_C(r)$  is the Coulomb potential, necessary if the involved nuclei are charged particles,  $U_R(r)$  is the real part of the optical potential,  $W_V(r)$  and  $W_S(r)$  are the volume and surface absorption terms respectively and  $U_{S.O}(r)$  is the spin-orbit term [87, 100], necessary if the incident particles possess non-zero spins. In the optical model framework, both microscopic and macroscopic potentials are invoked. In the microscopic approach the real part of the potential is obtained by assuming a nucleon-nucleon effective interaction. In contrast, the macroscopic description does not treat the nucleus as a system of different nucleons and thus, the interaction between the projectile and a target can be described in terms of a mean potential.

#### Macroscopic Approach

The most famous macroscopic potential was proposed by Woods and Saxon [101]. The assumed form of this potential is similar to that for the radial dependence of the nuclear density distribution and is following the relation:

$$V(r) = -\frac{V_0}{1 + e^{(r-R)/\alpha}}, \quad (1.18)$$

where  $V_0$  is the potential depth,  $R$  is the radius usually defined as:  $R = r_0(A_p^{1/3} + A_t^{1/3})$ ,

where  $A_p$  and  $A_t$  are the mass numbers of the projectile and the target respectively and  $\alpha$  is the diffuseness which describes the decreasing rate of the potential [100]. The optical potential parameters are usually determined by fitting elastic scattering angular distribution data. However, at this point we would like to stress out the well-known problem of potential ambiguities [102–106]. In this, different families of potentials can provide equivalent fits to the data. To overcome this problem, one has to determine the radial region of sensitivity, where the nuclear potential can be well and uniquely determined. In order to determine the so called sensitive radius, the Crossing Point [77, 103, 107–109] and the Notch Perturbation [77, 110–112] methods are introduced. Below, are presented briefly the main features of each method.

The crossing point method is applied both on the real and the imaginary part of the optical potential and we will assume that they are both described by Woods-Saxon form factors. Working separately for the real and the imaginary part, we are changing manually in small steps the values of the diffuseness  $\alpha_v$  and we are fitting to the data the depth  $V_0$  and the radius  $R_v$ . Then, for the sets  $(V_0, R_v, \alpha_v)$  with the best  $\chi^2$  values, we calculate the potential through the expression 1.18 and we plot these values as a function of radius  $r$ . These potential families cross each other at a specific radial point  $x$  corresponding to the sensitive radius where the optical potential can be uniquely determined. The Notch Perturbation method is based on the introduction of a localized perturbation (notch) into the real or imaginary part of the optical potential at a given radius  $r$ , and the observation of the effect of such a perturbation on the predicted cross sections as the perturbation is moved systematically across the potential. It is expected that at the radial region where the calculation is very sensitive to the potential parameters, the perturbation will strongly affect the calculated cross sections, while away from that region, the impact on the calculated cross sections will be unimportant.

## Microscopic Approach

In the microscopic description of the optical potential, the real part of the optical potential is usually obtained in a double folding model, by using an effective nucleon-nucleon (NN) interaction folded over matter densities of projectile and the target [113, 114]. In this respect, the potential can be written as:

$$U(\vec{R}) = \int d\vec{r}_1 \int d\vec{r}_2 \rho_p(\vec{r}_1) \rho_t(\vec{r}_2) u(r_{12}), \quad (1.19)$$

where  $\rho_i$ ,  $i=(p,t)$ , are the density distributions of the projectile and the target,  $R$  is the distance

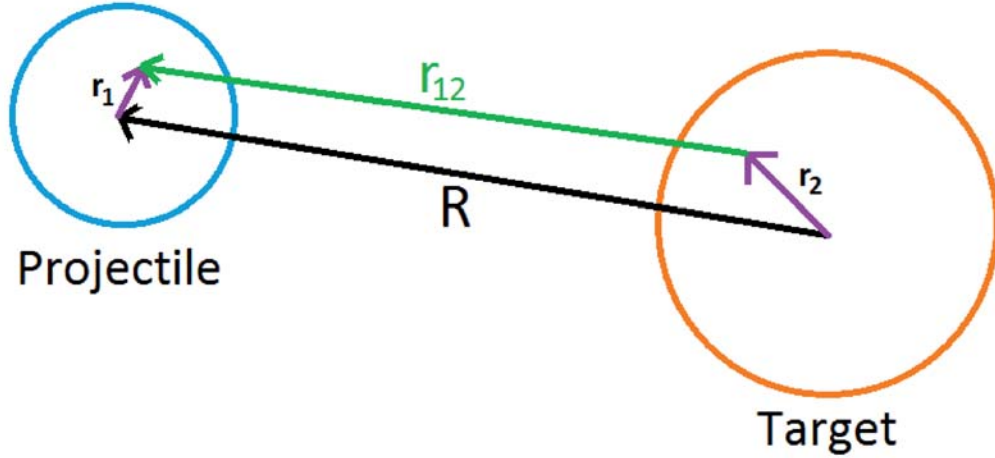


Figure 1.2: *Coordinates used in the folding procedure.*

between the center of mass of the interacting nuclei and  $u(r_{12})$  is the effective NN interaction. In principle, the effective interaction has the form [113, 114]:

$$u(r_{12}) = u_{00} + u_{01}\tau_1 \cdot \tau_2 + u_{10}\sigma_1 \cdot \sigma_2 + u_{11}\sigma_1 \cdot \sigma_2\tau_1 \cdot \tau_2, \quad (1.20)$$

where  $\sigma$  and  $\tau$  are the Pauli matrices for spin and isospin respectively. The M3Y effective interaction [113, 115] is the oldest and the most popular interaction which is widely and successfully used in elastic scattering and other reactions. In the M3Y approach the first term of Equation 1.20 is given as:

$$u_{00}(r, E) = \left[ 7999 \frac{e^{-4r}}{4r} - 2134 \frac{e^{-2.5r}}{2.5r} \right] MeV. \quad (1.21)$$

It is well-established, that the wave function of  $N$  identical fermions has to be antisymmetric. However, the term that describes the effective interaction between two nearby nucleons in the same nucleus is not antisymmetric. To correct that, an additional correction term was added to the relation above and the effective interaction is given by the following expression [114]:

$$u_{00}(r) = \left[ 7999 \frac{e^{-4r}}{4r} - 2134 \frac{e^{-2.5r}}{2.5r} - 276 \left( 1 - 0.005 \frac{E}{A} \right) \delta(r) \right] MeV, \quad (1.22)$$

with  $E$  and  $A$  being the energy and the mass number of the projectile respectively. It should be noted that the M3Y interaction is density independent. Therefore, it is used only in a short density range approximately the 1/3 of the density of a normal nuclear matter [113]. In a more realistic analysis, it is necessary to include a density dependent interaction, like the following [114]:

$$u_{00}^{DD}(r, \rho, E) = u_{00}(r)f(\rho, E), \quad (1.23)$$

where  $u_{00}(r)$  is the original M3Y interaction and  $f(\rho, E)$  is a function following the form:

$$f(\rho, E) = C(E)[1 + \alpha(E)e^{-\beta(E)\rho}], \quad (1.24)$$

with  $\rho$  being the density of nuclear matter and  $C(E)$ ,  $\alpha(E)$  and  $\beta(E)$  being energy dependent parameters. This interaction is known as DDM3Y interaction (**D**ensity **D**ependent M3Y). A specific parametrization for the function  $f(\rho, E)$  was introduced in Refs. [116, 117]

$$f(\rho) = C[1 - \alpha\rho^\beta]. \quad (1.25)$$

This is called BDM3Y interaction and by replacing this term in Equation 1.19, the overall potential can be written as:

$$U(\vec{R}) = \int d\vec{r}_1 \int d\vec{r}_2 \rho_p(\vec{r}_1) \rho_t(\vec{r}_2) u_{00}(r) \left[ C(1 - \alpha\rho^\beta) \right]. \quad (1.26)$$

Some typical parameters for different types of BDM3Y interaction are presented in Table 1.1. In the present work, for our Optical Model analysis we have adopted the BDM3Y1 interaction. Further details are given in Chapter 4.

Table 1.1: *Typical parameters for the different types of BDM3Y interaction [116, 117].*

| Interaction | C      | $\alpha$               | $\beta$ |
|-------------|--------|------------------------|---------|
| BDM3Y0      | 1.3827 | 1.1135 fm <sup>2</sup> | 2/3     |
| BDM3Y1      | 1.2253 | 1.5124 fm <sup>3</sup> | 1.0     |
| BDM3Y2      | 1.0678 | 5.1069 fm <sup>6</sup> | 2.0     |
| BDM3Y3      | 1.0153 | 21.073 fm <sup>9</sup> | 3.0     |

### 1.1.4 Threshold Anomaly and Dispersion Relations

As it was already mentioned, both real and imaginary part of the optical potential are energy dependent. At energies well above the Coulomb barrier, the energy evolution of the optical potential is almost energy independent but approaching the vicinity of the Coulomb barrier, this independence no longer holds. The optical model analysis for elastic scattering data for the  $^{16}\text{O} + ^{208}\text{Pb}$  [1] and  $^{32}\text{S} + ^{40}\text{Ca}$  [2] showed that the imaginary potential decreases rapidly at barrier, while the real potential presents a localized peak. That behavior was named **Threshold Anomaly (TA)**. The real part of the optical potential can be written as:

$$V(E) = V_0 + \Delta V(E), \quad (1.27)$$

where  $V_0$  is an energy independent term and  $\Delta V(E)$  is called dynamic polarization potential and reflects the effect on  $V(E)$  of couplings to non-elastic processes [3–5]. This term is connected with the imaginary part through a dispersion relation. The dispersion relation is similar to that appearing in optics for the interaction between the electric field and a dielectric material, connecting the absorption coefficient with the refraction index [118–120]. In our case, the dispersive term is given by the expression [5]:

$$\Delta V(E) = \frac{P}{\pi} \int_{-\infty}^{\infty} \frac{W(E')}{E' - E} dE', \quad (1.28)$$

where  $P$  is the principle value and  $W(E)$  is the function that describes the energy dependence of the imaginary potential. The subtracted version of Equation 1.28 which was first suggested by Satchler [5], leads to the following expression:

$$\Delta V(E) - \Delta V(E_S) = (E - E_S) \frac{P}{\pi} \int \frac{W(E')}{(E' - E_S) * (E' - E)} dE', \quad (1.29)$$

where  $E_S$  is a reference energy. In order to calculate this quantity, the linear segment model [5] is adopted where in this approach, the function  $W(E)$  is described by three linear segments (or more) as it is shown in Figure 1.3. The result for the  $\Delta V(E)$  is given by the following relation:

$$\pi\Delta V(E) = W_0(\epsilon_a \ln |\epsilon_a| - \epsilon_b \ln |\epsilon_b|) + (W_1 - W_0)(\epsilon'_b \ln |\epsilon'_b| - \epsilon'_c \ln |\epsilon'_c|) - W_1(\epsilon''_c \ln |\epsilon''_c| - \epsilon''_m \ln |\epsilon''_m|) + W_1(\eta \ln \eta - (\eta + 1) \ln (\eta + 1)), \quad (1.30)$$

where  $W_0, W_1 \geq 0$  and

$$\epsilon_i = \frac{E - E_i}{\Delta_0}, \epsilon'_i = \frac{E - E_i}{\Delta_1}, \epsilon''_i = \frac{E - E_i}{\Delta_m}, \eta = \frac{\Delta_1}{\Delta_m}. \quad (1.31)$$

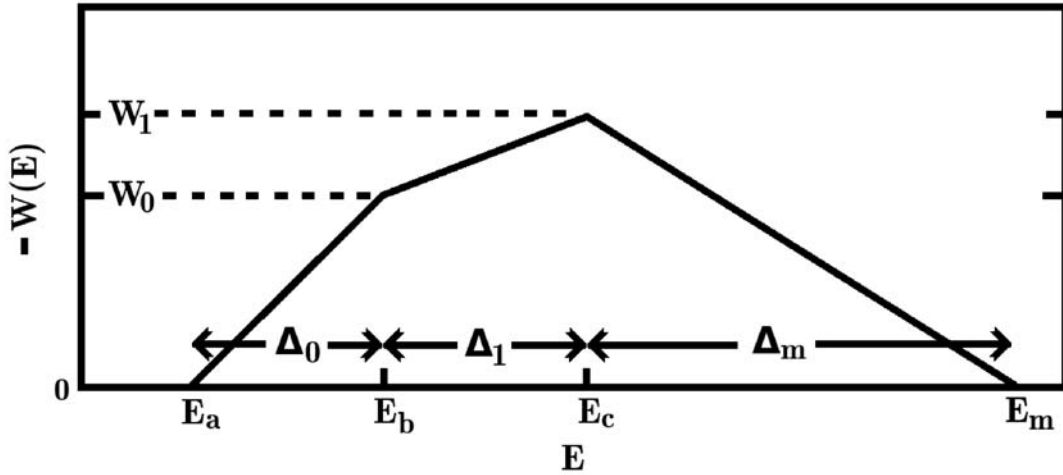


Figure 1.3: *The linear schematic model for  $W(E)$ , consisting of three straight-line segments. Figure from Ref. [4].*

## 1.2 Reaction Mechanisms

As it was already mentioned above, during a nuclear collision different types of reactions can take place. Besides the elastic scattering, where the nuclei at the entrance and the exit channel are the same, we can distinguish two types of nuclear reactions:

**Direct reactions** and **compound nucleus reactions**. The main features for each mechanisms are presented below.

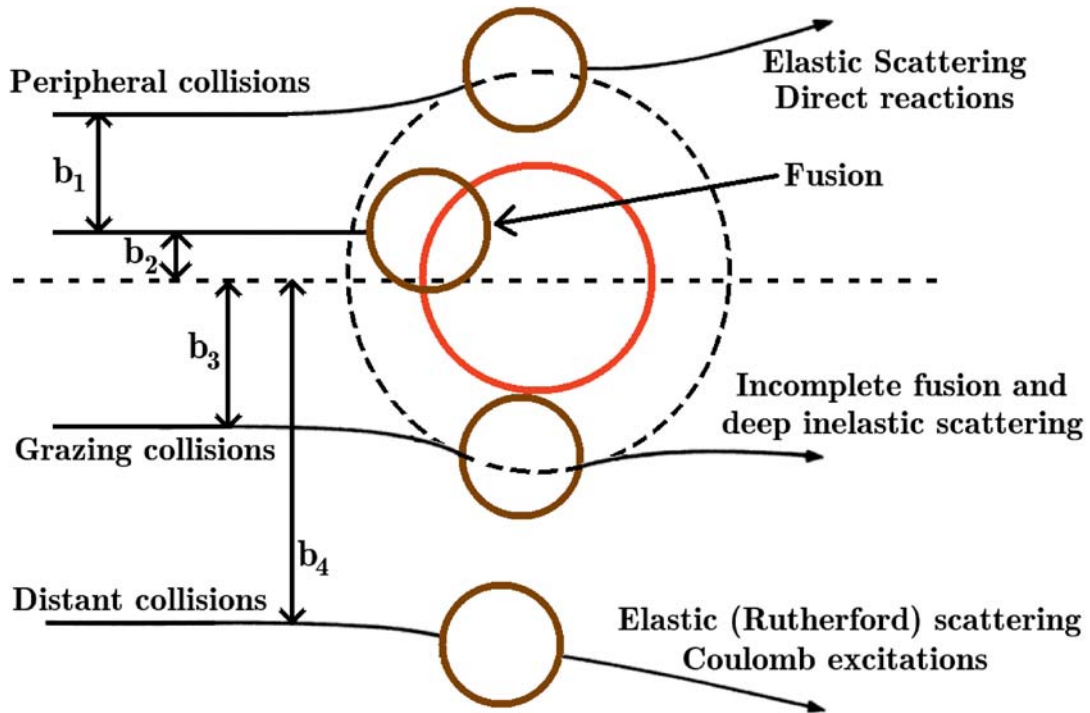
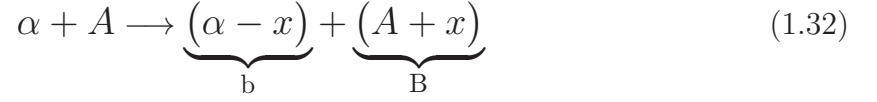


Figure 1.4: *Classical description of the heavy ion collisions, showing the trajectories corresponding to different values of the impact parameter  $b$  [87].*

### 1.2.1 Direct Reactions

The term “direct reaction” characterizes a reaction mechanism which occurs fast and proceeds directly from the initial to the final state without forming an intermediate compound state [8, 99]. The time of interaction between the incident and the target nucleus is very short ( $\Delta t \approx 10^{-22}$ s) compared to the life time of the corresponding compound nucleus ( $t \approx 10^{-17}$ s). In a classical description of the heavy ion collisions via the impact parameter  $b$  [87, 121] (Figure 1.4), direct reactions correspond to trajectories with larger impact parameters than in the case of compound nucleus reactions. The most interesting types of direct reactions are: the stripping reaction, its inverse process, the pickup reaction, the knock-out reaction and the breakup reaction.

- Stripping reactions: In the case of a stripping reaction, when the incident nucleus approaches the target, a strong interaction takes place between the outer nucleons of the projectile and the outer nucleons of the target. Thus, there is a possibility for one or more peripheral nucleons to be detached from the projectile and captured by the target (Figure 1.5a). Assuming a reaction of the form:



the Q-value is given by the expression:

$$Q = (M_\alpha + M_A - M_b - M_B)c^2. \quad (1.33)$$

The binding energy of nucleus B is:

$$E_B = (M_A + M_x - M_B)c^2 \quad (1.34)$$

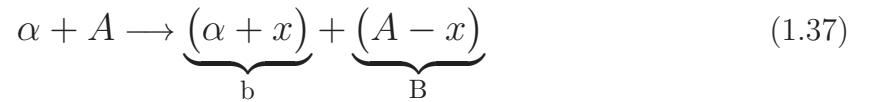
and the separation energy for the removal of the valence particle x from the projectile nucleus  $\alpha$  is given by the expression:

$$S_x = (M_x + M_b - M_\alpha)c^2. \quad (1.35)$$

Using Equations 1.34 and 1.35, the Q-value for a stripping reaction can be written as:

$$Q = (-S_x + E_B). \quad (1.36)$$

- Pickup reactions: The inverse process of the reaction mechanism described above is known as pickup reaction. During a peripheral collision between two nuclei, a cluster of nucleons (or a single nucleon) is transferred from the target to the projectile (Figure 1.5b). Assuming a reaction of the form:



the Q-value is evaluated through the relation 1.33. The binding energy of nucleus b is given as:

$$E_b = (M_\alpha + M_x - M_b)c^2 \quad (1.38)$$

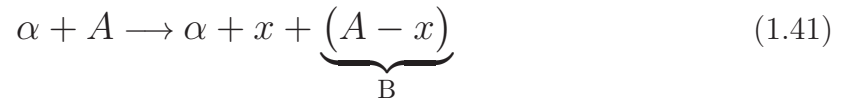
and the separation energy for the removal of the valence particle x from the target nucleus A is given by the expression:

$$S_x = (M_x + M_B - M_A)c^2. \quad (1.39)$$

Using Equations 1.38 and 1.39, the Q-value for a pickup reaction can be written as:

$$Q = (-S_x + E_b). \quad (1.40)$$

- **Knock-out reactions:** In a knock-out reaction [121], during a high energy collision one or more nucleons are knocked-out from the target by the projectile and both projectile and nucleons continue moving freely (Figure 1.5c). On the other hand, in a pickup reaction, one or more nucleons of the target are peaked up by the projectile. The form of a knock-out reaction is:



with a Q-value given as:

$$Q = -S_x, \quad (1.42)$$

where  $S_x$  is the separation energy for the removal of the valence particle  $x$  from the target nucleus  $A$ . These reactions are also known as quasi-free scattering because they permit a description of the whole procedure as an interaction between the target and one of the outer nucleons of the projectile (Figure 1.5c).

- **Breakup reactions:** In a breakup reaction, the projectile nucleus which is usually a weakly bound one (e.g.  ${}^6,7,11\text{Li}$ ,  ${}^7,9\text{Be}$ ) breaks into two or more fragments, due to the Coulomb and/or nuclear interactions with the target nucleus [8]. The breakup process can be further classified in direct and sequential breakup. In the first case, the weakly bound projectiles breaks immediately during the interaction with the target nucleus, while in the later the projectile is formed in a resonant state and subsequently decays into two or more fragments [122]. Considering a breakup reaction as the following one:



the smallest value of the modulus of Q-value for such a process is:

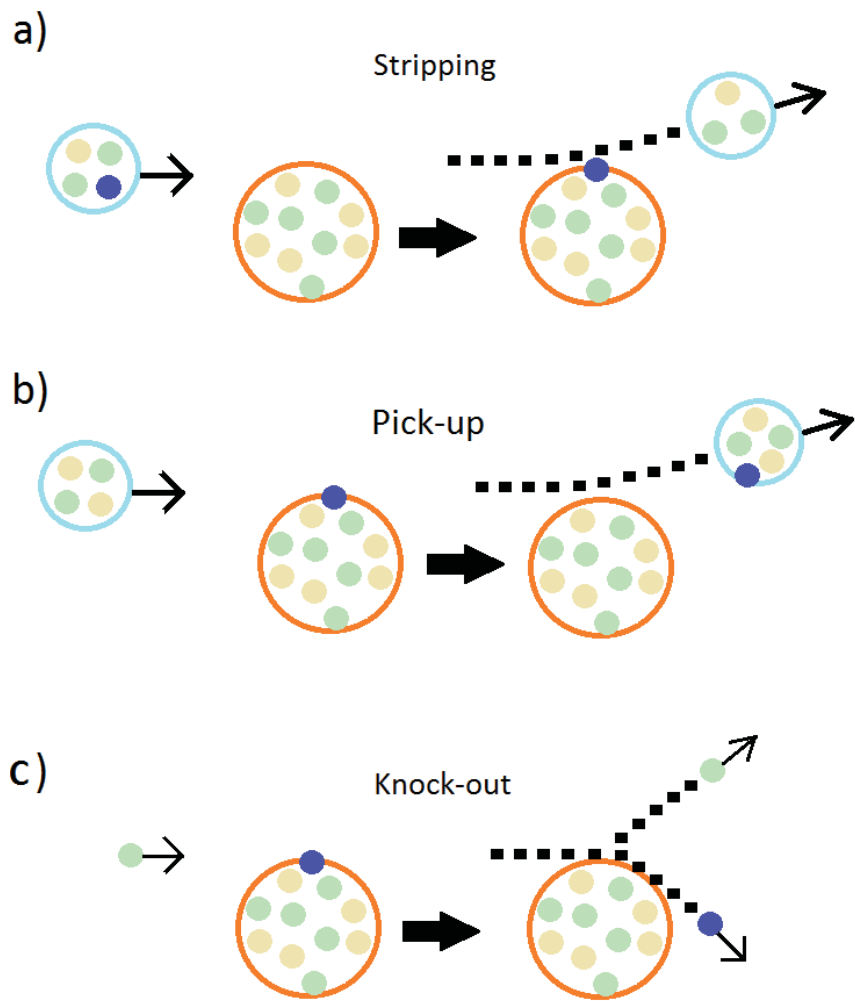


Figure 1.5: *Schematic representation of the direct nuclear reaction mechanisms.*

$$Q = E_\alpha, \quad (1.44)$$

with  $E_\alpha$  being the binding energy of the projectile nucleus  $\alpha$ .

The description of a breakup reaction, is usually performed in the CDCC framework details of which were presented in Subsection 1.1.2. The rest of the direct reactions, may be described in the **D**istorted **W**ave **B**orn **A**pproximation (DWBA) framework, details of which are presented below.

### Distorted Wave Born Approximation

As it was already mentioned in Subsection 1.1.1, in order to describe the scattering of the projectile by the target [85], we have to solve the Schrödinger equation:

$$\left[ -\frac{\hbar^2}{2\mu}\nabla^2 + V(\vec{r}) \right] \Psi(\vec{r}) = E\Psi(\vec{r}), \quad (1.45)$$

where  $\mu$  is the reduced mass,  $E$  is the energy in the center of mass frame and  $V(\vec{r})$  the potential that describes the interaction between the projectile and the target. If we define

$$U(\vec{r}) = \frac{2\mu}{\hbar^2}V(\vec{r}) \quad (1.46)$$

equation 1.45 can be written as:

$$\left( \nabla^2 + k^2 \right) \Psi(\vec{r}) = U(\vec{r})\Psi(\vec{r}). \quad (1.47)$$

The solution of the homogeneous equation (right-hand side of Equation 1.47 equals to zero) corresponds to a plane wave and is given by the expression:

$$X_k(\vec{r}) = Ae^{(\vec{k}\cdot\vec{r})}, \quad (1.48)$$

and so the general solution of Equation 1.47 is:

$$\Psi_k(\vec{r}) = e^{(\vec{k}\cdot\vec{r})} + \int d^3r' G(\vec{r}, \vec{r}') U(\vec{r}') \Psi_k(\vec{r}'), \quad (1.49)$$

where A was set equal to 1 and  $G(\vec{r}, \vec{r}')$  being the Green's function defined as: [87]

$$G(\vec{r}, \vec{r}') = -\frac{1}{4\pi} \frac{e^{ik|\vec{r}-\vec{r}'|}}{|\vec{r}-\vec{r}'|}. \quad (1.50)$$

In order to determine the scattering amplitude and thus the differential cross section, we need to know the behavior of  $\Psi_k(\vec{r})$  at large distances from the target. The Green's function behaves asymptotically as:

$$G(\vec{r}, \vec{r}') = -\frac{1}{4\pi} \frac{e^{ikr}}{r} e^{-i\vec{k}' \cdot \vec{r}'}, r \rightarrow \infty \quad (1.51)$$

where it was assumed that:  $\vec{k}' = k \hat{r}$ . So, the wave function defined by Equation 1.49 has the asymptotic form:

$$\Psi_k(\vec{r}) = e^{i\vec{k} \cdot \vec{r}} - \frac{1}{4\pi} \frac{e^{ikr}}{r} \int d^3r' e^{-i\vec{k}' \cdot \vec{r}'} U(\vec{r}') \Psi_k(\vec{r}'), r \rightarrow \infty. \quad (1.52)$$

Identifying the scattering amplitude as the coefficient of the outgoing wave, we obtain an integral expression for the scattering amplitude:

$$f(\theta, \phi) = -\frac{1}{4\pi} \int d^3r' e^{-i\vec{k}' \cdot \vec{r}'} U(\vec{r}') \Psi_k(\vec{r}'). \quad (1.53)$$

Despite the simple form of the Equation 1.53, we still cannot calculate the scattering amplitude since the integral form contains the unknown wave function  $\Psi_k(\vec{r}')$ , but if the potential  $U(\vec{r})$  is weak, the amplitude of  $\Psi_k(\vec{r}')$  is small and the unknown wave function can be replaced by the plane wave  $e^{i\vec{k} \cdot \vec{r}'}$ . This is called First Order Born Approximation. That leads to the expression of the scattering amplitude where everything is known [121]:

$$f_{BA}(\theta, \phi) = -\frac{1}{4\pi} \int d^3r' e^{-i\vec{k}' \cdot \vec{r}'} U(\vec{r}') e^{i\vec{k} \cdot \vec{r}'}. \quad (1.54)$$

Moving one step forward, we can assume that the potential  $U(\vec{r})$  can be written as  $U(\vec{r}) = U_0(\vec{r}) + U_1(\vec{r})$  and for  $U_0(\vec{r})$  the exact solution can be found by solving the equation [121]:

$$\left(\nabla^2 + k^2\right) X_{0k}(\vec{r}) = U_0(\vec{r}) X_{0k}(\vec{r}). \quad (1.55)$$

So, the plane waves of Equation 1.48 are replaced with the solutions of the above equation and are called distorted waves  $X_{0k}^{(\pm)}(\vec{r})$ . The  $X_{0k}^{(+)}(\vec{r})$  corresponds to a plane wave plus an outgoing scattered wave, while the  $X_{0k}^{(-)}(\vec{r})$  corresponds to a plane wave plus an ingoing scattered wave. Considering all the above, the asymptotic form of the  $\Psi_k(\vec{r})$  can be written as:

$$\Psi_k(\vec{r}) = X_{0k}^{(+)}(\vec{r}) - \frac{1}{4\pi} \frac{e^{ikr}}{r} \int d^3r' X_{0k'}^{(-)}(\vec{r}')^* U_1(\vec{r}') \Psi_k(\vec{r}'), r \rightarrow \infty. \quad (1.56)$$

If the potential  $U_1(\vec{r})$  is sufficiently weak compared to  $U_0(\vec{r})$ ,  $\Psi_k(\vec{r})$  can be replaced by  $X_{0k}^{(+)}(\vec{r})$ . This approximation is called **D**istorted **W**ave **B**orn **A**pproximation (DWBA) and the expression for the scattering amplitude is [121]:

$$f_{DWBA}(\theta, \phi) = f_0(\theta, \phi) - \frac{1}{4\pi} \int d^3r' X_{0k'}^{(-)}(\vec{r}')^* U_1(\vec{r}') X_{0k}^{(+)}(\vec{r}'). \quad (1.57)$$

The entire procedure described above, is referred to the elastic scattering process. In a more general case the interaction potential can be written by two terms. The  $U_0(\vec{r})$  is chosen to describe the elastic scattering, while the  $U_1(\vec{r})$  describes the interaction responsible for the direct reaction. In this respect, it is valid to use DWBA for direct reactions if only the elastic scattering is stronger than any other possible process [121]. Then, the transition amplitude for the reaction A(a,b)B has the form of:

$$f_{direct}^{DWBA}(\theta, \phi) = -\frac{1}{4\pi} \int d^3r_\alpha d^3r_\beta X_\beta^{(-)}(\vec{r}_\beta)^* \langle b, B | U_1 | a, A \rangle X_\alpha^{(+)}(\vec{r}_\alpha), \quad (1.58)$$

where  $X_\alpha$  is used to describe the elastic scattering at the entrance channel ( $\alpha = a + A$ ), while  $X_\beta$  is used to describe the elastic scattering at the exit channel ( $\beta = b + B$ ). Therefore, transition amplitudes are strongly dependent on the entrance and exit channel potentials, highlighting the importance of the elastic scattering measurements which provide the information about nucleus - nucleus potential. In the present work, the theoretical predictions [123] for the transfer reactions under consideration were obtained in the DWBA framework via code FRESKO [98]. Details about the calculations are given in Chapter 4.

## 1.2.2 Compound Nucleus Reactions

In a compound nucleus reaction, the projectile and the target are merged forming a compound nucleus in a high excited state. The compound nucleus life time is  $\approx 10^{-17}$ s (this is the lifetime at low excitation energies and decreases with the increasing excitation energy). During that time interval, the excitation energy of the compound system is shared among the nucleons of which it is consisted until one or more nucleons acquires enough energy to escape [100, 121]. The compound nucleus mechanism can be described by the two-stage scheme:



where  $\alpha$  is the projectile, A is the target,  $C^*$  is the excited compound nucleus and b,  $B^*$  are the reaction products after the compound nucleus decay. The excited  $B^*$  nucleus will decay either through particle emission, if the excitation energy is sufficiently large, or through  $\gamma$ ,  $\beta$  decay [121]. The life time of the compound nucleus is very long compared to the time within the incident particles and the target nucleus interact during a direct reaction. As a consequence, the compound nucleus  $B^*$  has lost the information of its formation (entrance channel) and thus, it will decay in various modes irrespective of the formation process. This is known as Bohr independence hypothesis [100, 121, 124]. Based on that, the cross section for the decay of the compound nucleus to a specific channel can be written as:

$$\sigma_{\alpha b} = \sigma_C(E) * G_b^C(E), \quad (1.60)$$

where  $\sigma_C(E)$  is the formation cross section of the compound nucleus  $C^*$  from the entrance channel  $\alpha + A$  with energy E, and  $G_b^C(E)$  is the probability for the compound nucleus  $C^*$  to decay in the b + B channel. Using the Bohr hypothesis, theories like the Hauser-Feshbach [125] or the Weisskopf-Ewing [126, 127] theory have been developed to predict cross sections for the various decay modes of the compound nucleus. Below are presented briefly the main features of these theories.

### The Hauser-Feshbach theory

Starting from Bohr hypothesis, the cross section for the a particular decay mode from an initial channel c to a final channel c' is:

$$\sigma_{cc'} = \sum_J \sigma_{J\pi}(c) \frac{\Gamma_{c'}^{J\pi}}{\Gamma^{J\pi}}, \quad (1.61)$$

where  $\sigma_{J\pi}(c)$  is the cross section for the compound nucleus formation,  $\Gamma^{J\pi}$  is the sum of the decay widths corresponding to the possible decay modes and the ratio  $\frac{\Gamma_{c'}^{J\pi}}{\Gamma^{J\pi}}$  is the probability for the compound nucleus to decay in a particular channel  $c'$ .  $\Gamma_{c'}^{J\pi}$  is a fraction of the total decay width and is connected with the compound nucleus formation cross section,  $\sigma_{J\pi}(c)$ , via the following relation [87]:

$$\Gamma_{c'}^{J\pi} \propto g_{c'} k_{c'}^2 \sigma_{J\pi}(c), \quad (1.62)$$

where  $k_{c'}$  is the wave number of the emitted particle and  $g_{c'}$  is the statistical weight of the final channel. The cross section for the compound nucleus formation is the sum over all orbital angular momentum values  $\ell$  and is given by the expression [87]:

$$\sigma_{J\pi}(c) = \frac{\pi}{k^2} \frac{(2J+1)}{(2i+1) + (2I+1)} \sum_{\ell} T_{\ell}(c), \quad (1.63)$$

where  $T_{\ell}(c)$  is the transmission coefficient which we assumed that does not depend on spin  $J$ . The transmission coefficients for the light particle emission are usually determined using optical model potentials. Using Equations 1.62 and 1.63 we can write the decay width as:

$$\Gamma_{c'}^{J\pi} \propto g_{c'} k_{c'}^2 \frac{\pi}{k^2} \frac{(2J+1)}{(2i+1) + (2I+1)} \sum_{\ell'} T_{\ell'}(c'). \quad (1.64)$$

In the same way, the sum of all decay widths may be written as:

$$\Gamma^{J\pi} = \sum_c \Gamma_c^{J\pi} \propto g_c k_c^2 \frac{\pi}{k^2} \frac{(2J+1)}{(2i_c+1) + (2I_c+1)} \sum_c \sum_{\ell} T_{\ell}(c). \quad (1.65)$$

where  $k_c$  is the wave number of the projectile,  $g_c$  is the statistical weight of the entrance channel and  $i_c$  and  $I_c$  are the spin of the target and the projectile respectively. Finally, using equations 1.61, 1.63, 1.64 and 1.65, the cross section for the transition from channel  $c$  to the final channel  $c'$  is given by the Hauser-Feshbach theory as [87]:

$$\sigma_{cc'} = \frac{\pi}{k^2} \sum_J \frac{(2J+1)}{(2i_c+1) + (2I_c+1)} \frac{\sum_\ell T_\ell(c) \sum_{\ell'} T_{\ell'}(c')}{\sum_c \sum_\ell T_\ell(c)}. \quad (1.66)$$

### The Weisskopf-Ewing theory

The Weisskopf-Ewing theory [126, 127] is the first statistical model which was used for the description of the compound nucleus decay. This theory is favored when the available energy is enough such as to excite the states of the compound nucleus which are very close to each other and thus cannot be resolved. It is simpler than the Hauser-Feshbach theory, since the decay widths are treated to be independent of spin  $J$  and parity [87]. The cross section for a particular decay mode from an initial channel  $c$  to a final channel  $c'$  is given as:

$$\sigma_{cc'} = \sigma(c) \frac{\Gamma_{c'}}{\Gamma}. \quad (1.67)$$

Using Equations 1.64 and 1.65 (without summing over  $\ell$ ) the relation above can be written as:

$$\sigma_{cc'} = \sigma(c) \frac{g_{c'} k_{c'}^2 \sigma(c')}{\sum_c g_c k_c^2 \sigma(c)}. \quad (1.68)$$

If the energy of the emitted particle after the compound nucleus decay is within the energy range of  $[E_{c'}, E_{c'} + dE_{c'}]$ , the energy of the residual nucleus will be within the energy range of  $[U_{c'}, U_{c'} + dU_{c'}]$  [87], where

$$U_{c'} = E_{comp.} - B_{c'} - E_{c'}, \quad (1.69)$$

with  $E_{comp.}$  and  $B_{c'}$  being the compound nucleus energy and the binding energy of the emitted particle in the compound nucleus respectively. Taking also into account the level density of the residual nucleus  $\omega(U_{c'})$ , Equation 1.68 can be written as:

$$\sigma_{cc'} dE_{c'} = \sigma(c) \frac{g_{c'} k_{c'}^2 \sigma(c') \omega(U_{c'}) dU_{c'}}{\sum_c \int_0^{E_c^{max}} g_c k_c^2 \sigma(c) \omega(U_c) dU_c}. \quad (1.70)$$

The level density of the residual nucleus of the reaction is obtained usually through the constant temperature model [128], the Fermi gas model [129], the Gilbert-Cameron model [130]. The calculations of the cross sections for the possible decay modes of a compound nucleus may be

determined by the statistical model codes like CASCADE [131] or PACE2 [132]. In the code CASCADE, the decay sequence starts with a compound nucleus of a given mass and charge and excitation energy, while its spin distributions are obtained via fusion cross sections from a strong-absorption model [131]. Then the relative decay widths for the emitted particles or  $\gamma$  are calculated and the matrices containing the population of the daughter nuclei as function of excitation energy and angular momentum are generated. This procedure is repeated until the excitation energy of the compound system is lower than the particle emission threshold. One disadvantage of this code is that it cannot provide angular distributions for the emitted particles or the residual nuclei. In case of the code PACE2, the decay sequence is similar as for the code CASCADE, but at each de excitation step of the compound nucleus, angular momentum projections are calculated, which enables to determine the angular distribution of emitted particles. In the present work, the statistical model calculations were performed with the code PACE2. Details about these calculations are presented on Chapter 4.



# Chapter 2

## Experimental Details

The purpose of the present work is the study of the elastic scattering and the relevant reaction mechanisms for the system  ${}^7\text{Be} + {}^{28}\text{Si}$  at near barrier energies. The experiment, proposed by Prof. A. Pakou (University of Ioannina), was visualized at the **Istituto Nazionale di Fisica Nucleare - Laboratori Nazionali di Legnaro** (INFN-LNL) in Italy, at the EXOTIC facility [133–137] with the collaboration of the EXOTIC group and other contributing research groups as appear in the last part of this thesis. The experiment included angular distribution measurements for the various ejectiles, which were performed using the detector array of the EXOTIC facility, EXPADES [138, 139]. Information regarding the beam line are given in the following Section, while details for the detection system as well as the electronics of the present experimental setup are presented in Sections 2.2 and 2.3.

### 2.1 The EXOTIC facility

EXOTIC is a **R**adioactive **I**on **B**eam facility (RIB) hosted at LNL in Italy. In the EXOTIC beam line, the RIBs are produced via the **I**n **F**light technique (IF) in inverse kinematics, where a high intensity primary beam of (100-150)pnA, delivered by the LNL XTU-TANDEM Van de Graaff accelerator, impinges on a gas target. The gas target is confined in a 50 mm long cylindrical cell with two Havar foil windows 2.2  $\mu\text{m}$  thick, located at the entrance and the exit of the cell. The windows tolerance has been tested with an internal gas pressure up to 1.2 bar, while the operating gas pressure at most of the experiments is  $\sim 1$  bar. Furthermore, the gas target is usually cooled down with liquid  $\text{N}_2$  and thus, the gain in the intensity of the secondary beam may be increased by a factor of  $\sim 3$ , compared with a gas target operated

Table 2.1: *Characteristics of the available radioactive ion beams produced at the EXOTIC facility [68, 140].*

| Primary beam    | Gas Target    | Secondary Beam  | Intensity (pps) |
|-----------------|---------------|-----------------|-----------------|
| $^{17}\text{O}$ | $^1\text{H}$  | $^{17}\text{F}$ | $10^5$          |
| $^6\text{Li}$   | $^3\text{He}$ | $^8\text{B}$    | $10^3$          |
| $^7\text{Li}$   | $^1\text{H}$  | $^7\text{Be}$   | $10^5$          |
| $^7\text{Li}$   | $^2\text{H}$  | $^8\text{Li}$   | $10^5$          |
| $^{15}\text{N}$ | $^1\text{H}$  | $^{15}\text{O}$ | $10^4$          |

at a room temperature (300 K) [137]. A list of the RIBs delivered at the EXOTIC facility is included in Table 2.1.

A schematic view of the EXOTIC facility is presented in Figure 2.1, where the first element of the EXOTIC line is the slit set S0, located  $\sim 200$  mm upstream the gas target, which is used to control the dimensions of the primary beam spot. The common values for the S0 slits aperture are  $\pm 1.5$  mm on X and Y axes. After S0, a quadrupole set (Q1-Q3) is placed  $\sim 200$  mm downstream the gas target, ensuring large horizontal and vertical acceptances for the secondary beam of  $\Delta\theta = \pm 50$  mrad and  $\Delta\phi = \pm 65$  mrad respectively. A second slit system, S1, is situated  $\sim 1$  m upstream the dipole magnet (DM) preventing the scattered ions of the primary beam from impinging on the dipole walls, while the  $30^\circ$  bending dipole magnet together with the S2 slit system are used to reduce the beam contaminations. Then, with the appropriate choice of the electric and magnetic fields in the Wien filter (WF), all the spurious ions will be deflected and eventually blocked by slit system S3, located 136 mm downstream the exit of the second quadrupole triplet (Q4-Q6). After the secondary beam is purified, is directed into the scattering chamber.

The scattering chamber of the EXOTIC facility is a 778 mm diameter cylindrical cell that hosts a rotating platform with four available positions at  $\pm 27^\circ$ ,  $\pm 69^\circ$ ,  $\pm 111^\circ$  and  $\pm 153^\circ$  with respect to the beam direction for mounting the telescopes' supports. By rotating the platform, different angular configurations may be achieved depending on the physics case of each experiment.

### 2.1.1 The dipole

The operating principle of a dipole is quite simple. Considering a charge particle  $\alpha$ , with mass  $\mathbf{m}$ , charge  $\mathbf{q}$  moving with constant velocity  $\vec{\mathbf{u}}$  perpendicular to a uniform magnetic field  $\vec{\mathbf{B}}$ , its trajectory will be deflected by the the Lorentz force,  $\vec{\mathbf{F}}_L$ . Thus, the charge particle

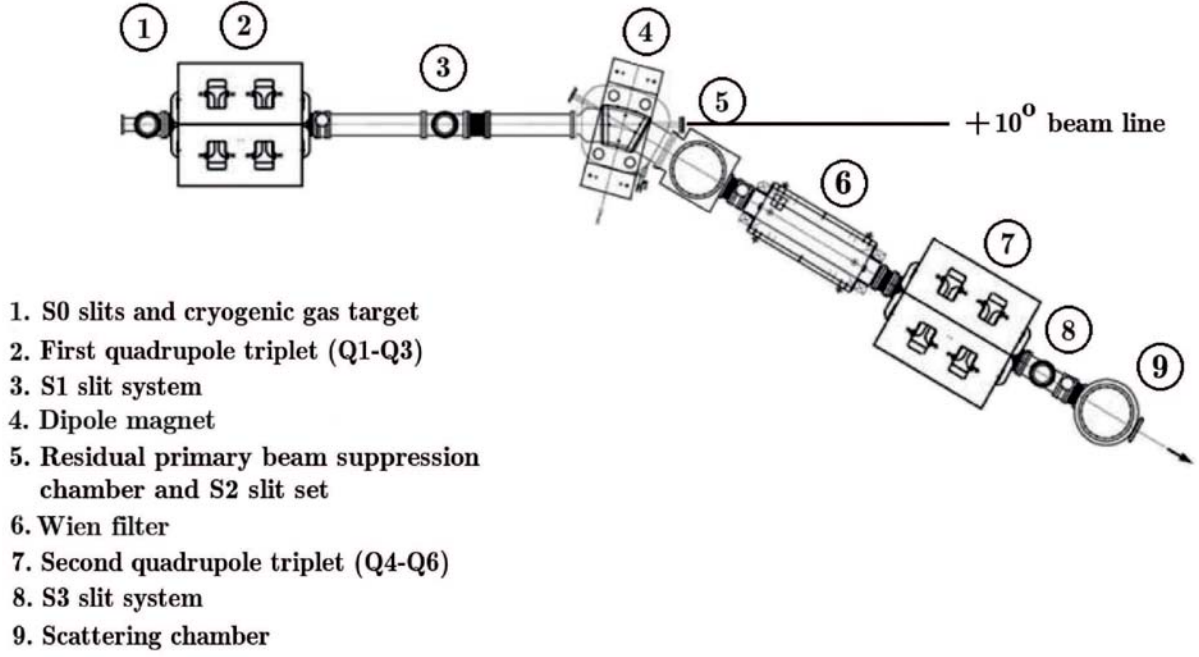


Figure 2.1: A schematic layout of the EXOTIC beam line - Figure from Ref. [135].

is undergoing acceleration leading its track along the circumference of a circle (Figure 2.2a). The equations of motion describing the movement of the particle inside the magnetic field are given by the following expression:

$$\begin{aligned}
 \vec{F}_L &= q\vec{u} \times \vec{B} = m \frac{\vec{u}^2}{\rho} \\
 quB &= m \frac{u^2}{\rho} \\
 B\rho &= \frac{p}{q}
 \end{aligned} \tag{2.1}$$

where,  $\rho$  is the radius of the track and the product  $B\rho$  is the magnetic rigidity. The magnetic rigidity expresses the bending strength of the dipole for a given radius and momentum of the particle. So, the dipole acts like is a filter on magnetic rigidities.

### 2.1.2 The Wien filter

The Wien filter is an optical device consisting of perpendicular electric ( $\vec{E}$ ) and magnetic ( $\vec{B}$ ) fields. Considering the case of the charge particle mentioned above, by entering inside

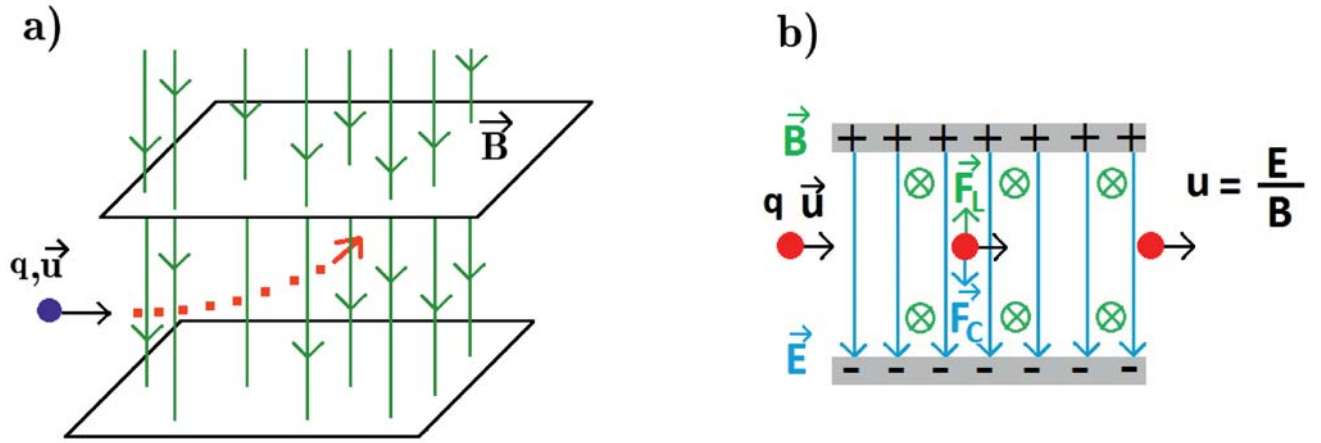


Figure 2.2: a) A schematic representation for the motion of a charge particle inside the homogeneous magnetic field of a dipole. b) The operation of the Wien filter for a given ratio  $E/B$ .

the Wien filter, the ion will “sense” the Coulomb force  $\vec{F}_C$ , as well as the Lorentz one  $\vec{F}_L$ . The two forces have opposite directions (Figure 2.2b). By adjusting properly the values of the electric and magnetic fields, each force will compensate each other allowing particles with a specific velocity to pass through the Wien filter unaffected according to Equation 2.2.

$$\begin{aligned}
 \vec{F}_L &= -\vec{F}_C \\
 q\vec{u} \times \vec{B} &= -q\vec{E} \\
 uB &= E \\
 u &= \frac{E}{B}
 \end{aligned}
 \tag{2.2}$$

## 2.2 Detection systems and electronics

The EXOTIC facility includes the following detections systems: Silicon detectors for monitoring the secondary beam in the beginning of the experiment, to be described in Subsection 2.2.1, two **P**arallel **P**late **A**valanche **C**ounters -PPAC detectors [137, 139] for mapping the trajectory of the secondary beam during the experimental procedure- Subsection 2.2.2- and the detection multi telescope array EXPADES [138, 139] to be described in Subsection 2.2.3.

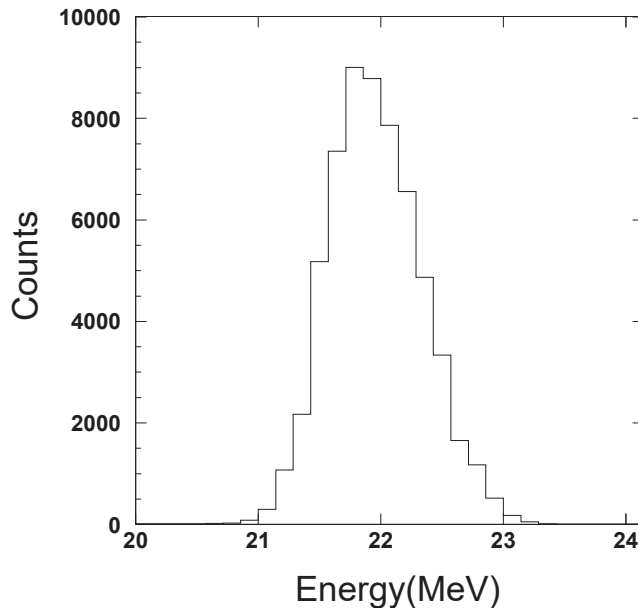


Figure 2.3: A typical one dimensional energy spectrum from the beam monitor  $ML_2$  detector at the energy of 22.0 MeV.

### 2.2.1 Silicon detectors

During the secondary beam production, it is critical to monitor the radioactive beam profile in order to obtain the optimum parameters in the dipole and the Wien filter for rejecting any contaminants and focus as much as possible the secondary beam. The beam monitoring was achieved by using a surface barrier silicon detector, mounted on the target ladder, as a monitor detector ( $ML_2$ ), providing information about the different ions arriving at the target position. The monitor detector was 100  $\mu\text{m}$  thick and it was also used to measure the energy of the secondary beam. A typical spectrum of the  $ML_2$  detector is presented in Figure 2.3, where a clear  ${}^7\text{Be}$  peak is observed. Furthermore, in order to validate the beam purity a  $\Delta E$ -E telescope was also used consisting of a silicon detector 20  $\mu\text{m}$  thick followed by a second one 200  $\mu\text{m}$  thick. A representative  $\Delta E$ -E spectrum from the energy at 22.0 MeV is presented in Figure 2.4, where the only contour appearing in the spectrum is the  ${}^7\text{Be}$  one.

### 2.2.2 Parallel Plate Avalanche Counters

The two PPAC detectors [137, 139] of the EXOTIC beam line, developed by INFN-Napoli, are X-Y position sensitive detectors with tolerance to counting rates up to  $\sim 10^6$  Hz for RIBs in

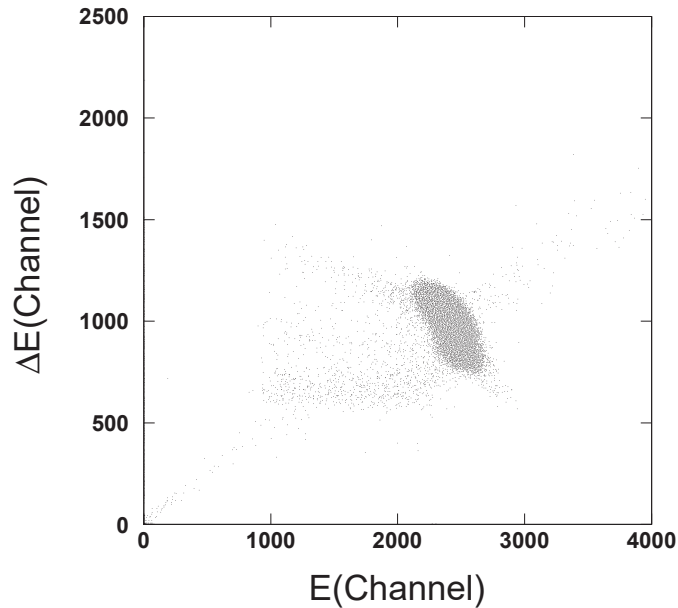


Figure 2.4: A typical  $\Delta E$ - $E$  spectrum at the energy of 22.0 MeV from the telescope mounted on the target ladder. It is obvious that the possible beam contaminants were successfully suppressed.

the energy regime of (3-5) MeV/u. The first PPAC (PPAC<sub>A</sub>) is located 909 mm upstream the secondary target, while the second one (PPAC<sub>B</sub>) is located at the entrance of the scattering chamber, 365 mm upstream the secondary target. The PPAC detector has an active area of (62 × 62) mm<sup>2</sup> and is usually operated with isobutane (C<sub>4</sub>H<sub>10</sub>) at a pressure of 10 to 20 mbar. Each PPAC consists of a cathode plate between two anodes. The cathode plate is made of a mylar foil 1.5 μm thick with an extra layer of 30 nm aluminum evaporated on both sides of the mylar. Each anode consists of 60 wires 20 μm thick with 1 mm spacing from each other. The two anodes are placed perpendicular to each other ensuring a position resolution of 1 mm(X) × 1 mm(Y). The anode wires are connected to a 2.3 ns/mm delay line. The charge collected by the anodes produces a signal travelling towards the delay line (see Figure 2.5). Reaching the delay line, the signal is splitted in two directions (Left-Right or Up-Down) travelling simultaneously towards the two ends (X<sub>1</sub> and X<sub>2</sub> or Y<sub>1</sub> and Y<sub>2</sub>). The time interval that the signal needs to reach each end is measured with a **T**ime to **D**igital **C**onverter (TDC), using as a start the signal from the cathode, while the stop signal is provided by each end. The time difference of the arrival time of the signal between the the two ends of the delay line is proportional to the position of the particle. Absolute measurements of the position of the particles are obtained after calibrating the PPAC's as follows. Almost all the active area of a PPAC is irradiated by the secondary beam. Thus, by plotting the differences (X<sub>1</sub> - X<sub>2</sub>) or (Y<sub>1</sub>

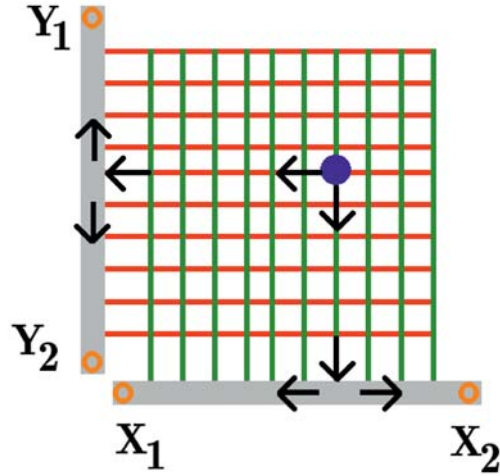


Figure 2.5: The position determination on a PPAC detector through the anodes signals. A group of electrons, designated with the blue dot, produces a signal that travels through the anode wires towards the delay lines, depicted with the grey bars. The signal (black arrow) arriving at the delay line is splitted in two directions, travelling towards  $X_1$  and  $X_2$  or  $Y_1$  and  $Y_2$  outputs. The time differences  $(X_1 - X_2)$  and  $(Y_1 - Y_2)$  are proportional to the X and Y position respectively.

-  $Y_2$ ), in principle, it is expected to observe in the spectrum a number of peaks equal to the number of the anode wires producing the signals. Since the spacing between two wires is known (1 mm), the distance between two neighbor peaks in the spectrum is converted from channels into millimeters and the position of the particles is deduced. Representative calibrated spectra of PPAC<sub>A</sub> for the time differences  $(X_1 - X_2)$  and  $(Y_1 - Y_2)$  from the present experiment are presented in Figure 2.6. After the determination of the X and Y positions, the beam profile can be reconstructed by plotting the  $(Y_1 - Y_2)$  versus  $(X_1 - X_2)$ . The relevant spectra for both PPAC's are shown in Figure 2.7. In addition to the beam profile monitoring, the two PPAC's provided the information for an event by event reconstruction of the beam particle trajectories as well as the trajectories of the scattered particles from the target to the **Double Sided Silicon Strip Detectors** (DSSSD's). This information proved to be very useful for the analysis of the elastic scattering data which are very sensitive to a possible misalignment of the beam at the target position. It was implemented in an event by event analysis code, developed in our laboratory, for the exact determination of the scattering angle for each one of the events. Details about this code are given on the Appendix A.

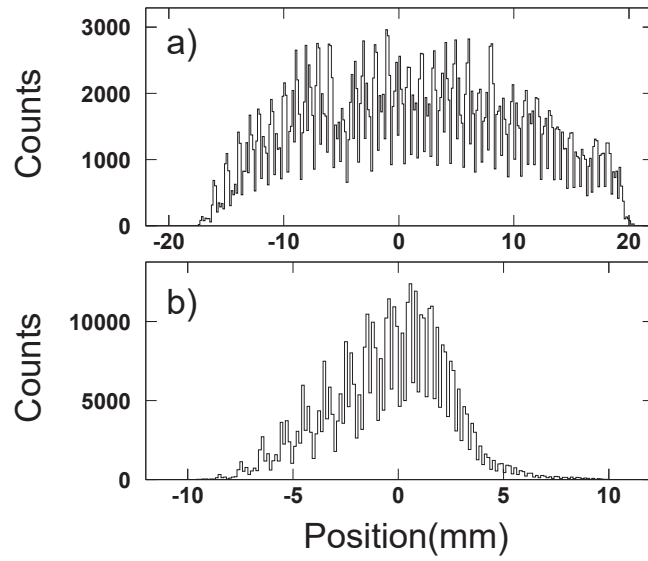


Figure 2.6: a) The determination of X position on PPAC<sub>A</sub> for the  ${}^7\text{Be}$  beam at the energy of 22.0 MeV. b) The determination of Y position on PPAC<sub>A</sub> for the  ${}^7\text{Be}$  beam at the energy of 22.0 MeV.

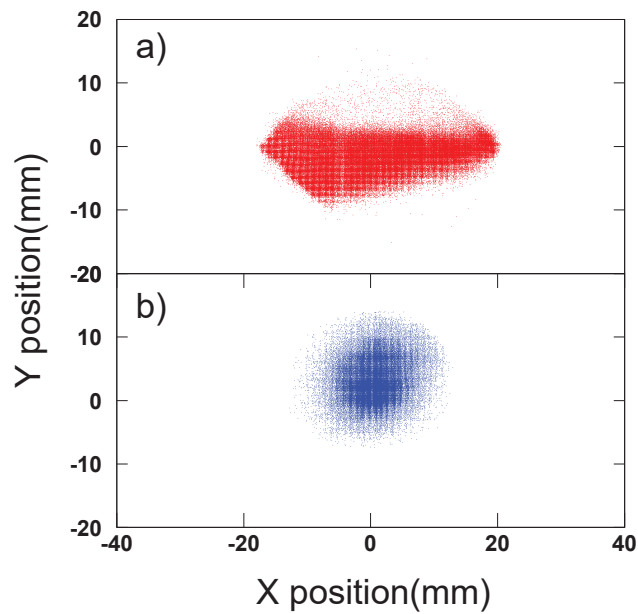


Figure 2.7: a) The  ${}^7\text{Be}$  beam profile as it was recorded on PPAC<sub>A</sub> at the energy of 22.0 MeV. b) The  ${}^7\text{Be}$  beam profile as it was recorded on PPAC<sub>B</sub> at the energy of 22.0 MeV.

### 2.2.3 Double Sided Silicon Strip Detectors (DSSSD) and the EXPADES array

The advent of radioactive beam facilities moved the interest to measurements involving exotic nuclei especially at near barrier energies, where the direct mechanisms are expected to be of great importance creating a very interesting field for studies of reaction mechanisms and channel coupling effects. Since the RIBs are usually produced with lower intensities than the stable ones, a detector system covering a large solid angle together with high granularity is required. These features are met in the DSSSD arrays (Double Sided Silicon Strip Detectors).

A DSSSD is consisted of an n-type silicon layer having implanted  $p^+$  silicon strips on the one side (front) and  $n^-$  silicon strips on the other side (back) [141, 142]. The  $p^+$  indicates that the crystal is highly doped with impurities increasing the population of the holes, while  $n^-$  indicates that the crystal is doped with impurities such as there is an excess of free electrons. In the space between the series of  $n^-$  strips, thinner  $p^+$  silicon strips are implanted for electrical isolation purposes. A reverse biased voltage is applied over the detector, creating an electric field throughout the n-type silicon layer that prevents the recombination of the electrons and holes, leading to the formation of the so called **depletion region**. When a charged particle passes through the detector, electron-hole pairs are formed in the depletion region. Then, both charge carriers are moving in opposite directions producing two coincidence signals. Each strip is connected to its own amplifier and so, the coincidence signal from a single event is amplified and through the readout electronics the energy loss of the ion as well as its position in the detector are determined.

The past few years, a large number of DSSSD arrays like EXPADES [138, 139], GLORIA [143, 144], MUST2 [145, 146], TIARA [147], LASSA [148], HiRA [149] and LEDA [150] were developed dedicated to measurements with stable or radioactive beams. In the present study the DSSSD array of the EXOTIC facility, EXPADES (**EX**otic **PA**rticle **DE**tection **S**ystem) was used. EXPADES is a detector array of eight telescopes, each one comprised by two DSSSD's with the possibility to use also an ionization chamber (IC). In the present experiment the IC part was not available therefore, the main focus will be given on the description of the DSSSD's. The  $\Delta E$  stage of the telescopes is a DSSSD (45-60) $\mu\text{m}$  thick detector, while the E stage is a DSSSD  $\sim 300 \mu\text{m}$  thick detector. The DSSSD's have active areas of  $(64 \times 64) \text{ mm}^2$  with 32 strips per side. The y strips, providing the information of Y position, are implanted on the front side of the detector and are orthogonally oriented with respect to the the x strips on the back side, providing the information of X position. Thus, pixels of  $(2 \times 2) \text{ mm}^2$  are

defined. The signal readout electronics for the  $\Delta E$  stage of the telescopes are different from those for the E one as explained in [138, 139]. A short description for both types of electronics is given below.

At the  $\Delta E$  stage of the detector, both x and y strips were short-circuited two-by-two in order to reduce the cost as well as complexity of the signal handling. The  $\Delta E$  electronics readout were developed by INFN-Milano and include a charge sensitive preamplifier and an amplifier module called **MEGAMP** [151]. The preamplifier module has 16 input channels and it generates 16 differential output signals, fed as an input to the MEGAMP. The MEGAMP amplifier has 16 input channels where each one provides information both for energy and time. The energy information is provided from a spectroscopy amplifier. The signal is amplified properly by means of a 2-bit coarse gain stage followed by an 8-bit fine gain stage and then is sent to the ADC module. The time information is provided using two **C**onstant **F**raction **D**iscriminators (CFDs) and a **T**ime to **A**nalog **C**onverter (TAC). The CFDs provide an output signal at 30% and 80% of the signal leading edge. The 30% CFD output provides the START signal to the TAC unit, while the STOP signal is provided either by the 80% CFD output or an external signal. Using as STOP the 80% CFD signal the TAC unit provides a pulse shape information, while an external signal may be used for Time Of Flight (TOF) measurements. The block diagram for a single channel of the MEGAMP is displayed in Figure 2.8.

Regarding the E stage, the readout electronics include 32-channel ASIC chips (VA and TA) installed on a board (VA-TA board), designed by INFN-Padova, for each side of the detector (front and back). The development of the electronics was based on similar work described in Refs. [149, 152]. The VA chip is employed for the treatment of the energy signal and the TA chip for the treatment of the logic signal. The VA chip is consisted of a charge sensitive preamplifier followed by a slow amplifier and a Sample and Hold unit. In contrast to the MEGAMP module, the amplification via the VA chip is common for all strips and can be set at four discrete values allowing a dynamic range for the detector of 30, 52, 90 and 113 MeV. After the amplification stage, the signals from all the strips are combined into one through a multiplexer (MUX) and the final signal is sent to the ADC. The TA chip is comprised of a fast shape unit followed by a discriminator, where its output signal is sent to the Trigger Supervisor (TSB) which is responsible for the trigger logic. The block diagram for a single channel of the VA-TA board is illustrated in Figure 2.9. These are in short the main features of the electronics for the  $\Delta E$ -E telescopes of the EXOTIC facility. Further details are given in Ref. [139].

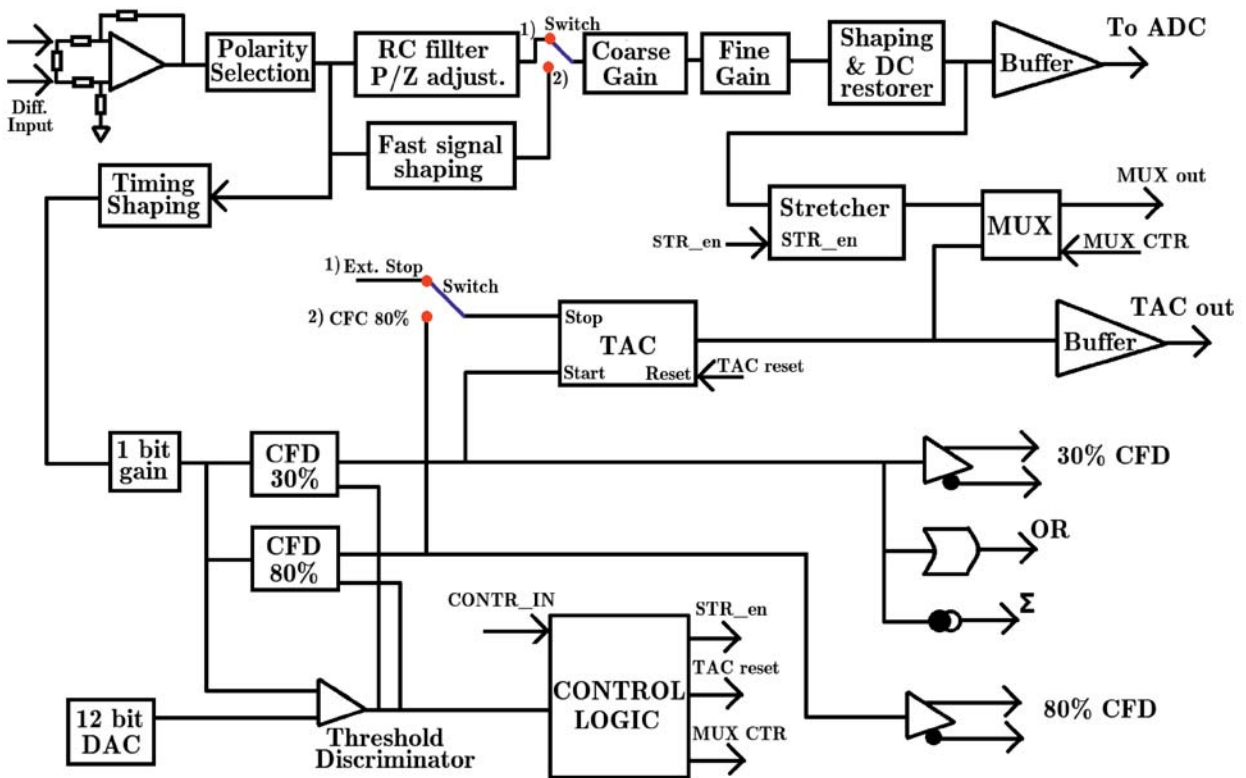


Figure 2.8: The block diagram of the MEGAMP amplifier for a single channel - Figure from Ref. [139].

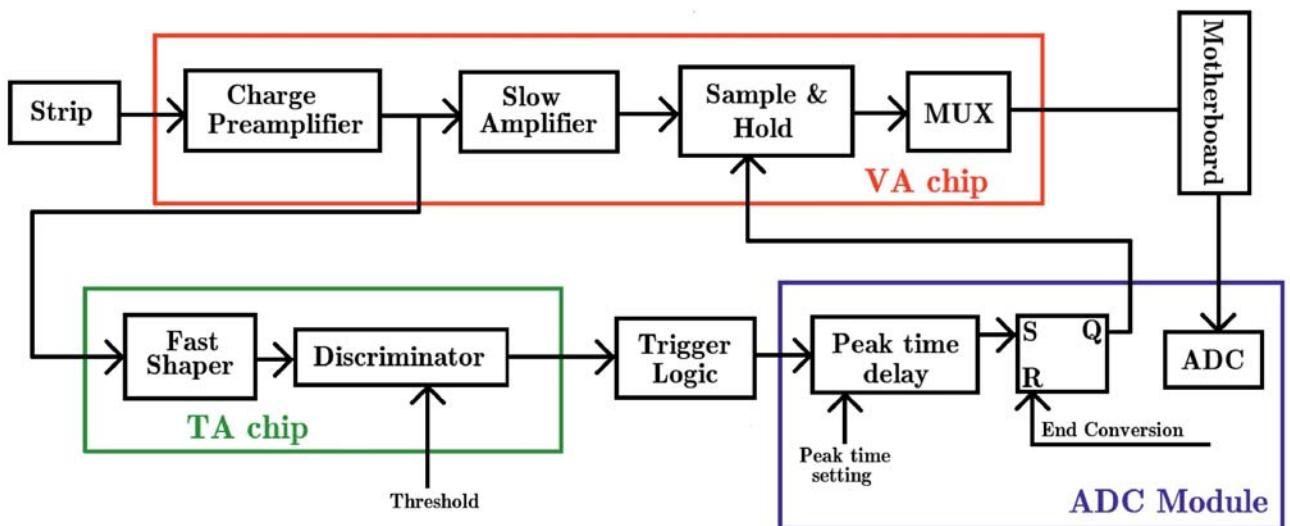


Figure 2.9: The block diagram of the VA-TA board for a single channel - Figure from Ref. [139].

## 2.2.4 The trigger of the experiment

In the previous Subsection, a short description about the EXPADES array and its electronics was presented. Further on, the main concept of the experimental design is the trigger of the electronics. The trigger is controlled via the Trigger Supervisor (TSB) board. The TSB accepts the OR signals of the x and y strips from both stages of the  $\Delta E$ -E telescopes. Also, signals from external sources, usually from PPAC's, are fed as an input to the TSB. The TSB board includes four different stages: The first stage receives the signal from all the DSSSD's. The second stage receives the signal from the external sources together with the output of the first stage. In the third stage, the output of the second stage is used to create further logic and in the final stage, the so called **Master Trigger** signal for the chain of the electronics is generated. In our case, the Master Trigger of the experiment was created as the logical AND between the OR signal of the  $\Delta E$  stage of the telescopes and the signal from the cathode of PPAC<sub>A</sub>. Under normal circumstances, the PPAC<sub>A</sub> signal precedes the signal from the DSSSD's. Thus, the signal from the cathode of PPAC<sub>A</sub> was delayed by 200 ns, such as the two signals were overlapped within a certain time window.

## 2.3 Experimental setup and procedure

In the present experiment, six telescopes from the EXPADES array were used with the following standard configuration. The forward telescopes T1 and T6 were set at  $\pm 27^\circ$ , the middle telescopes T2 and T5 at  $\pm 69^\circ$  and the backward ones T3 and T4 at  $\pm 111^\circ$ , covering the following angular ranges:  $\sim (13^\circ \text{ to } 41^\circ)$  and  $\sim (14^\circ \text{ to } 40^\circ)$  for the forward telescopes,  $\sim (54^\circ \text{ to } 85^\circ)$  for the middle telescopes and  $\sim (96^\circ \text{ to } 126^\circ)$  for the backward telescopes. The telescopes were set at symmetrical positions to balance any beam divergence and to improve the statistics of the measurement. A schematic view of the experimental setup is displayed in Figure 2.10, while a photo with the telescopes mounted in the scattering chamber appears in Figure 2.11. In the center of the scattering chamber, a target ladder was installed with several available positions (Figure 2.12). In the present experiment, three kinds of targets were used. For the main measurement, two  $^{28}\text{Si}$  targets  $0.4 \text{ mg/cm}^2$  and  $0.6 \text{ mg/cm}^2$  thick were used, the second one for the measurement at the energy of 17.2 MeV. In addition, the thick silicon and a  $^{208}\text{Pb}$  target ( $2 \text{ mg/cm}^2$ ) were used at the energies of 9.0 and 22.0 MeV respectively for the solid angle determination, since the scattering at such energies is of Rutherford type.

For the needs of the present study, the  $^7\text{Be}$  secondary radioactive beam was produced by

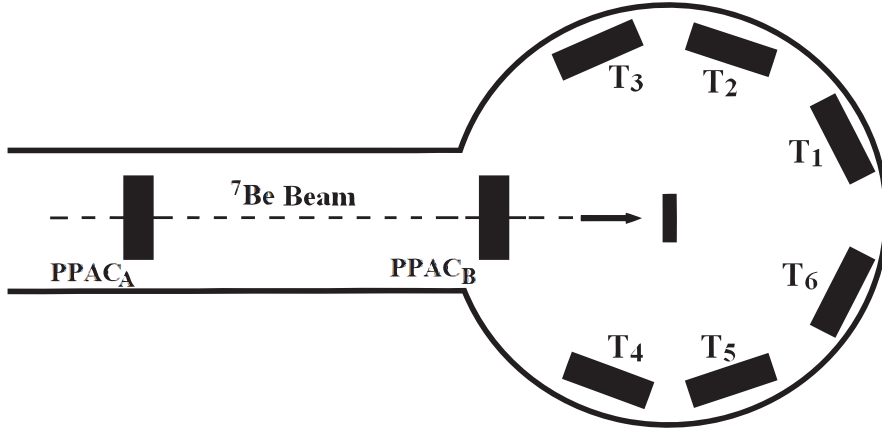


Figure 2.10: Schematic view of the experimental setup which includes 6 of the 8 modules of the EXOTIC array EXPADES [138, 139]. Each module includes two DSSSD's as explained in the text. Telescopes T1 and T6 were set at  $\pm 27^\circ$ , T2 and T5 at  $\pm 69^\circ$  and T3 and T4 at  $\pm 111^\circ$ , covering the following angular ranges:  $\sim 13^\circ$  to  $41^\circ$  and  $\sim 14^\circ$  to  $40^\circ$  for the forward telescopes,  $\sim 54^\circ$  to  $85^\circ$  for the middle telescopes and  $\sim 96^\circ$  to  $126^\circ$  for the backward telescopes.

means of the  $^1\text{H}(^7\text{Li},^7\text{Be})\text{n}$  reaction. The  $^7\text{Li}$  primary beam with an intensity of 150 pA, produced at three energies namely 26, 31 and 33 MeV, impinged on a  $\text{H}_2$  gas primary target at a pressure of 1 bar and a temperature of 93 K corresponding to an effective thickness of  $1.35 \text{ mg/cm}^2$ . The  $^7\text{Be}$  beam was produced at five near barrier energies namely 9.0, 13.2, 17.2, 19.8 and 22.0 MeV, the highest three being obtained by re-tuning the primary beam while the lowest two using an  $^{27}\text{Al}$  degrader at the energies of 19.8 and 17.2 MeV. After the gas target, the  $^7\text{Be}$  beam was directed into a series of optical elements, slits sets and collimators placed along the beam line, allowing the separation of  $^7\text{Be}$  from the scattered  $^7\text{Li}$  ions and possible  $^4\text{He}$  contaminations from the  $^1\text{H}(^7\text{Li},^4\text{He})^4\text{He}$  reaction, as it was explained in Section 2.1. In the present experiment, the average  $^7\text{Be}$  beam intensity was  $\sim 5 \times 10^4$  pps on the target position.

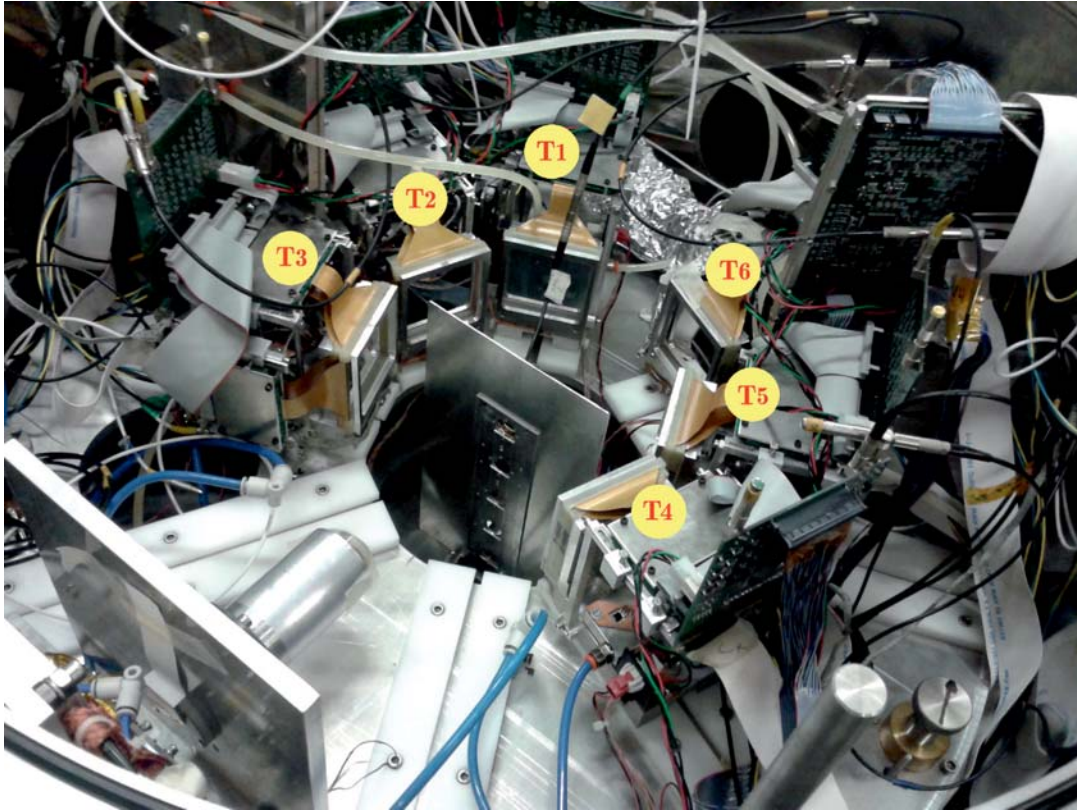


Figure 2.11: A photo of the detectors' arrangement inside the scattering chamber.

Table 2.2: The information regarding the telescopes arrangement inside the scattering chamber. The first column indicates the telescope identity, the second one includes the distances of each telescope with respect to the target position, the third column includes the mean angle of each telescope, while the last one the angular range covered by each telescope.

| Telescope ID | Distance from the target (mm) | Mean angle (deg) | Angular range (deg) |
|--------------|-------------------------------|------------------|---------------------|
| T1           | 123.0                         | 27.0             | 13.0 - 41.0         |
| T2           | 111.0                         | 69.0             | 53.5 - 84.5         |
| T3           | 115.0                         | 111.0            | 94.8 - 127.2        |
| T4           | 106.0                         | 111.0            | 96.1 - 126.0        |
| T5           | 111.0                         | 69.0             | 53.5 - 84.5         |
| T6           | 134.0                         | 27.0             | 14.2 - 39.8         |

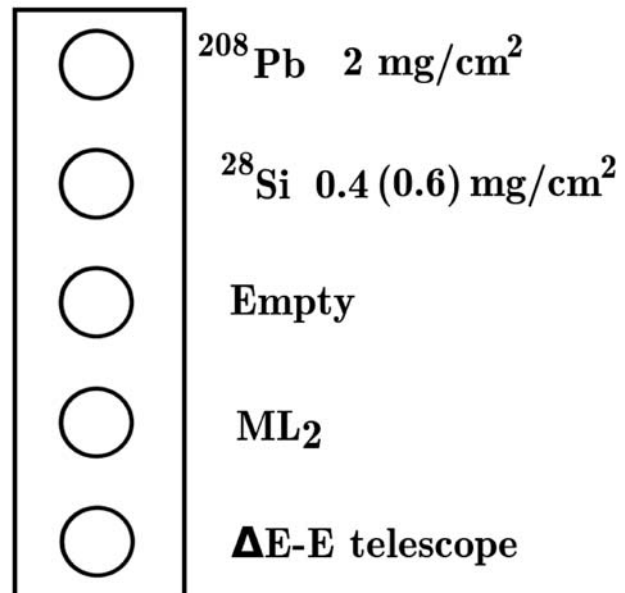


Figure 2.12: *Schematic representation of the target ladder used in the present experiment.*



# Chapter 3

## Data Reduction

In order to deduce the optical potential and map its energy evolution, elastic scattering angular distribution data were determined at various near barrier energies, namely 13.2, 17.2, 19.8 and 22.0 MeV ( $E/V_{C.b.} = 1.14, 1.48, 1.71, 1.90$ ). Further on, the degree of competition between direct and the compound nucleus mechanisms was sought by considering the  $^3\text{He}$  and  $^4\text{He}$  reaction products. For that, experimental angular distributions together with direct and compound nucleus calculations were used, as the tool for disentangling the various mechanisms. In the following, details about the data reduction are presented, leading to differential cross sections either for the elastically scattered  $^7\text{Be}$  ions (Section 3.2) or the  $^3,4\text{He}$  reaction products (Section 3.3).

### 3.1 Energy calibration

For the identification of the reaction products, especially in the present case where the elastically scattered ions stop in the first stage of the telescope, an accurate energy calibration of the detectors is necessary. In order to span the whole dynamical range of them, the calibration was performed by using a pulser in combination with a triple alpha source ( $^{239}\text{Pu}$ ,  $^{241}\text{Am}$ ,  $^{244}\text{Cm}$ ). The pulser generator was calibrated through the alpha source and the detectors through the pulser. Thus, the accuracy of the calibration was extended in a wide energy range. Representative spectra for the calibration of one strip of the  $\Delta E$  stage of telescope T6 are displayed in Figure 3.1.

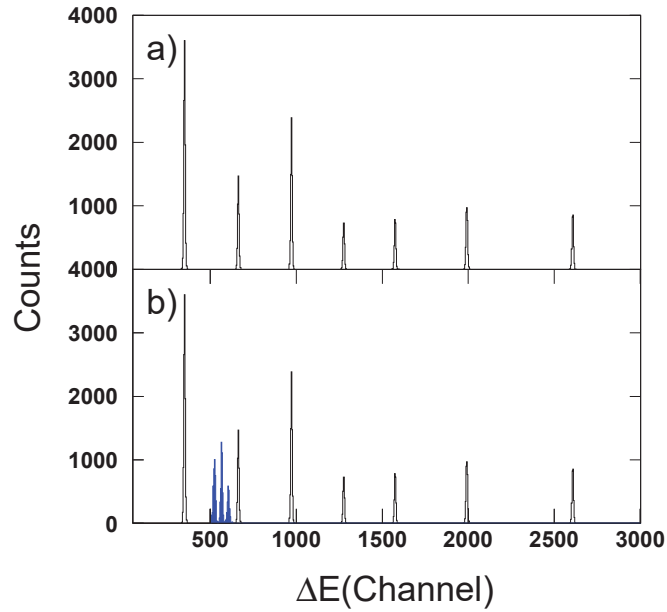


Figure 3.1: Calibration spectra collected by one strip of the  $\Delta E$  stage of telescope T6. a) A pulser spectrum spanning a wide energy range. b) A pulser spectrum together with the peaks corresponding to the triple alpha source decay which are denoted with the blue color.

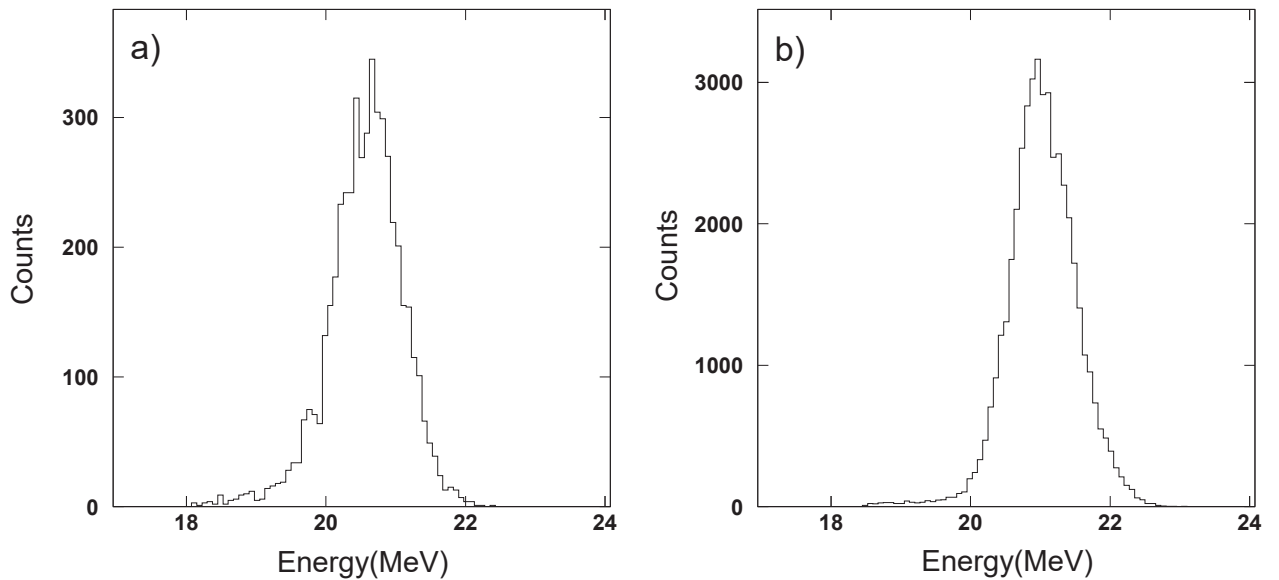


Figure 3.2: Representative energy spectra for the elastic scattering of  ${}^7\text{Be}$  on (a)  ${}^{28}\text{Si}$  and (b)  ${}^{208}\text{Pb}$  at the beam energy of 22.0 MeV. These spectra were recorded by one strip of the  $\Delta E$  stage of telescope T1, corresponding to a  $\theta_{lab} = 22.3^\circ$ .

## 3.2 Determination of the elastic scattering cross sections

The elastically scattered  ${}^7\text{Be}$  ions were stopped in the first stage of the telescope and were identified taking into account the kinematics of the colliding ions and the energy loss, using the programs NRV [153] and LISE++ [154]. A typical one dimensional energy spectrum from a telescope set at forward angles is shown in the left panel of Figure 3.2. As it is seen, the peak is well pronounced and no other events are present near by. This is because, the other light reaction products did not stop in this detector but punched through, therefore leaving very little energy in it. At this point it should be mentioned that the data in the present analysis refer to quasi - elastic scattering, since excitations to the  $1/2^-$  state of  ${}^7\text{Be}$  (0.429 MeV) or the  $2^+$  state of  ${}^{28}\text{Si}$  (1.779 MeV) could not be resolved from pure elastic scattering events.

The reduction of the quasi - elastic scattering events was performed by means of an event by event code, developed in our laboratory, using the data analysis package ROOT [155]. Details of this code will be given in Appendix A. Briefly we can refer on that as following. Experimentally the coordinates for each beam particle are determined in two places via the information collected by the two PPAC's. This information is implemented in our code and via analytic geometry, the beam particle trajectories are reconstructed. In this respect, the reaction position on the target is defined for each event. Subsequently, the DSSSD telescopes provide the position of each elastically scattered particle, since each event is detected in a unique pixel of the detector. By using the coordinates of the reaction position on the target together with the coordinates of the events detected in the DSSSD's, the scattering angle for each event can be determined.

Data concerning both the quasi - elastic scattering of  ${}^7\text{Be}$  on  ${}^{28}\text{Si}$  and  ${}^{208}\text{Pb}$  were treated in an event by event framework. Events with the same angle or with an angle inside an angular range corresponding to a particular strip of each EXPADES detector were summed up. The so performed event by event analysis, reported in Ref. [156], improved greatly our preliminary strip or/and pixel analysis reported previously in [157]. The ratios  $\sigma/\sigma_{Ruth}^{Si}$  were deduced according to the following expression:

$$Ratio \equiv \frac{\sigma}{\sigma_{Ruth}^{Si}} = \frac{N_{Si}}{N_{Pb}} * K \quad (3.1)$$

where  $N_{Si}$  and  $N_{Pb}$  are the event by event counts corresponding to every strip collected with

the silicon and lead targets respectively and the constant K corresponds to

$$K = \frac{T_{Pb} \Phi_{Pb} \sigma_{Ruth}^{Pb}}{T_{Si} \Phi_{Si} \sigma_{Ruth}^{Si}} \quad (3.2)$$

where  $T_{Si}$  and  $T_{Pb}$  are the scattering centers of the silicon and lead targets respectively,  $\Phi_{Si}$  and  $\Phi_{Pb}$  are the beam fluxes during the runs with the silicon and lead targets respectively and  $\sigma_{Ruth}^{Si}$  and  $\sigma_{Ruth}^{Pb}$  are the calculated Rutherford cross sections for the elastic scattering of  ${}^7\text{Be}$  on  ${}^{28}\text{Si}$  and  ${}^{208}\text{Pb}$  respectively. In case of the 17.2 MeV data, the main quasi - elastic scattering data were combined with quasi - elastic scattering data at 9.0 MeV where the scattering can be considered as Rutherford, and not with data from the lead target. Thus, Equations 3.1 and 3.2 were slightly modified, where  $N_{Pb}$  was replaced with  $N_9^{Si}$  and  $T_{Pb}$  was replaced with  $T_{Si}$ , with  $N_9^{Si}$  being the event by event counts corresponding to every strip collected with the silicon target at 9.0 MeV and  $T_{Si}$  are the scattering centers of the silicon target. In this particular case, Equation 3.2 is reduced to Equation 3.3.

$$K = \frac{\Phi_{Pb} \sigma_{Ruth}^{Pb}}{\Phi_{Si} \sigma_{Ruth}^{Si}} \quad (3.3)$$

The constant K is determined assuming that at small scattering angles the ratio  $\sigma/\sigma_{Ruth}^{Si}$  between elastic scattering cross sections and Rutherford cross sections is 1.0. This assumption is valid only at the lowest energy of 13.2 MeV. For the rest of the energies the ratio was assumed to be closed to 1, according to the theoretical calculations. As a result, the error assigned to our data, except systematic errors, is connected solely with the statistical errors from the measurements with the silicon and lead targets and not with errors due to the beam flux or the target thickness. The error in the ratio was calculated as:

$$\Sigma = \pm Ratio * \left( \sqrt{\frac{1}{N_{Si}} + \frac{1}{N_{Pb}}} \right) \quad (3.4)$$

The results for the quasi - elastic scattering of  ${}^7\text{Be}+{}^{28}\text{Si}$  at the energy of 22.0, 19.8, 17.2 and 13.2 MeV are presented in Figures 3.3, 3.4, 3.5 and 3.6 respectively. Differential cross sections were determined via weighted means of data, collected by telescopes placed at symmetrical positions. Weighted mean cross sections, were evaluated through the expression:

$$(\text{Ratio})_{mean} = \frac{\sum_i \frac{(\text{Ratio})_i}{\Sigma_i^2}}{\sum_i \frac{1}{\Sigma_i^2}} \quad (3.5)$$

and the error in the weighted mean was deduced as:

$$(\Sigma)_{mean} = \pm \sqrt{\frac{1}{\sum_i \frac{1}{\Sigma_i^2}}} \quad (3.6)$$

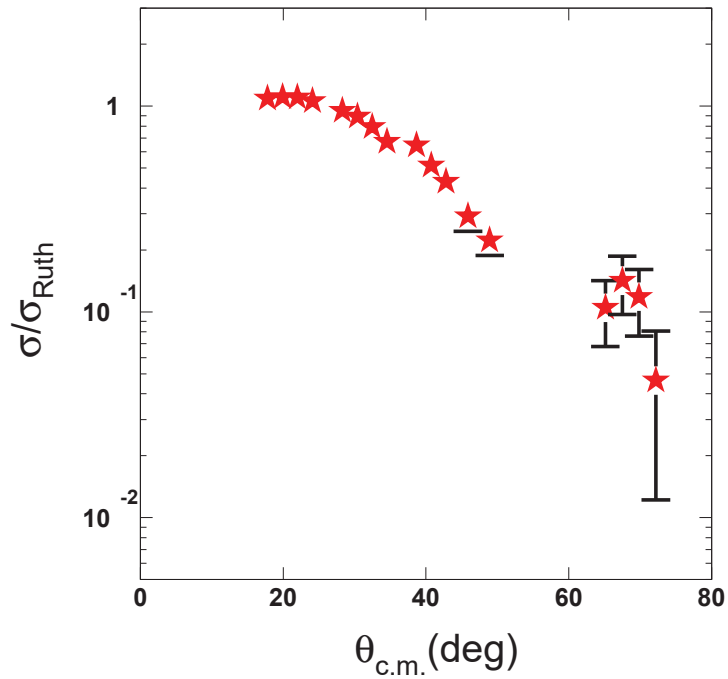


Figure 3.3: Present angular distribution data for the quasi - elastic scattering of  ${}^7\text{Be}+{}^{28}\text{Si}$  at the energy of 22.0 MeV. Tabulated values of the ratios are given in Appendix C.

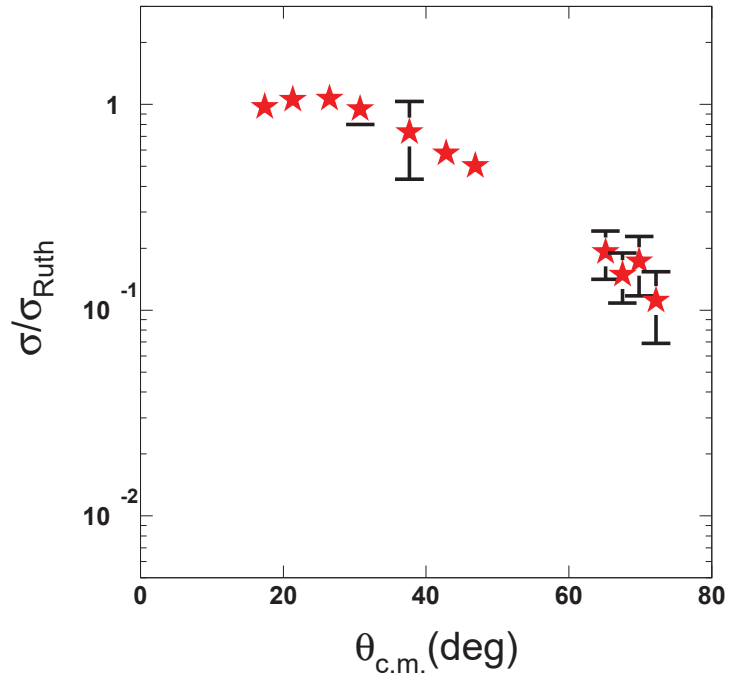


Figure 3.4: Same as in Figure 3.3 but for the energy of 19.8 MeV. Tabulated values of the ratios are given in Appendix C.

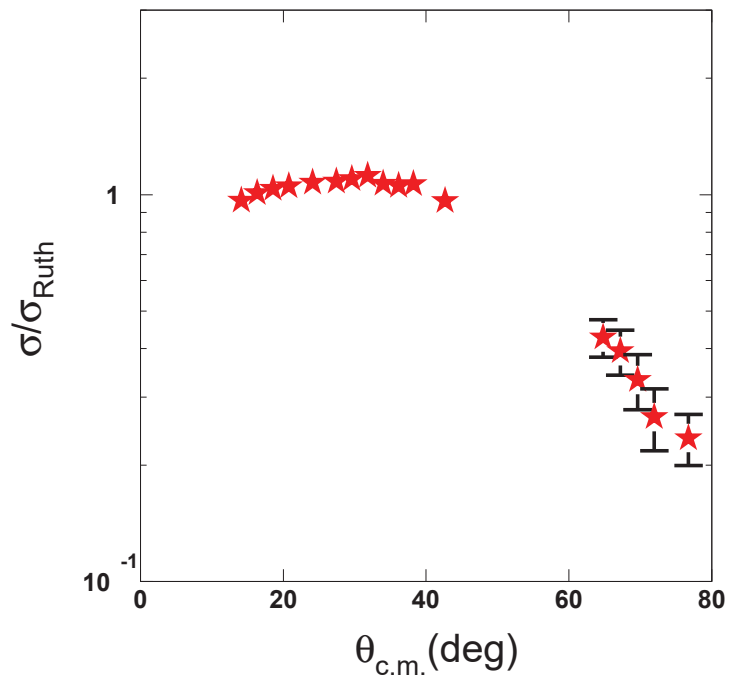


Figure 3.5: Same as in Figure 3.3 but for the energy of 17.2 MeV. Tabulated values of the ratios are given in Appendix C.

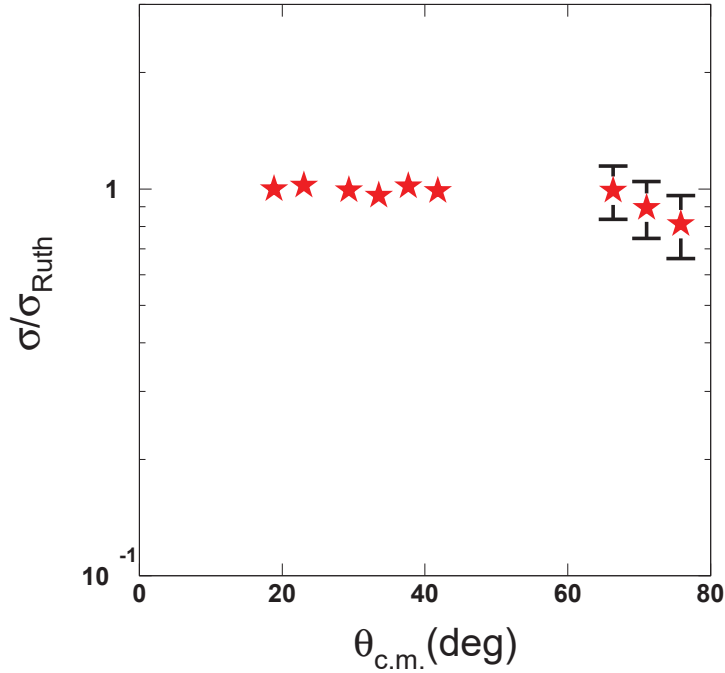


Figure 3.6: *Same as in Figure 3.3 but for the energy of 13.2 MeV. Tabulated values of the ratios are given in Appendix C.*

The quasi - elastic scattering data were treated in an Optical Model and a Continuum Discretized Coupled Channels (CDCC) framework to be described in Chapter 4.

### 3.3 Determination of the reaction cross sections

Our reaction analysis refers to the production of  ${}^3\text{He}$  and  ${}^4\text{He}$  either through a direct or a compound nucleus process. These light particles were able to pass through the  $\Delta E$  stage of the telescopes and thus, they were well-discriminated by the  $\Delta E$ -E technique (see Appendix E) as may be seen in Figure 3.7. Light particles with low energy that stopped in the first stage of the telescopes were retrieved via simulations as it will be described below. The reaction mechanisms leading to the production of  ${}^3\text{He}$  are:

1. Projectile breakup:  ${}^7\text{Be} \rightarrow {}^3\text{He} + {}^4\text{He}$ ,  $S_\alpha = 1.586$  MeV and
2.  ${}^4\text{He}$  stripping:  ${}^{28}\text{Si}({}^7\text{Be}, {}^3\text{He}){}^{32}\text{S}$ ,  $Q_{gg} = 5.36$  MeV

while those leading to the production of  ${}^4\text{He}$  are:

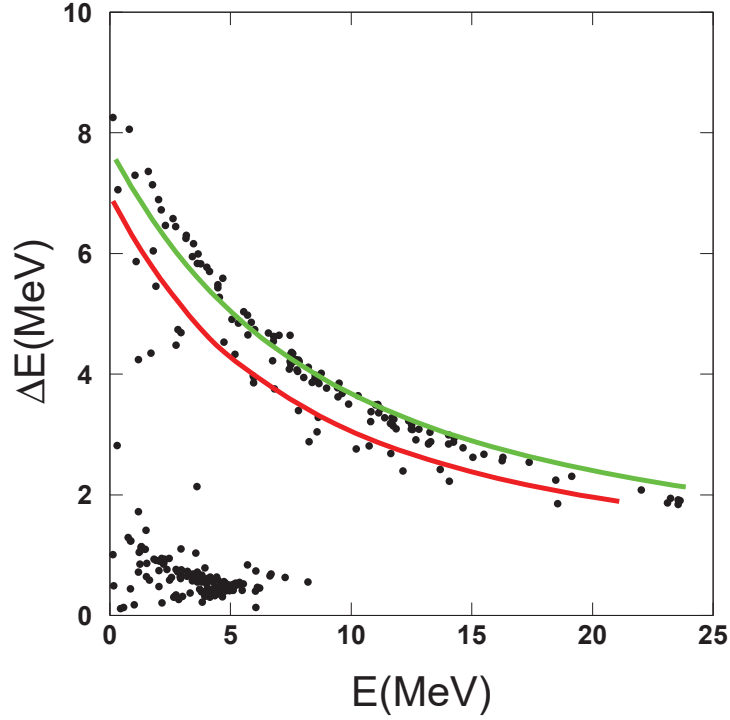


Figure 3.7: A representative  $\Delta E$ - $E$  correlation plot for telescope T1 at the energy of 22.0 MeV. The solid green and red lines represent kinematical simulations for the energy loss of  ${}^3\text{He}$  and  ${}^4\text{He}$  ions in the telescope using code LISE++ [154], presenting very good agreement with the data.

1. Projectile breakup:  ${}^7\text{Be} \rightarrow {}^3\text{He} + {}^4\text{He}$ ,  $S_\alpha = 1.586$  MeV,
2.  ${}^3\text{He}$  stripping:  ${}^{28}\text{Si}({}^7\text{Be}, {}^4\text{He}){}^{31}\text{S}$ ,  $Q_{gg} = 10.89$  MeV,
3. 1n stripping:  ${}^{28}\text{Si}({}^7\text{Be}, {}^6\text{Be}){}^{29}\text{Si}$ ,  $Q_{gg} = -2.20$  MeV,  ${}^6\text{Be} \rightarrow {}^4\text{He} + \text{p} + \text{p}$ ,
4. 1n pickup:  ${}^{28}\text{Si}({}^7\text{Be}, {}^8\text{Be}){}^{27}\text{Si}$ ,  $Q_{gg} = 1.72$  MeV,  ${}^8\text{Be} \rightarrow {}^4\text{He} + {}^4\text{He}$  and
5. Evaporation process after compound nucleus formation.

### 3.3.1 $\alpha$ - particle production cross sections

The  $\alpha$  - particle production data were analyzed via the analysis program PAW [158]. The  $\alpha$  yields were obtained by applying the appropriate energy windows on the two dimensional  $\Delta E$ - $E$  plots. However, it should be noted that due to the thickness of the  $\Delta E$  detector, an

energy threshold in the detection of the two reaction products was introduced. So, an energy phase space correction was necessary to be applied for the missing counts. This was achieved via comparisons of the experimental energy spectra with simulated ones. Simulated spectra were obtained with the contribution of all processes direct and of compound nucleus origin, normalized appropriately in a best fit. Compound nucleus energy spectra were produced via the well known code PACE2 (**P**rojection **A**ngular-momentum **C**oupled **E**vaporation) [132]. For  $\alpha$  - particles produced via a direct process, that is the neutron pickup channel leading to  ${}^8\text{Be}$  ( ${}^4\text{He}+{}^4\text{He}$ ), its inverse process leading to  ${}^6\text{Be}$  ( ${}^4\text{He}+2\text{p}$ ), the  ${}^3\text{He}$  stripping and the breakup processes, a Monte Carlo simulation code was developed to describe them. Energy spectra for most of the processes were generated by the code starting from angular distributions obtained in the DWBA framework, while for the breakup the angular distributions of the continuum states were obtained in the CDCC framework. In case of the  ${}^3\text{He}$  stripping process, no theoretical calculation was performed due to the lack of the appropriate spectroscopic factors (see Section 4.2). However, for the rest of the processes, tests adopting either specific angular distributions or isotropic ones did not affect the result for the energy spectra. Therefore, in this particular case, the simulations were performed with the assumption of an isotropic distribution. Details regarding the simulation code are given in Appendix B, while as an example, the main features of the code for the simulation of the neutron stripping process are given below.

In order to construct the alpha energy spectra from the decay of  ${}^6\text{Be}$ , the energy and the momentum of  $\alpha$  particles in the laboratory frame are necessary. In this respect, the simulation code is organized in three steps: In the first step, a theoretical angular distribution for the  ${}^3\text{He}$  stripping process, obtained in the DWBA framework using code FRESCO [98], was fed as an input to the code. Then, the emission angle  $\theta_{c.m.}$  of the  ${}^6\text{Be}$  in the center-of-mass (c.m.) frame was randomly generated, and by using the theoretical angular distribution of  ${}^6\text{Be}$  as a constrain, we evaluated the frequency of each  $\theta_{c.m.}$  to be observed. Subsequently, for each emission angle, the momentum modulus in the c.m. frame,  $P_{c.m.}$ , was calculated and subsequently the pairs  $(\theta_{c.m.}, P_{c.m.})$  were transformed in the laboratory reference system to be used in the final step of the code. In the second step, the breakup procedure takes part in the  ${}^6\text{Be}$  rest frame and the  ${}^6\text{Be}$  nucleus breaks into an  $\alpha$  particle and two protons. The  $\alpha$  particle and one of the protons are emitted with randomly specified energies and momenta and the third fragment acquires energy and momentum fulfilling the conservations laws of energy and momentum at the rest frame of  ${}^6\text{Be}$ . In the final step, following the prescription of Olimov et al. [159], by applying a Galilean transformation and an axes rotation, the alpha energy spectra from the rest frame of  ${}^6\text{Be}$  are transformed to the laboratory frame. The same or similar method was followed for the rest of the direct processes and the final energy spectrum

was obtained by summing the four energy spectra normalized to the calculated cross sections. Finally, direct and the compound nucleus spectra were summed using various assumptions for the ratio direct to compound nucleus contributions until the best fit to the experimental data was obtained. Comparisons between experimental and simulated alpha energy spectra ( $\Delta E + E$ ) are shown in Figure 3.8, while the procedure described above is demonstrated in Figure 3.9 for two representative spectra.

The integrated  $^4\text{He}$  yields for each strip, after corrections for missing counts (by comparing experimental and simulated energy spectra), were transformed to differential cross sections in the laboratory reference system via the following relation:

$$\frac{d\sigma}{d\Omega} = \frac{N_\alpha}{N_{Pb}} * K' \quad (3.7)$$

where  $N_\alpha$  is the  $^4\text{He}$  yield for each strip,  $N_{Pb}$  are the counts for each strip collected from  $^7\text{Be}$  quasi - elastic scattering to the lead target and the constant  $K'$  corresponds to

$$K' = K * \sigma_{Ruth}^{Si} \quad (3.8)$$

with  $K$  being a constant determined by the quasi - elastic scattering data as it was described in Section 3.2 and  $\sigma_{Ruth}^{Si}$  is the calculated Rutherford cross section in the laboratory reference system for the elastic scattering of  $^7\text{Be}$  on  $^{28}\text{Si}$ . The results of the analysis are presented in Figure 3.10 and they are also reported in Ref. [160].

### 3.3.2 $^3\text{He}$ production cross sections

The  $^3\text{He}$  particles are produced through direct processes as it was stated above, by breakup and  $^4\text{He}$ -stripping. In the same spirit as for the  $\alpha$  particle production, missing counts due to the energy threshold introduced by  $\Delta E$  detector were estimated via comparisons of the experimental with the simulated spectra produced by our Monte Carlo code. The results of the simulations are presented in Figure 3.11. After correcting for missing counts, the integrated  $^3\text{He}$  yields for each strip were transformed to differential cross sections in the laboratory reference system via the Equation 3.7, where  $N_\alpha$  was replaced with  $N_{^3He}$ , with the second being the  $^3\text{He}$  yield corresponding to every strip. The angular distributions for the  $^3\text{He}$  particle production are shown in Figure 3.12.

Looking at Figure 3.12, it is obvious that the  $^3\text{He}$  particle angular distributions are forward

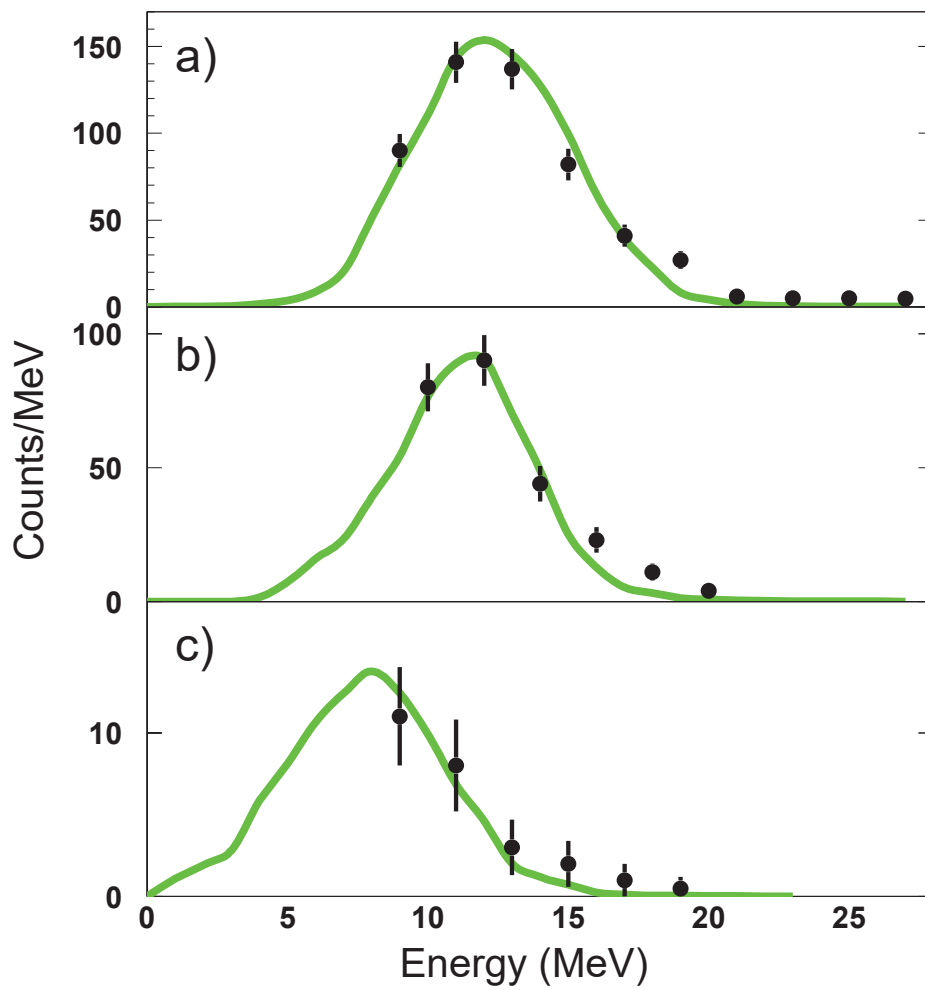


Figure 3.8: *Alpha energy spectra ( $\Delta E+E$ ) collected with telescope T1 at three energies a) 22.0 MeV, b) 19.8 and c) 13.2 MeV. The green solid line represents the simulated spectrum taking into account both direct and compound nucleus mechanisms.*

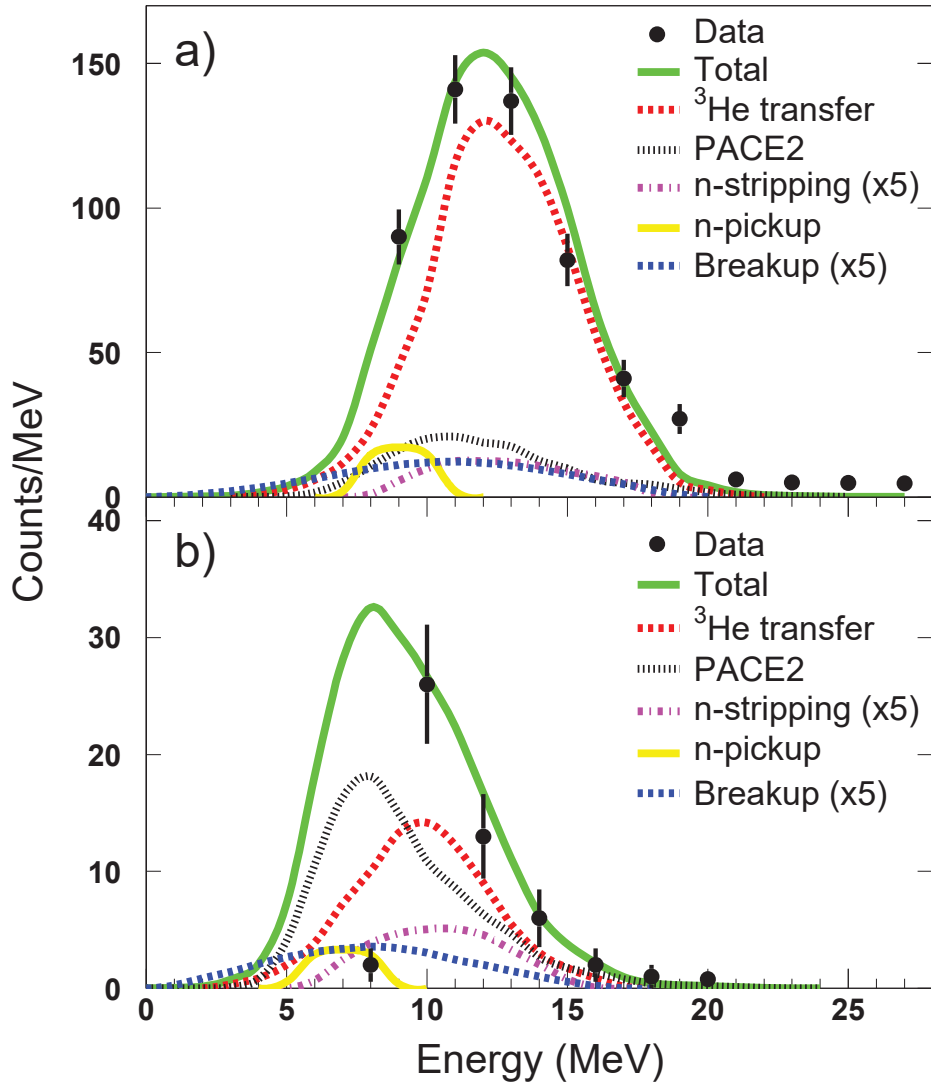


Figure 3.9: *Decomposition of the simulated alpha energy spectra at the energy of 22.0 MeV for telescopes (a) T1 and (b) T2 due to compound nucleus process, designated with the dotted black line, and direct processes as follows: The dashed red line indicates the  $\alpha$  spectrum due to  $^3\text{He}$  stripping, the dashed blue line due to breakup, the dotted-dashed magenta line due to neutron stripping and the solid yellow line due to neutron pickup. The multiplication factors are arbitrary values for the purpose of presenting the different processes only.*

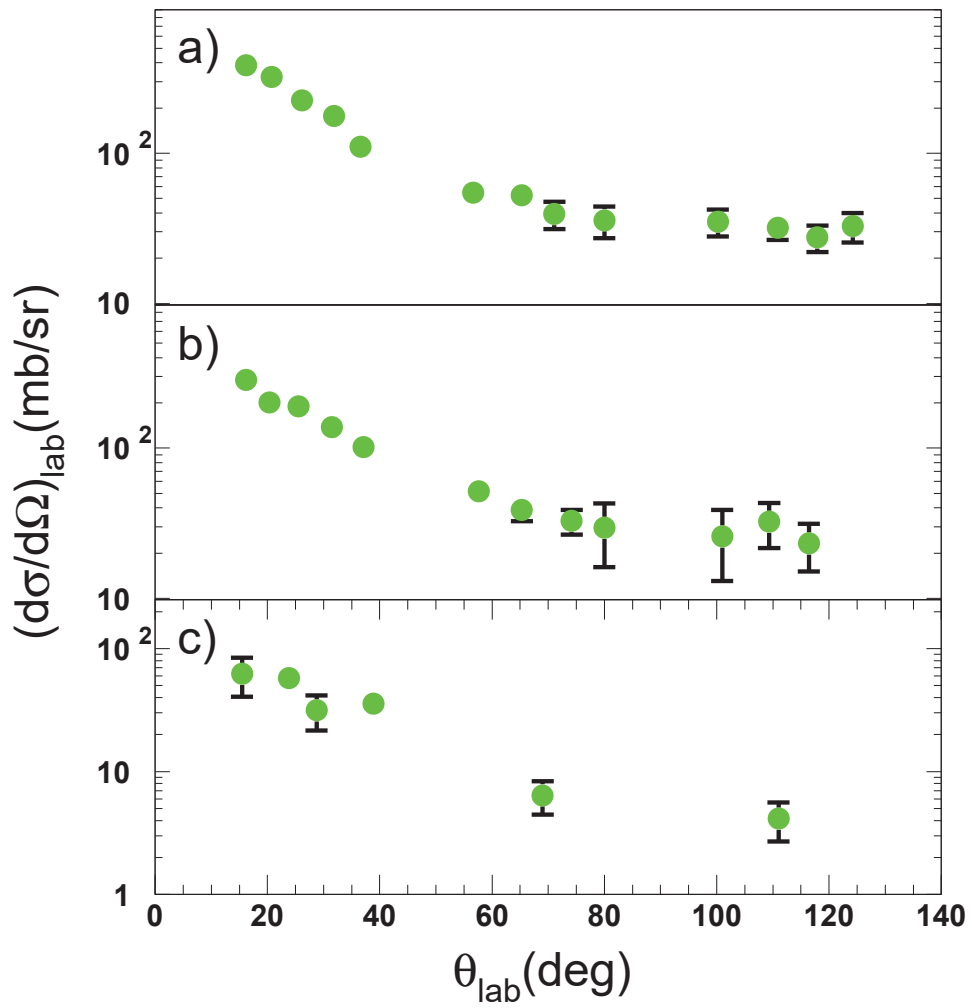


Figure 3.10: Present angular distribution data for the  ${}^4\text{He}$  particle production at the energies of a) 22.0 MeV, b) 19.8 MeV and c) 13.2 MeV. Tabulated values of the differential cross sections are given in Appendix C.

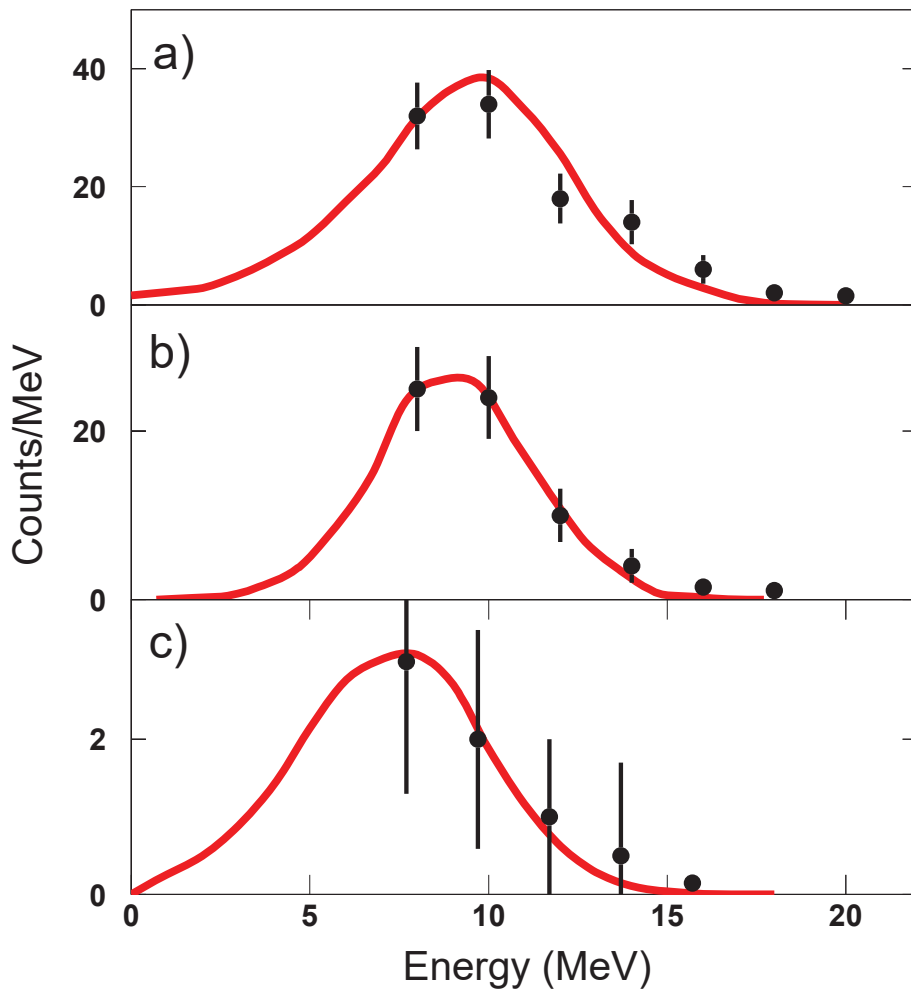


Figure 3.11:  ${}^3\text{He}$  energy spectra collected with telescope T1 at three energies a) 22.0 MeV, b) 19.8 and c) 13.2 MeV. The red solid line represents the simulated spectrum taking into account  ${}^4\text{He}$  transfer and breakup processes.

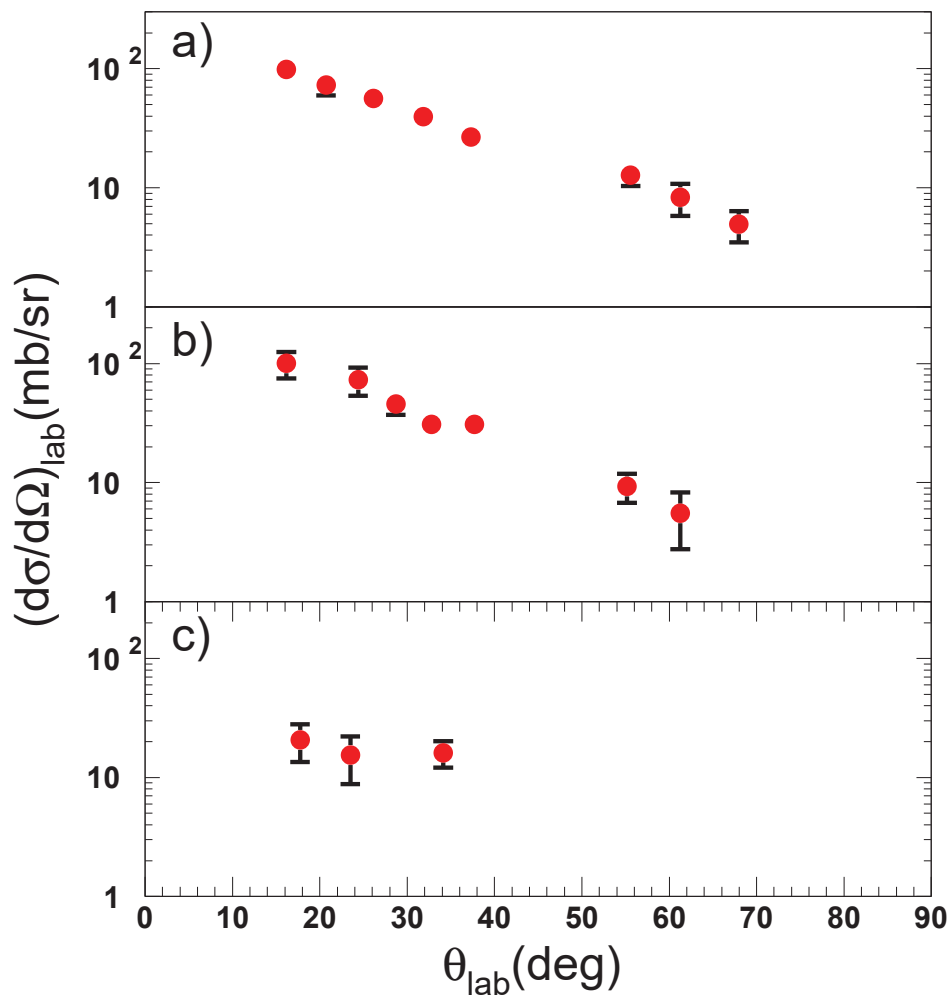


Figure 3.12: Present angular distribution data for the  ${}^3\text{He}$  particle production at the energy of a) 22.0 MeV, b) 19.8 MeV and c) 13.2 MeV. Tabulated values of the differential cross sections are given in Appendix C.

peaked. This fact points to direct mechanisms. On the other hand, the  $^4\text{He}$  particle angular distributions are forward peaked but are also extended at backward angles with substantial cross sections. This points to a more complicated situation where both direct and compound nucleus mechanisms are present. The theoretical analysis of these data is presented in the following Chapter.

# Chapter 4

## Theoretical Analysis

In the present Chapter, the theoretical analysis of the experimental angular distributions for the elastically scattered  ${}^7\text{Be}$  ions as well as the  ${}^{3,4}\text{He}$  reactions products is presented and discussed. The elastic scattering data were analyzed in a double folding framework and the energy evolution of the optical potential as well as the total reaction cross sections were deduced [156]. Further on, regarding the reaction mechanisms, angular distribution data of  $\alpha$  - particles were analyzed in statistical model, DWBA and CDCC frameworks in order to disentangle the degree of competition between direct and compound nucleus channels [160]. Subsequently, fusion cross sections were deduced taking into account  $\alpha$  - particle cross sections due to compound nucleus formation and  $\alpha$  - particle multiplicities from the statistical model calculations. Finally, angular distribution data of  ${}^3\text{He}$  particles were analyzed in the DWBA and CDCC frameworks since the only mechanisms contributing to the  ${}^3\text{He}$  production are the  $\alpha$  - stripping and the breakup. In the following, the theoretical interpretation of the elastic scattering data is presented in Section 4.1, while the relevant analysis of  ${}^{3,4}\text{He}$  reaction data is presented in Section 4.2.

### 4.1 Elastic Scattering

#### 4.1.1 Optical Model Analysis

For the Optical Model (OM) analysis we followed the same method as the one adopted for  ${}^6,7\text{Li} + {}^{28}\text{Si}$  previously [16, 17], and elastic scattering calculations were performed [161] with the code ECIS [162]. The real part of the entrance potential was derived in a double folding

model [113] adopting the microscopic BDM3Y1 interaction developed by Khoa et al. [117]. Since the density distributions of the projectile and the target are introduced in the folding procedure, the density for the  $^{28}\text{Si}$  was obtained from electron scattering data adopting a three parameter Fermi model [163]. The proton ground state densities were deconvoluted from the finite charge distribution of the constituent nucleons to obtain a point proton ground state density. Point neutron densities were taken to be  $N/Z$  times the point proton ground state densities. In case of the  $^7\text{Be}$ , its density was calculated adopting semi-phenomenological analytic expressions taking into account the asymptotic behavior and the behavior of the density at the nucleus center according to Bhagwat et al. [164].

In case of the imaginary potential, assuming that the imaginary part of the entrance potential presents the same radial dependence as the real one, the same folded potential was adopted but with a different normalization factor. During the fitting procedure, a search was performed by using as free parameters the two normalization factors  $\mathbf{N}_R$  and  $\mathbf{N}_I$  for the real and imaginary potential respectively. The best fit optical potential parameters are included in Table 4.1, while the deduced best fit angular distributions are compared with the data in Figures 4.1, 4.2, 4.3 and 4.4 for the energy of 22.0, 19.8, 17.2 and 13.2 MeV respectively. The adopted errors in the optical model parameters were deduced from a sensitivity analysis [161] performed by varying the parameters,  $N_R$  and  $N_I$ , by certain amounts. The results of the sensitivity analysis are presented in Figures 4.1 - 4.4.

Table 4.1: *Best fit optical model parameters for system  $^7\text{Be} + ^{28}\text{Si}$  for the real,  $N_R$  and imaginary,  $N_I$ , part of the optical potential. The real part of the potential was calculated in a double folding model (see text). For the imaginary part, the same potential as the real one was adopted, assuming the same radial shape.*

| Energy (MeV) | $N_R$           | $N_I$           |
|--------------|-----------------|-----------------|
| 22.0         | $0.43 \pm 0.17$ | $0.45 \pm 0.33$ |
| 19.8         | $0.43 \pm 0.18$ | $0.59 \pm 0.45$ |
| 17.2         | $0.32 \pm 0.15$ | $0.29 \pm 0.33$ |
| 13.2         | $0.63 \pm 0.25$ | $0.14 \pm 0.32$ |

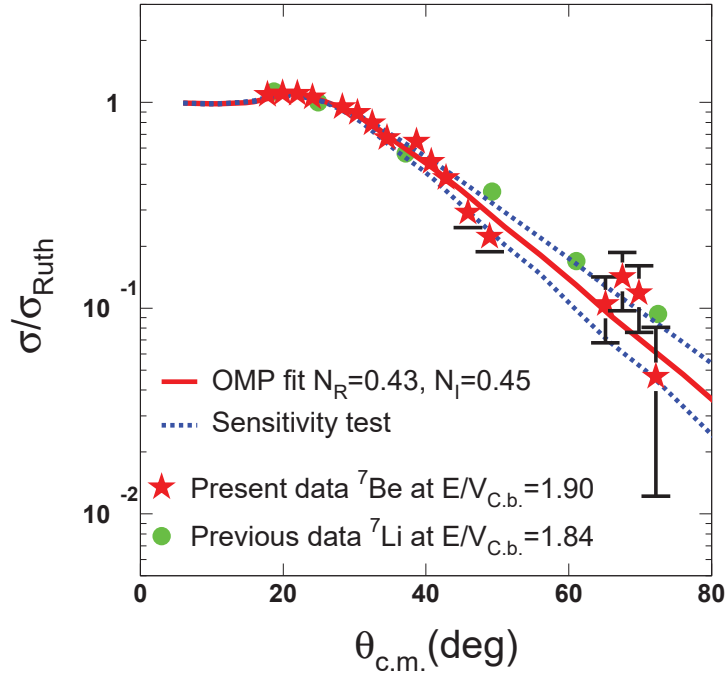


Figure 4.1: Present angular distribution data for the elastic scattering of  ${}^7\text{Be} + {}^{28}\text{Si}$  at the energy of 22.0 MeV ( $E/V_{C.b.} = 1.90$ ), designated with the red stars, are compared with previous data [17] for  ${}^7\text{Li} + {}^{28}\text{Si}$  at 16.0 MeV ( $E/V_{C.b.} = 1.84$ ). The solid red line describes our best fit optical model calculation, while the blue dashed lines represent the results of the sensitivity analysis.

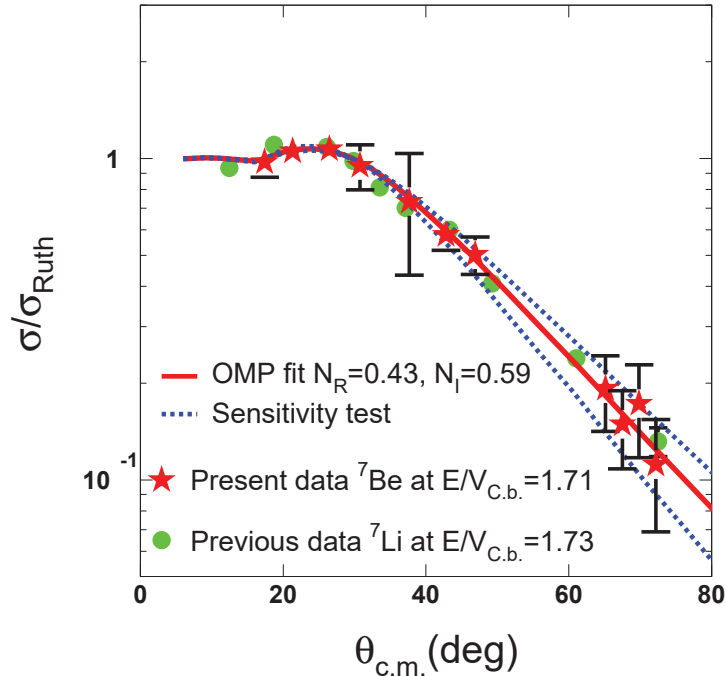


Figure 4.2: Present angular distribution data for the elastic scattering of  ${}^7\text{Be} + {}^{28}\text{Si}$  at the energy of 19.8 MeV ( $E/V_{C.b.} = 1.71$ ), designated with the red stars, are compared with previous data [17] for  ${}^7\text{Li} + {}^{28}\text{Si}$  at 15.0 MeV ( $E/V_{C.b.} = 1.73$ ). The solid red line describes our best fit optical model calculation, while the blue dashed lines represent the results of the sensitivity analysis.

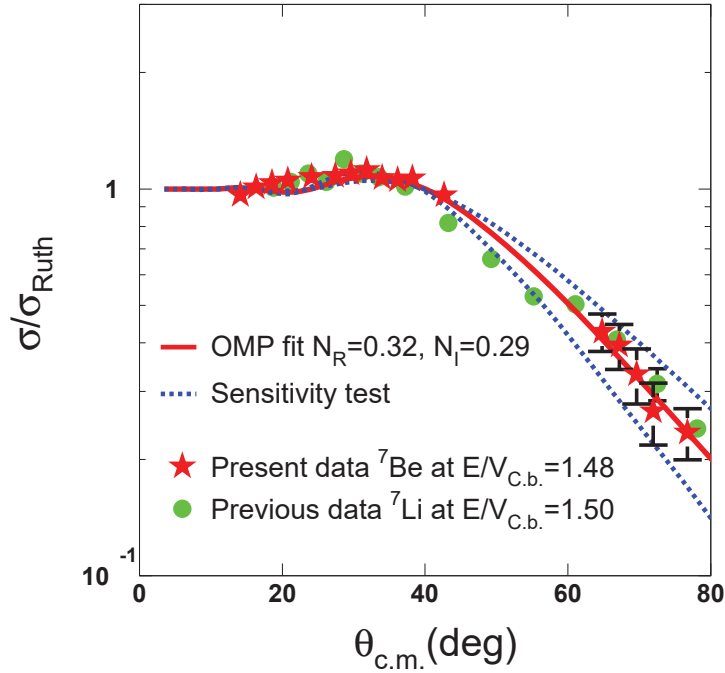


Figure 4.3: Present angular distribution data for the elastic scattering of  ${}^7\text{Be} + {}^{28}\text{Si}$  at the energy of 17.2 MeV ( $E/V_{C.b.} = 1.48$ ), designated with the red stars, are compared with previous data [17] for  ${}^7\text{Li} + {}^{28}\text{Si}$  at 13.0 MeV ( $E/V_{C.b.} = 1.50$ ). The solid red line describes our best fit optical model calculation, while the blue dashed lines represent the results of the sensitivity analysis.

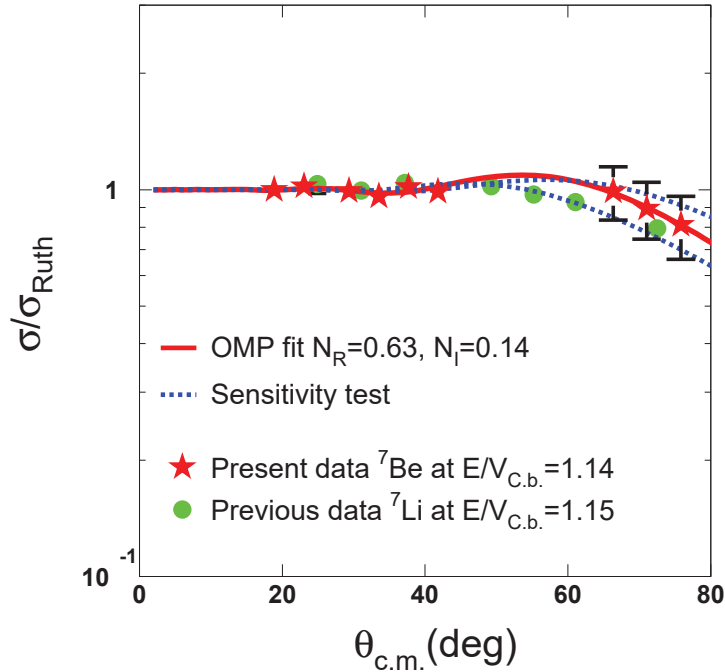


Figure 4.4: Present angular distribution data for the elastic scattering of  ${}^7\text{Be} + {}^{28}\text{Si}$  at the energy of 13.2 MeV ( $E/V_{C.b.} = 1.14$ ), designated with the red stars, are compared with previous data [17] for  ${}^7\text{Li} + {}^{28}\text{Si}$  at 10.0 MeV ( $E/V_{C.b.} = 1.15$ ). The solid red line describes our best fit optical model calculation, while the blue dashed lines represent the results of the sensitivity analysis.

### 4.1.2 Energy evolution of the optical potential parameters

The best fit optical potential parameters for the system  ${}^7\text{Be} + {}^{28}\text{Si}$  are plotted in Figure 4.5 as a function of energy. It has to be pointed out here that we have considered as more appropriate to plot rather these potential parameters [16] as a function of energy, than the values of the real and imaginary potential at the strong absorption radius, since for light elements the definition of the radial region of sensitivity is not straight forward. As it was shown by Roubos et al. [77], using the crossing point method to determine the sensitive radius, two crossing points between the various potential families were observed around Coulomb barrier. Furthermore, for weakly bound projectiles, the radial region of sensitivity varies with the bombarding energy [165,166]. Additionally, in a similar analysis for  ${}^6\text{Li} + {}^{28}\text{Si}$  system [16], tests adopting either a Woods-Saxon potential [101] for the imaginary part or the same folding interaction as for the real part were performed. In both cases, the quality of the fits to the angular distribution data was similar. This result validates the present analysis. The present analysis is also preferable as we have to fit only two parameters, avoiding additional uncertainties for deducing the optical potential.

The energy evolution of the optical potential parameters is compared with previous results of  ${}^7\text{Li}$  on  ${}^{28}\text{Si}$  [17] in Figure 4.5. Although the uncertainties in the determination of the potential parameters for the  ${}^7\text{Be} + {}^{28}\text{Si}$  system are large, the trend of the energy evolution seems to be the same for both projectiles pointing out to a similarity between the two mirror nuclei. In particular, a decreasing trend in the strength of the imaginary potential is observed for both projectiles approaching the barrier from higher to lower energies compatible with the standard threshold anomaly. The situation is more clear considering the results of the analysis of the  ${}^6\text{Li} + {}^{28}\text{Si}$  data [16] with the backscattering barrier distribution technique [18–20,167]. As it was shown in Ref. [18,19], among different trials, only a potential with a slightly increasing imaginary part is able to describe adequately well both the excitation functions as well the barrier distribution data. The best potential obtained from the barrier distribution analysis for  ${}^6\text{Li} + {}^{28}\text{Si}$  system is presented in Figure 4.6, where an increasing trend is met at  $E \sim 1.7V_{C.b.}$ . This is a clear evidence that the imaginary part of the optical potential for  ${}^7\text{Be}$  presents the same decreasing trend with the decreasing energy as for  ${}^7\text{Li}$  and not  ${}^6\text{Li}$ . This behavior is in accordance with the re-analysis of the  ${}^7\text{Be} + {}^{58}\text{Ni}$  elastic scattering and fusion data [38], while it contradicts the findings from the analysis of the  ${}^7\text{Be} + {}^{27}\text{Al}$  [39] elastic scattering, where an energy independent imaginary potential is suggested. However, this independence is given as susceptible to the use of very thick targets. Our suggestion for the similarity between  ${}^7\text{Li}$  and  ${}^7\text{Be}$  is also supported by the analysis of our  $\alpha$  - production data, simultaneously measured

with the elastic scattering ones to be described in Section 4.2.

In case of the real potential, an attempt was made to describe the potential behavior in terms of dispersion relations. Using the linear segment model [5] for the imaginary potential, a dispersion relations calculation was performed for the  ${}^7\text{Be} + {}^{28}\text{Si}$  system and is presented in Figure 4.5. In the same figure, a dispersion relations calculation performed previously for the  ${}^7\text{Li}$  [17] is also compared with the data. It will be interesting here to include the results from a barrier distribution analysis performed previously for  ${}^7\text{Li} + {}^{28}\text{Si}$  system [19]. It was found that the real potential is not connected via dispersions relation with the imaginary part but instead, an energy independent potential is suggested. In our case the results are inconclusive since we possess only one datum at the region where the peak in the strength of the real part, associated with the drop of the imaginary potential, should appear without excluding an energy independent real potential as in the case of  ${}^7\text{Li}$ . In this direction, more measurements with lower uncertainties around the barrier region are needed to draw firm conclusions.

### 4.1.3 Total reaction cross sections

The optical model analysis for the system  ${}^7\text{Be} + {}^{28}\text{Si}$ , leads also to total reaction cross sections which are included in Table 4.2. The assigned errors were obtained from the sensitivity analysis performed for the normalization factors  $N_R$  and  $N_I$ . In the same Table we have included total reaction cross sections obtained from the analysis of the  $\alpha$ -particle production for the same system (see Section 4.2), total reaction cross sections obtained with the phenomenological prediction as deduced for light targets in Ref. [68] and also total reaction cross sections calculated in a CDCC approach (see subsection 4.1.4). All results are found in very good agreement, supporting our present optical model analysis. Further on, our results were considered in a systematic framework involving other weakly bound and radioactive projectiles on a similar,  ${}^{27}\text{Al}$ , or the same target,  ${}^{28}\text{Si}$ . However, in order to compare total reaction cross sections corresponding to different systems, it is necessary to reduce appropriately the cross sections and compare them to some benchmark as it was pointed out in [168]. Thus, the different data sets were reduced according to a procedure applied previously for the reduction of fusion cross sections to fusion functions, as it is presented in Refs. [169–172]. Details about this procedure are given in Section 4.2. This technique is now applied to total reaction cross sections,  $(\sigma_{TR})$ , where they are reduced to total reaction cross section functions,  $\mathbf{F}_{TR}$ , as a function of quantity  $\mathbf{x}$ , following the prescription described in Refs. [68, 172, 173]. The definitions of  $F_{TR}$  and  $\mathbf{x}$  are the following:

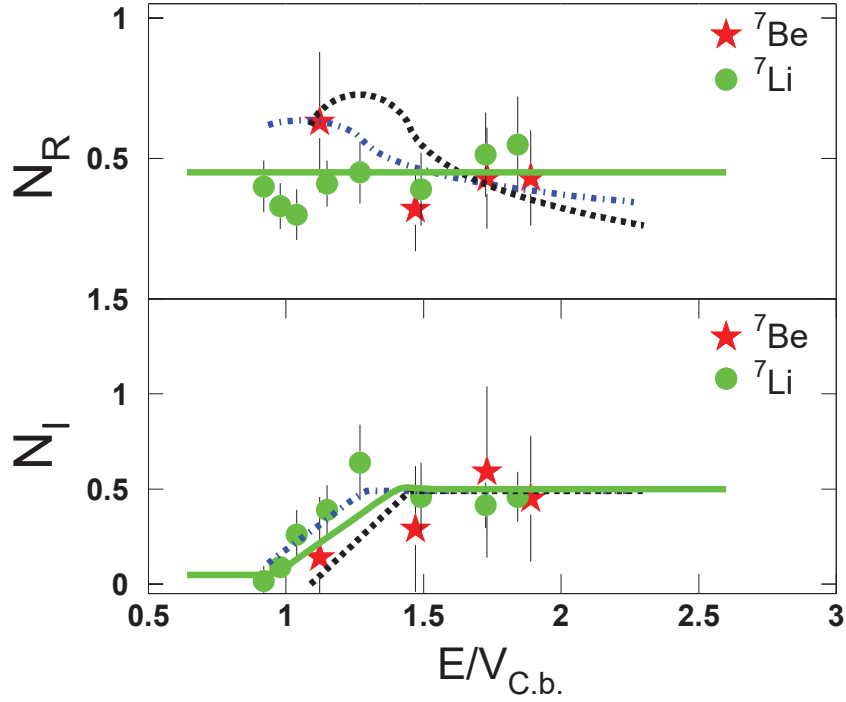


Figure 4.5: The energy evolution of the optical potential parameters,  $N_R$  and  $N_I$ , obtained in a BDM3Y1 framework for the  ${}^7\text{Be} + {}^{28}\text{Si}$  - present data, designated with the red stars, are compared with optical potential parameters for the system  ${}^7\text{Li} + {}^{28}\text{Si}$  - previous data [17], designated with the green circles. The dotted-dashed blue line corresponds to a dispersion relation analysis performed previously for  ${}^7\text{Li}$  [17], while the dashed black line corresponds to a dispersion relation analysis performed for the  ${}^7\text{Be}$  using the routine from Ref. [167]. The solid green lines correspond to the results of a barrier distribution analysis for  ${}^7\text{Li}$  [19], where an energy independent real potential is suggested, without obeying dispersion relations.

$$\sigma_{TR} \rightarrow F_{TR}(x) = \frac{2E_{c.m.}}{\hbar\omega R_B^2} * \sigma_{TR} \quad (4.1)$$

corresponding to an energy in the center of mass,  $\mathbf{E}_{c.m.}$ , reduced to quantity  $x$  given by the expression:

$$E_{c.m.} \rightarrow x = \frac{E_{c.m.} - V_B}{\hbar\omega}. \quad (4.2)$$

The barrier parameters namely, barrier heights  $V_B$ , radii  $R_B$  and curvatures  $\hbar\omega$  for the different systems were obtained using the Christensen-Winther potential [174] and are included in Table 4.3. Since the  $F_{TR}$  functions are strongly dependent on the atomic and mass number of the colliding ions [172], the comparison of reduced total reaction cross sections was limited

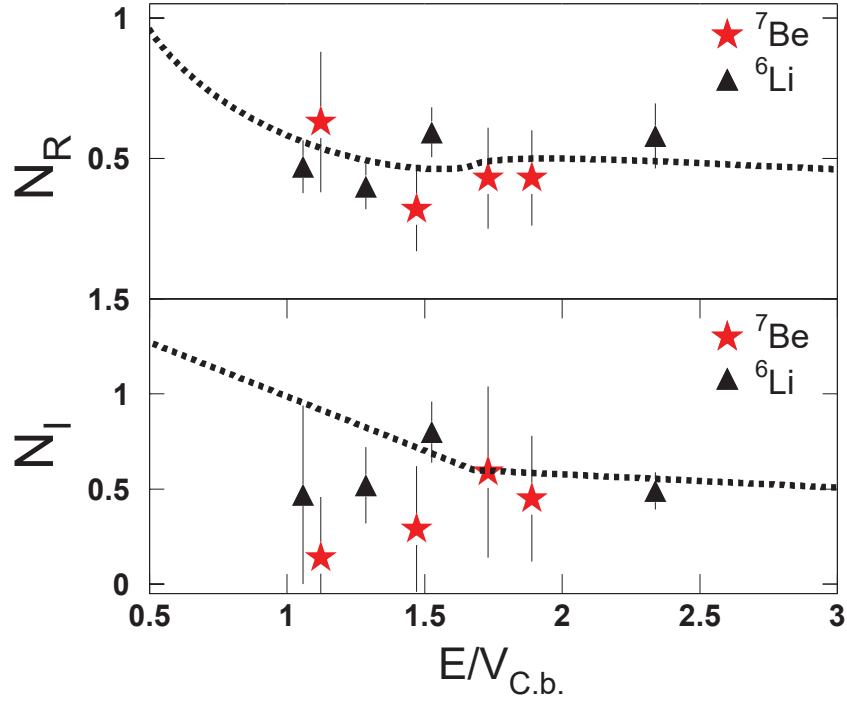


Figure 4.6: *The energy evolution of the optical potential parameters,  $N_R$  and  $N_I$ , obtained in a BDM3Y1 framework for the  ${}^7\text{Be} + {}^{28}\text{Si}$  - present data, designated with the red stars, are compared with optical potential parameters for the system  ${}^6\text{Li} + {}^{28}\text{Si}$  - previous data [16], designated with the black triangles. The dashed black line corresponds to a barrier distribution analysis performed previously for  ${}^6\text{Li}$  [18].*

to light targets. As it may be seen in Figure 4.7, the present results are in very good agreement with previous data:  ${}^{6,7}\text{Li} + {}^{28}\text{Si}$  [78],  ${}^6\text{He} + {}^{27}\text{Al}$  [175],  ${}^6\text{Li} + {}^{27}\text{Al}$  [176],  ${}^7\text{Be} + {}^{27}\text{Al}$  [39, 177] and  ${}^8\text{B} + {}^{27}\text{Al}$  [178]. Looking at Figure 4.7, we may see that the values of the total reactions cross sections corresponding to the first set of  ${}^7\text{Be} + {}^{27}\text{Al}$  [39] are larger than the second set [177], the present and all other data. This fact is related with the experimental conditions under these measurements were performed. By using such thick  ${}^{27}\text{Al}$  targets,  $2.1 \text{ mg/cm}^2$  and  $5.0 \text{ mg/cm}^2$ , large uncertainties in the determination of the reaction energy are introduced and therefore, the results of the optical model analysis, including total reaction cross sections, may be invalid. Also, for  ${}^8\text{B}$  the authors give two experimental values for the total reaction cross section (designated in Figure 4.7 with the magenta open circles and black open triangles) extracted from their optical model analysis either with the São Paulo potential or with a Woods-Saxon one. Finally, all data sets are compared with a phenomenological prediction obtained in Ref. [68], which describes them in an excellent way, considering that the prediction formula is suggested within an uncertainty band of 20%. The prediction function is following

Table 4.2: Total reaction cross sections for  ${}^7\text{Be} + {}^{28}\text{Si}$  obtained in the present work via an optical model analysis,  $\sigma_{opt}$ , are compared with values deduced in the  $\alpha$ -production analysis [160] (see Section 4.2),  $\sigma_{\alpha\text{-production}}$ , as well as with a phenomenological prediction [68],  $\sigma_{pred}$  and a theoretical value extracted from our CDCC calculations,  $\sigma_{CDCC}$  (see Subsection 4.1.4). The first column includes projectile energies incident in front of the target,  $E_{lab}$ , while the second column, the reaction energy,  $E_{rea}$ , in the middle of the target.

| $E_{lab}$ (MeV) | $E_{rea}$ (MeV) | $\sigma_{opt}$ (mb) | $\sigma_{\alpha\text{-production}}$ (mb) | $\sigma_{pred}$ (mb) | $\sigma_{CDCC}$ (mb) |
|-----------------|-----------------|---------------------|--|----------------------|----------------------|
| 22.0            | 21.7            | $1124 \pm 148$      | $1206 \pm 195$                           | 1118                 | 1130                 |
| 19.8            | 19.5            | $1072 \pm 163$      | $1103 \pm 242$                           | 990                  | 1020                 |
| 17.2            | 16.7            | $738 \pm 190$       | -  | 779                  | 831                  |
| 13.2            | 12.9            | $355 \pm 95$        | $250 \pm 63$                             | 347                  | 401                  |

Table 4.3: The barrier parameters namely, barrier height  $V_B$ , radius  $R_B$  and curvature  $\hbar\omega$ , for various systems considered in this work, obtained using the Christensen-Winther potential [174].

| System                             | $V_B$ (MeV) | $R_B$ (fm) | $\hbar\omega$ (MeV) |
|------------------------------------|-------------|------------|---------------------|
| ${}^7\text{Be} + {}^{28}\text{Si}$ | 9.351       | 7.922      | 3.478               |
| ${}^6\text{Li} + {}^{28}\text{Si}$ | 7.008       | 7.932      | 3.223               |
| ${}^7\text{Li} + {}^{28}\text{Si}$ | 6.840       | 8.145      | 2.968               |
| ${}^8\text{B} + {}^{28}\text{Si}$  | 11.670      | 7.935      | 3.662               |
| ${}^7\text{Be} + {}^{27}\text{Al}$ | 8.681       | 7.925      | 3.371               |
| ${}^9\text{Be} + {}^{27}\text{Al}$ | 8.358       | 8.269      | 2.955               |
| ${}^6\text{Li} + {}^{27}\text{Al}$ | 6.512       | 7.927      | 3.123               |
| ${}^6\text{He} + {}^{27}\text{Al}$ | 4.201       | 8.222      | 2.487               |
| ${}^8\text{B} + {}^{27}\text{Al}$  | 10.825      | 7.943      | 3.553               |

the equation:  $Y(x) = \alpha \ln[1 + \exp(2\pi x - b)]$ , with  $\alpha = 1.14409$  and  $b = -1.06089$ .

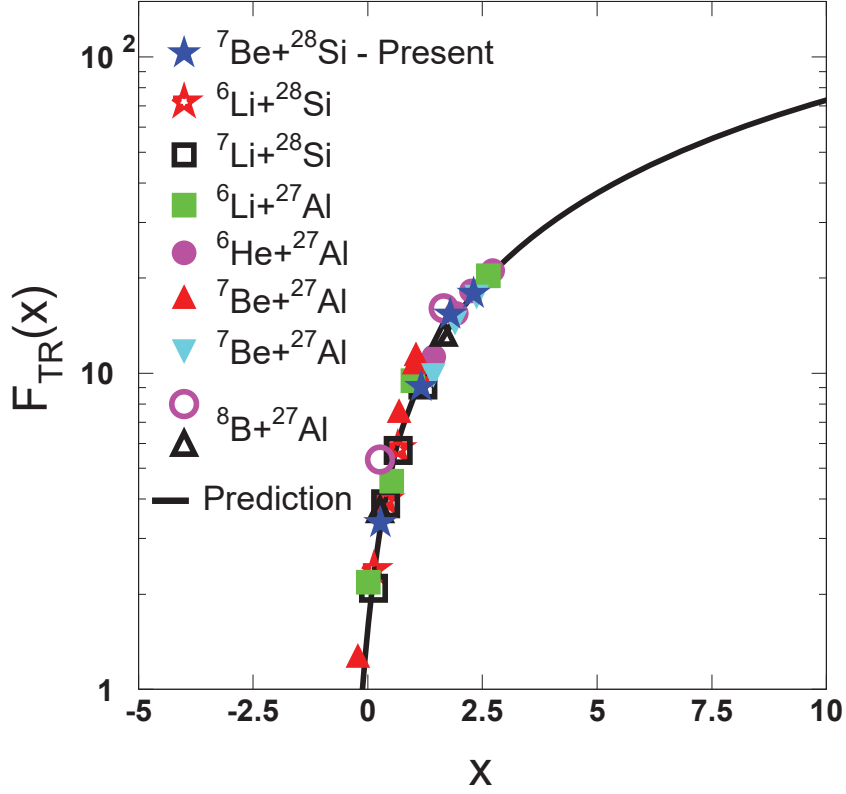


Figure 4.7: *Reduced total reaction cross sections for weakly bound projectiles on light targets. Previous data from Refs. [39, 78, 175–178] are compared with the present data and a prediction from Ref. [68] for light targets, designated with the black solid line.*

#### 4.1.4 Continuum Discretized Coupled Channels Calculations

For a more global description of the elastic scattering of  ${}^7\text{Be} + {}^{28}\text{Si}$ , Continuum Discretized Coupled Channels (CDCC) calculations were performed, taking into account couplings to continuum states, both resonant and non-resonant ones. These calculations were performed via the code FRESKO [98]. The model used in the calculations was very close to that of Ref. [179]. The  ${}^7\text{Be}$  nucleus was modeled as a composite system with a two-body  ${}^4\text{He} + {}^3\text{He}$  cluster structure. Couplings between resonant and non-resonant cluster states corresponding to  ${}^4\text{He} - {}^3\text{He}$  relative orbital angular momentum  $L = 0, 1, 2, 3, 4$  were included. The excitation to first excited state of the projectile (0.429 MeV) and ground state reorientation was also taken into account. The continuum phase space above the  ${}^7\text{Be} \rightarrow {}^4\text{He} + {}^3\text{He}$  breakup threshold (1.586 MeV) was discretized into momentum bins. As highest excitation energy was taken the

Table 4.4: *Optical model parameters for the  ${}^4\text{He} + {}^{28}\text{Si}$  [180] and  ${}^3\text{He} + {}^{28}\text{Si}$  [181] interactions adopted in the CDCC calculations. The real and imaginary parts of the optical potential are described by Woods-Saxon form factors. The nuclear radius is given as  $R = r_{V(W)} * 28^{1/3}$ . The Coulomb radius for the  ${}^4\text{He}({}^3\text{He}) + {}^{28}\text{Si}$  interaction was taken as  $R_C = 1.62(1.30) * 28^{1/3}$ .*

| System                             | V (MeV) | $r_V$ (fm) | $a_V$ (fm) | W (MeV) | $r_W$ (fm) | $a_W$ (fm) |
|------------------------------------|---------|------------|------------|---------|------------|------------|
| ${}^4\text{He} + {}^{28}\text{Si}$ | 82.00   | 1.62       | 0.52       | 13.50   | 1.62       | 0.52       |
| ${}^3\text{He} + {}^{28}\text{Si}$ | 106.50  | 1.07       | 0.85       | 11.80   | 1.80       | 0.65       |

energy of 9.4 MeV for the 22.0 and 19.8 MeV data and 7.7 MeV for the 17.2 and 13.2 MeV data. The convergence of the calculation was tested taking into account higher excitation energies and relative angular momenta which however did not affect the results of the calculation. The width of the bins at the energy of 13.2 and 17.2 MeV was  $\Delta k = 0.23 \text{ fm}^{-1}$ , while the width of the bins at the energy of 19.8 and 22.0 MeV was  $\Delta k = 0.20 \text{ fm}^{-1}$ . In the presence of resonant states, the binning schemes were suitably modified in order to avoid double counting. In our calculations, the  $7/2^-$  (4.57 MeV) and  $5/2^-$  (6.73 MeV) resonances were taken into account and they were treated as momentum bins with a width corresponding to 0.4 and 2.0 MeV respectively. All the diagonal and coupling potentials were generated from empirical  ${}^4\text{He} + \text{Target}$ ,  ${}^3\text{He} + \text{Target}$  optical model potentials for the corresponding target nucleus by means of the single-folding technique. The corresponding potentials were adopted from Refs. [180, 181] and are shown in Table 4.4.

Into this context, elastic scattering angular distributions were deduced and are compared with the data in Figures 4.8, 4.9, 4.10 and 4.11. Furthermore, one ( ${}^7\text{Be}$  ground state reorientation only)- and two ( ${}^7\text{Be}$  ground state reorientation and excitation of the first excited state)-channel calculations were performed and the results are compared with the data in Figures 4.12 and 4.13. The agreement of the data with the full CDCC calculations is very good, while it is seen that the coupling to inelastic excitations of  ${}^7\text{Be}$  is unimportant and couplings to continuum are substantial but not very strong. Furthermore, our CDCC calculations provided breakup angular distributions (Subsection 4.2.2) and total breakup cross sections. The last are included in Table 4.5.

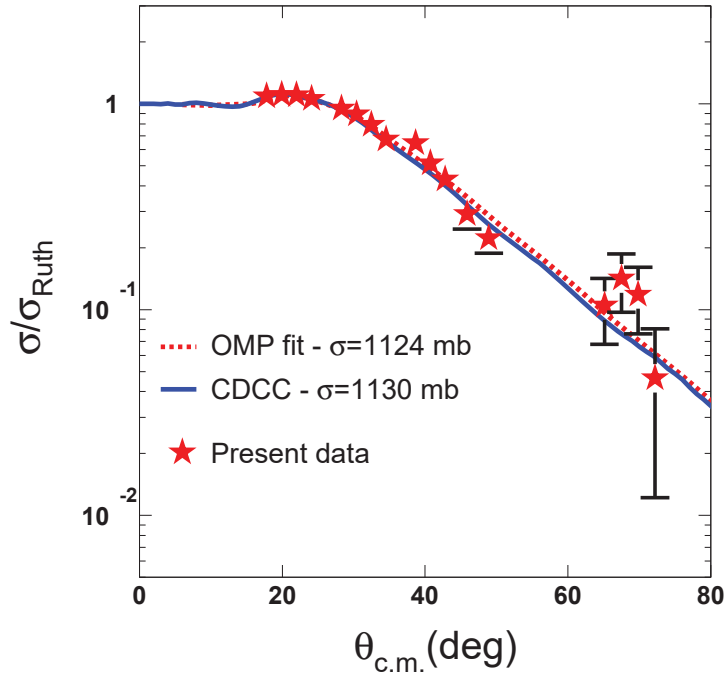


Figure 4.8: Present angular distribution data for the elastic scattering of  ${}^7\text{Be} + {}^{28}\text{Si}$  at the energy of 22.0 MeV ( $E/V_{C.b.} = 1.90$ ), designated with the red stars, are compared with a CDCC calculation which is denoted solid blue line. The dashed red line represents our best fit optical model calculation.

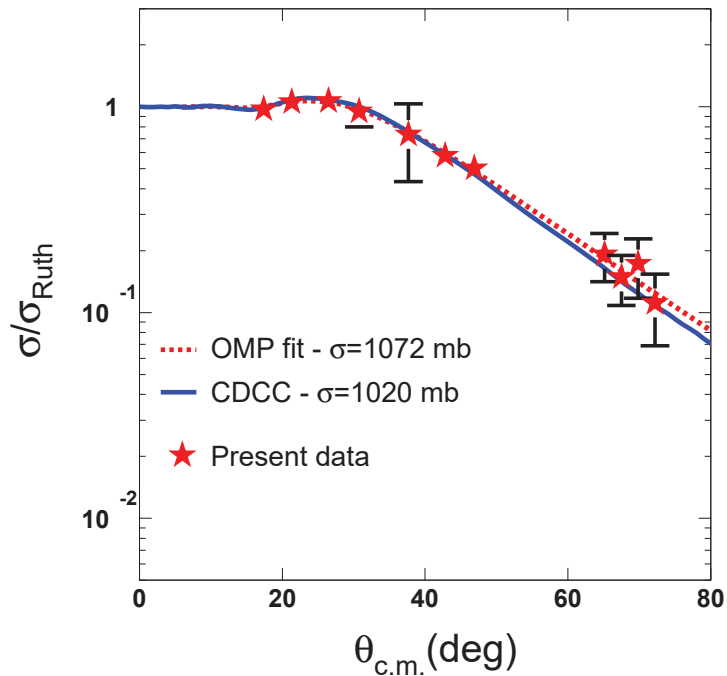


Figure 4.9: Same as in Figure 4.8 but for the energy of 19.8 MeV ( $E/V_{C.b.} = 1.71$ ).

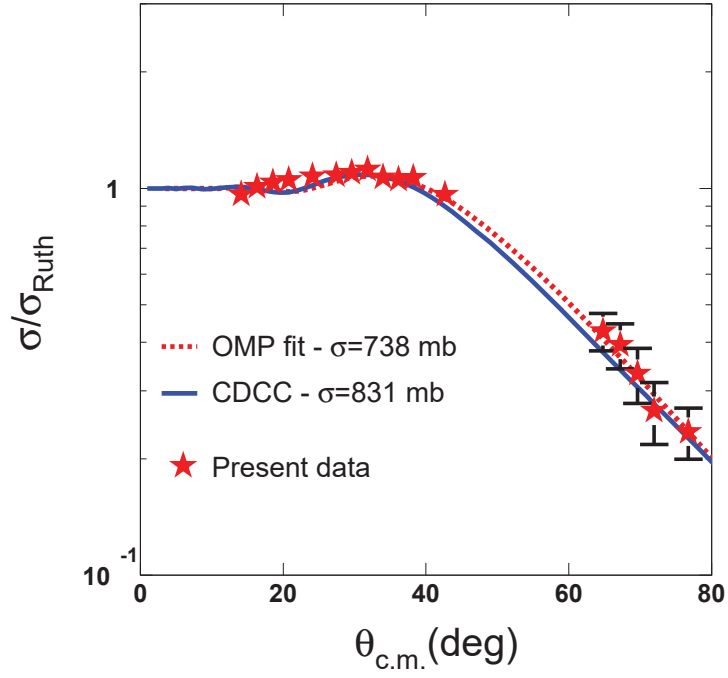


Figure 4.10: Same as in Figure 4.8 but for the energy of 17.2 MeV ( $E/V_{C.b.} = 1.48$ ).

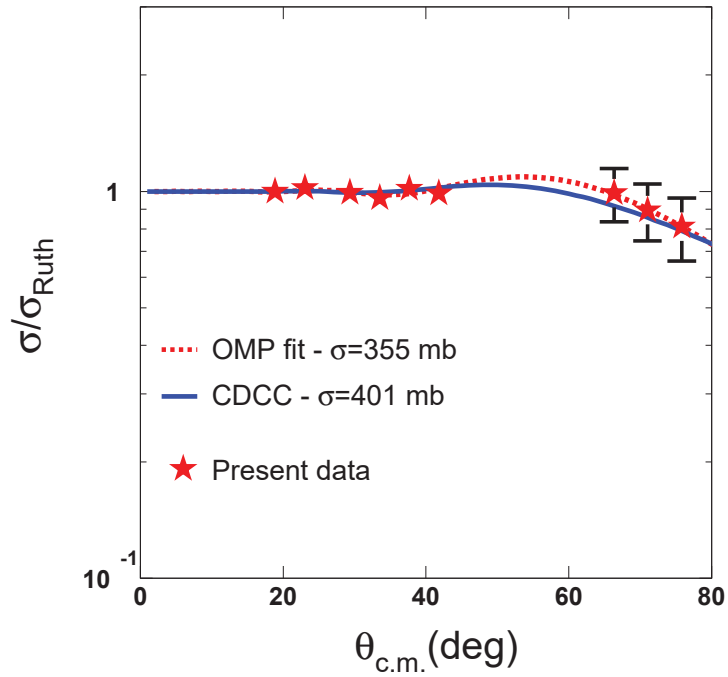


Figure 4.11: Same as in Figure 4.8 but for the energy of 13.2 MeV ( $E/V_{C.b.} = 1.14$ ).

Table 4.5: Breakup cross sections for the  ${}^7\text{Be} + {}^{28}\text{Si}$  system, as they were deduced from our CDCC calculations.

| Energy (MeV) | Breakup (mb) |
|--------------|--------------|
| 22.0         | 13.4         |
| 19.8         | 10.5         |
| 17.2         | 7.4          |
| 13.2         | 3.4          |

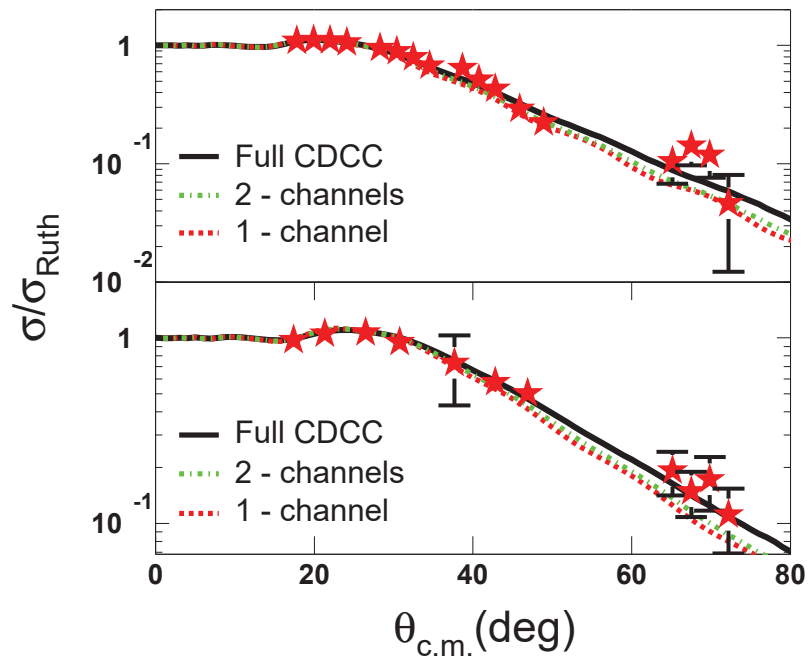


Figure 4.12: Elastic scattering data for  ${}^7\text{Be} + {}^{28}\text{Si}$  at 22.0 MeV (top) and 19.8 MeV (bottom) are compared with 1 - channel, 2 - channel and full CDCC calculations.

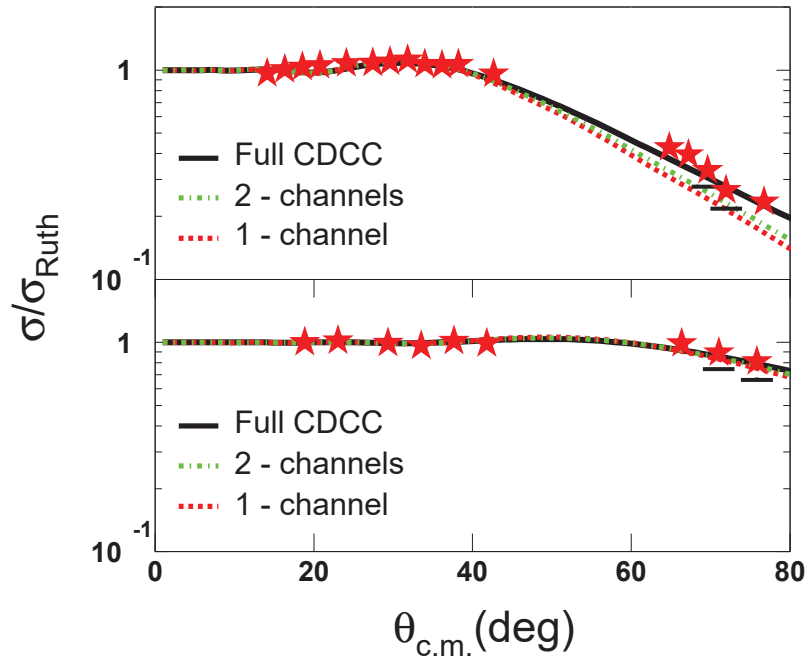


Figure 4.13: *Elastic scattering data for  ${}^7\text{Be} + {}^{28}\text{Si}$  at 17.2 MeV (top) and 13.2 MeV (bottom) are compared with 1 - channel, 2 - channel and full CDCC calculations.*

## 4.2 Reaction Mechanisms

### 4.2.1 Fusion Cross Sections

As it was mentioned in Chapter 3, the  $\alpha$ -particle production angular distributions are forward peaked but they also extend to more backward angles with substantial cross sections. This fact indicates the presence of both direct and compound nucleus formation mechanisms. In order to disentangle the compound nucleus processes from the direct ones, we follow the same technique as applied previously for the  ${}^6,7\text{Li} + {}^{28}\text{Si}$  systems [54, 60, 78]. The angular distributions from evaporated  $\alpha$ -particles were calculated within the statistical model framework [182] via code PACE2 (**P**rojection **A**ngular-momentum **C**oupled **E**vaporation) [132]. In the code, optical potential parameters for the evaporation of  $\alpha$ -particles were introduced from the work of Huizenga and Igo [183] based on  $\alpha$ -particle scattering from very low energies up to 50 MeV, and 20 target nuclei with  $10 \leq Z \leq 92$ . The level density parameter was taken as  $A/8 \text{ MeV}^{-1}$ , and compound nucleus spin distributions were calculated taking into account the Bass nuclear potential [184].

The calculated angular distributions were renormalized to the data of the backward de-

tectors,  $T_3$  and  $T_4$ . The procedure is illustrated in Figure 4.14 for 22.0, 19.8 and 13.2 MeV. In the latter case, due to low statistics, data for the middle and backward detectors were summed over the whole detector and the obtained differential cross sections were assigned to the middle angle of each detector. The renormalized compound nucleus angular distributions were integrated over angle and the  $\alpha$ -particle production due to compound nucleus formation,  $\sigma_{compound}^\alpha$ , was obtained. The values are included in Table 4.7. The errors were assigned taking into account the best fits and a reduced  $\chi^2$ -plus-1 analysis  $[(\chi^2/N) + 1]$ . The statistical model code PACE2, provides also the multiplicities for the evaporated  $\alpha$ -particles. Therefore, it was possible to deduce fusion cross section at three near barrier energies. However, it should be noted that the determination of fusion cross sections may be liable to possible shortcomings of the statistical model code. A comprehensive analysis of  $^8\text{B}$  fusion data in various compound nucleus models [185], has pointed out this issue. Our case is slightly different, since the parameter introduced in the evaporation code, that is the total fusion cross section, does not affect the extracted values of fusion cross sections as the calculated angular distributions are renormalized to the backward angle experimental data. However, the  $\alpha$ -particle multiplicities are sensitive on the choice of the level density parameter and the optical potential parameters for the evaporation of  $\alpha$ 's. This may introduce uncertainties in the determination of fusion cross sections.

In this direction, test adopting different level densities or different optical potential parameters were carried out. By varying the level densities approximately  $\pm 6\%$  ( $A/7.5$  or  $A/8.5$ ), the calculated multiplicities are larger or smaller 1% to 2%, introducing a negligible error to the fusion. Thus, we have estimated the error introduced in the multiplicities by using three different sets of optical model parameters from the work of Huizenga and Igo [183], McFadden and Satchler [186] and Satchler [187]. The last two are based on the analysis of 24.7 and 28.0 MeV  $\alpha$ -particle scattering on various targets with atomic numbers,  $8 \leq Z \leq 92$  and  $10 \leq Z \leq 50$  respectively. The calculated multiplicities together with the mean and a standard deviation are presented in Table 4.6. Subsequently, using the  $\alpha$ -particle multiplicities and the cross sections due to compound nucleus formation, fusion cross sections were deduced. The values are included in Table 4.7 and they are also compared with a single barrier penetration model (BPM) prediction of Wong [74].

The fusion cross sections, presented in Table 4.7, were considered in a systematics involving other, stable, weakly bound and radioactive projectiles on the same or similar mass targets ( $^{27}\text{Al}$ ,  $^{28}\text{Si}$ ). However, in order to compare fusion cross sections corresponding to various systems, the different data sets should be reduced appropriately such as to exclude static

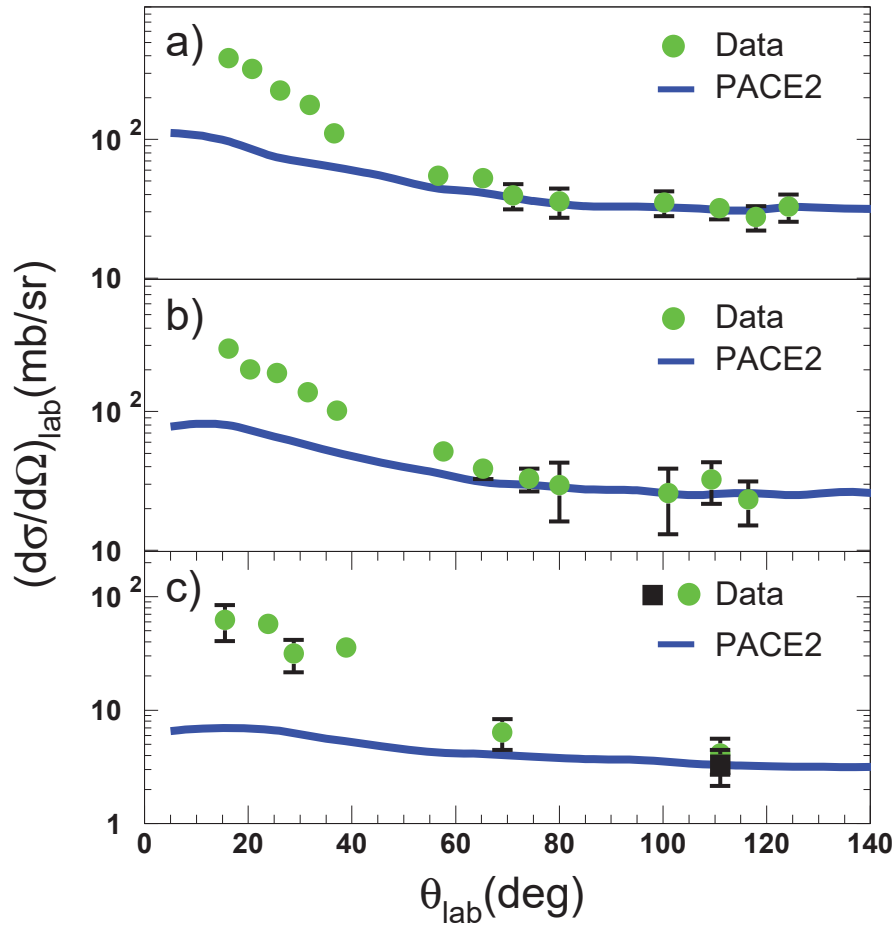


Figure 4.14: Present angular distribution data for the  ${}^4\text{He}$  particle production at the energies of a) 22.0 MeV, b) 19.8 MeV and c) 13.2 MeV. The solid blue line represents a calculation with the evaporation code PACE2 renormalized to the backward angle data. For the energy of 13.2 MeV, the black square represents the experimental datum minus the estimated contribution from direct processes, since in that case we expect significant direct contribution.

Table 4.6:  $\alpha$ -particle multiplicities obtained via statistical code PACE2 [132] using three different sets of optical potentials. The second column includes multiplicities using the Huizenga and Igo potential [183], M1, the third column using the McFadden and Satchler potential [186], M2, the fourth column using the Satchler potential [187], M3, while the last column includes the mean of these multiplicities,  $M_{mean}$ , and the standard deviation.

| Energy (MeV) | M1   | M2   | M3   | $M_{mean}$      |
|--------------|------|------|------|-----------------|
| 22.0         | 0.63 | 0.55 | 0.58 | $0.59 \pm 0.04$ |
| 19.8         | 0.57 | 0.50 | 0.52 | $0.53 \pm 0.04$ |
| 13.2         | 0.37 | 0.31 | 0.34 | $0.34 \pm 0.03$ |

effects for each system arising from the different barrier heights, radii and curvatures. The reduction procedure adopted in this work follows the prescription described in Refs. [169–172], based on a single barrier penetration model of Wong. Wong has approximated the barriers for different partial waves,  $\ell$ , by inverted harmonic oscillator potentials of height  $V_{B\ell}$  and frequency  $\omega_\ell$ . By using the assumption that the radii and curvatures of the potentials do not vary with angular momentum, Wong obtained for fusion the following analytic expression:

$$\sigma_{fusion}^{Wong} = \frac{\hbar\omega R_B^2}{2E_{c.m.}} * \ln \left[ 1 + \exp \left( \frac{2\pi(E_{c.m.} - V_B)}{\hbar\omega} \right) \right]. \quad (4.3)$$

Into this context, fusion cross sections can be reduced to fusion functions,  $\mathbf{F}(\mathbf{x})$ , as a function of quantity  $\mathbf{x}$ , according to the following relations:

$$\sigma_{fusion} \rightarrow F(x) = \frac{2E_{c.m.}}{\hbar\omega R_B^2} * \sigma_{fusion} \quad (4.4)$$

and

$$E_{c.m.} \rightarrow x = \frac{E_{c.m.} - V_B}{\hbar\omega}. \quad (4.5)$$

Table 4.7: Details of our results for the compound nucleus channel. The second column includes the cross section for the  $\alpha$ -particle production due to compound nucleus formation. The third column includes the  $\alpha$ -particle multiplicities obtained via the statistical code PACE2. The fourth column includes the extracted fusion cross sections,  $\sigma_{fusion}$ , and the last column a prediction for fusion cross section according to a single barrier penetration model of Wong [74].

| Energy (MeV) | $\sigma_{compound}^{\alpha}$ (mb) | $\alpha$ multiplicity | $\sigma_{fusion}$ (mb) | $\sigma_{fusion}^{Wong}$ (mb) |
|--------------|-----------------------------------|-----------------------|------------------------|-------------------------------|
| 22.0         | $511 \pm 87$                      | $0.59 \pm 0.04$       | $866 \pm 159$          | 910                           |
| 19.8         | $419 \pm 105$                     | $0.53 \pm 0.04$       | $791 \pm 205$          | 791                           |
| 13.2         | $50 \pm 18$                       | $0.34 \pm 0.03$       | $147 \pm 54$           | 202                           |

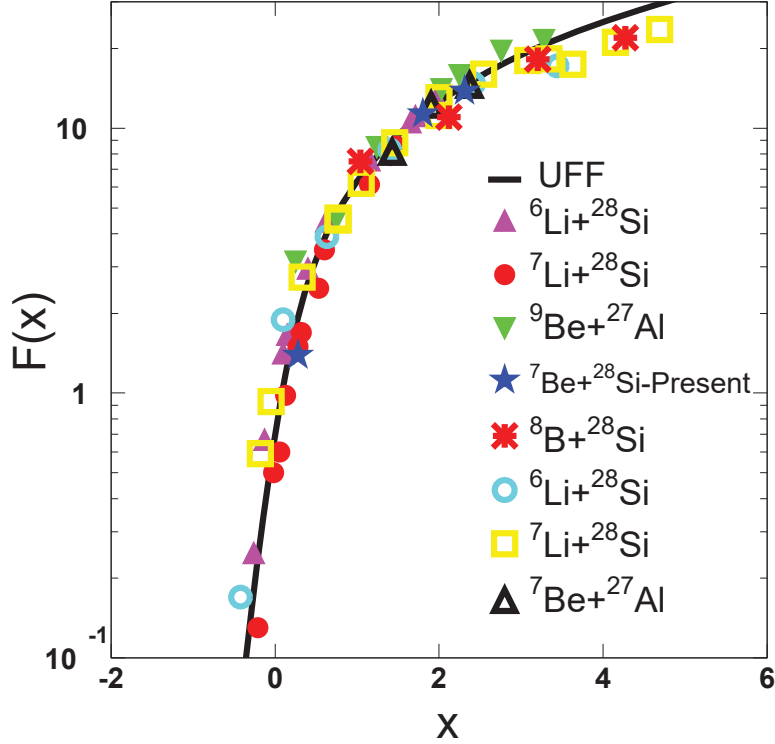


Figure 4.15: Reduced fusion cross sections for various stable and weakly bound (stable or radioactive) projectiles incident on  $^{27}\text{Al}$  and  $^{28}\text{Si}$  targets as a function of parameter  $x$  (reduced energy). The reduction was made according to Refs. [169–172]. The solid black line represents the Universal Fusion Function, UFF, defined in [171]. Previous data were taken from Refs. [78, 83, 177, 188–192].

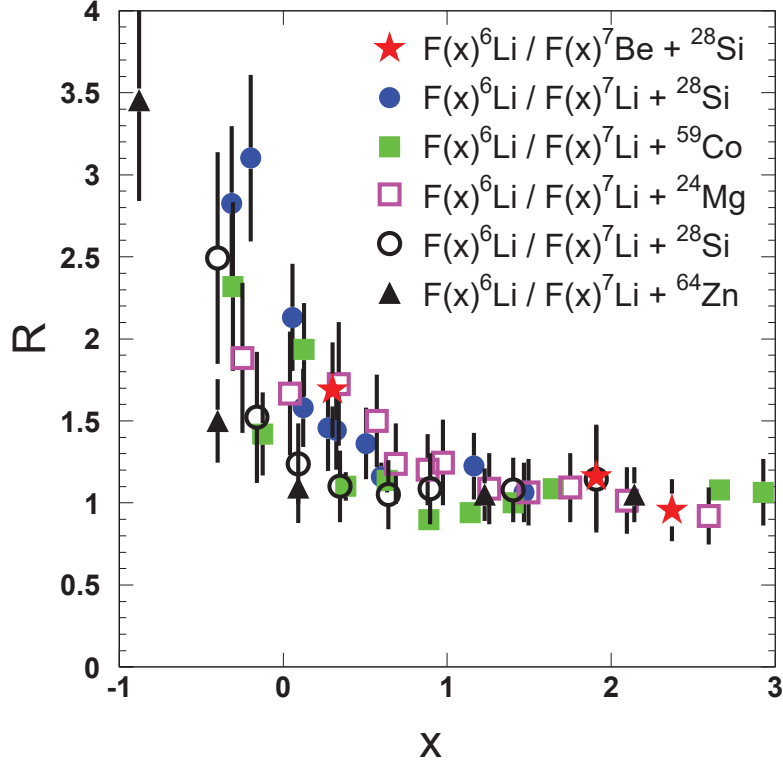


Figure 4.16: Ratios of fusion functions for  ${}^6\text{Li} + {}^{28}\text{Si}$  versus  ${}^7\text{Li} + {}^{28}\text{Si}$  compared with ratios of fusion functions for  ${}^6\text{Li} + {}^{28}\text{Si}$  versus  ${}^7\text{Be} + {}^{28}\text{Si}$  as a function of parameter  $x$  (reduced energy). Other ratios for  ${}^6\text{Li}$  versus  ${}^7\text{Li}$  on various low and medium mass targets are also included.

Fusion functions,  $F(x)$ , were determined for various systems and they are compared among themselves in Figure 4.15. The potential barrier parameters namely, barrier heights  $\mathbf{V}_B$ , radii  $\mathbf{R}_B$  and curvatures  $\hbar\omega$  for the different systems were obtained using the Christensen-Winther potential [174] and are included in Table 4.3. Looking in Figure 4.15, present and previous data follow the same trend as the **U**niversal **F**usion **F**unction (UFF), defined in Ref. [171] as:

$$F_0(x) = \ln \left[ 1 + \exp(2\pi x) \right], \quad (4.6)$$

and show good consistency between each other as well as the UFF to within an uncertainty band of 10% to 20%. Variations between the data and the UFF are expected since the experimental values for fusion, are given, in principle, at least with an error  $\sim 10\%$ . Also, Wong's approximation does not take into account couplings to direct mechanisms like breakup or transfer which are expected to be important around and below barrier. However, to assign

such variations with significance to a particular coupling scheme, the uncertainties to fusion cross sections should be small, which is not in the present case. Nevertheless, we may try to map variations between fusion cross sections obtained for  ${}^6\text{Li}$  and  ${}^7\text{Li}$  with those for  ${}^7\text{Be}$ , in order to strengthen (or not) our results obtained from the optical model analysis that point to a similarity between the two mirror nuclei,  ${}^7\text{Li}$  and  ${}^7\text{Be}$ . In this direction, ratios of fusion functions for  ${}^6\text{Li}$  to those for  ${}^7\text{Li}$  and  ${}^7\text{Be}$  were formed. Comparisons of previously measured data for  ${}^{6,7}\text{Li} + {}^{24}\text{Mg}$  [82],  ${}^{6,7}\text{Li} + {}^{28}\text{Si}$  [78],  ${}^{6,7}\text{Li} + {}^{28}\text{Si}$  [83],  ${}^{6,7}\text{Li} + {}^{59}\text{Co}$  [80] and  ${}^{6,7}\text{Li} + {}^{64}\text{Zn}$  [81] with present results are shown in Figure 4.16. It is seen that hindrance of fusion cross sections for  ${}^7\text{Li}$  with respect to those of  ${}^6\text{Li}$ , starts near barrier (already at  $\sim E = 1.1V_{C.b.}$ ,  $R = 1.5$ ) and it reaches the order of  $\sim 70\%$  well below barrier. The same trend is met for the present data indicating a similarity between  ${}^7\text{Be}$  and  ${}^7\text{Li}$  rather than  ${}^6\text{Li}$  as theory had predicted for elastic scattering in Ref. [179]. However, it should be noted that in Ref. [179], CDCC calculations were performed for the elastic scattering of  ${}^{6,7}\text{Li}$  and  ${}^7\text{Be}$  on the heavy  ${}^{208}\text{Pb}$  target, where couplings to breakup could play an important role.

## 4.2.2 Direct Reactions Cross Sections

In the previous Section, cross sections due to compound nucleus formation were determined by renormalizing the theoretical compound nucleus angular distributions to the backward angle data of the experimental (total)  $\alpha$ -particle angular distributions. By subtracting from the experimental (total) cross sections the renormalized compound values at each angle, the angular distributions due to direct mechanisms were obtained. As it was already mentioned in Chapter 3, different direct processes contribute to the  $\alpha$ -particle cross section. Theoretical angular distributions for the n-pickup and n-stripping processes were obtained in the DWBA framework, while for the breakup the  $\alpha$  angular distributions were obtained in a CDCC framework. The relevant transformations of the theoretical angular distributions from the center-of-mass frame to the laboratory one were performed using the same Monte Carlo code used in the spectrum simulations. The so obtained angular distributions are compared with the data in Figure 4.17. Looking at Figure 4.17, it can be seen that the  $\alpha$ -particle production due to these processes is small. The remaining part should be therefore attributed to an  ${}^3\text{He}$  stripping process, but which cannot be quantified by DWBA calculations due to the lack of the appropriate spectroscopic factors (see Subsection 4.2.3).

For the  ${}^3\text{He}$ -particle production, the only two contributing mechanisms are the  ${}^4\text{He}$  stripping and the breakup. However, due to the low statistics and the geometrical efficiency of our detector setup, coincidence events between  ${}^3\text{He}$  and  ${}^4\text{He}$  particles, a clear signature of an ex-

clusive breakup event, were not recorded. Therefore, integrating the  $^3\text{He}$  angular distributions, we can provide an inclusive cross section for both reaction channels. The results are given in Table 4.8. Moreover, theoretical angular distributions for the  $^4\text{He}$  stripping and breakup were obtained in the DWBA and CDCC frameworks respectively and are compared to the experimental data in Figure 4.18. The “total” angular distributions, obtained as the sum of the angular distributions for the breakup and  $^4\text{He}$  stripping, are in reasonable qualitative agreement with the experimental data, while underestimate them in absolute magnitudes. This may be explained from the fact that absolute spectroscopic factors for  $\alpha$  transfer, introduced in the DWBA calculation for the  $^{28}\text{Si}(^7\text{Be}, ^3\text{He})^{32}\text{S}$  reaction, are notoriously ill defined. The values of the spectroscopic factors extracted from experiments with the same target but using different reactions and at different energies, may vary by a factor of 5 or more. Therefore, taking into account that according to CDCC calculations, which described in a very good way the elastic scattering data, the contribution of the breakup channel is small, we can say that the bulk of the  $^3\text{He}$  production is attributed to  $^4\text{He}$  stripping. This is consistent with previous data concerning the  $^7\text{Be}+^{58}\text{Ni}$  system [67] and it seems to be a more general property of reactions involving weakly bound nuclei presenting a cluster structure. For example, in Ref. [57], where exclusive measurements are reported for  $^7\text{Li}+^{93}\text{Nb}$ , t stripping is suggested as the main direct mechanism for the  $\alpha$  production.

Finally, having obtained cross sections for the  $^{3,4}\text{He}$  production due to direct mechanisms and fusion cross sections, total reaction cross sections were deduced by summing these two components. To avoid double summing the breakup channel, present in both  $^3\text{He}$  and  $^4\text{He}$ -particle production, we have subtracted the breakup cross section estimated via the CDCC calculations. Also, to avoid double counting of  $\alpha$ 's from the decay of  $^8\text{Be}$  (n-pickup reaction) which breaks into two  $\alpha$  particles, we have subtracted the cross section estimated via the DWBA calculations. Both these contributions are very small and do not significantly affect the final result. The values of the total reaction cross sections, extracted from the  $\alpha$  production measurement, are given in the sixth column of Table 4.8. Also, a comparison between these values and the ones obtained from the present optical model analysis, from our CDCC calculations and a prediction formula described in Ref. [68] is presented in Table 4.9. All values are in very good agreement with each other indicating the validity of the measurements. Subsequently, ratios of the direct versus total reaction cross sections were formed. The present ratios are compared with previous ones for the systems  $^{6,7}\text{Li} + ^{28}\text{Si}$  [68, 78] in Figure 4.19. The trend of the energy evolution of the ratio for the three projectiles is the same, that is approaching the barrier from higher to lower energies, the contribution of the direct channels becomes larger. However, the present data seem to follow in magnitude those of  $^7\text{Li}$  rather

Table 4.8:  ${}^4\text{He}$  and  ${}^3\text{He}$ - particle production cross sections. The second column includes the cross section for  ${}^4\text{He}$ -particle production. The third and fourth columns include the  ${}^4\text{He}$ - and  ${}^3\text{He}$ - particle production cross sections, respectively, due to direct mechanisms. The fifth column includes total cross sections due to the direct channels, deduced as the sum of  ${}^4\text{He}$  and  ${}^3\text{He}$  cross sections after subtracting a small part due to breakup and due to double  $\alpha$ -production in the  ${}^8\text{Be} + {}^{27}\text{Si}$  channel. The breakup cross sections were estimated in a CDCC approach resulting 13.4 mb, 10.5 mb and 3.4 mb for 22.0 MeV, 19.8 MeV and 13.2 MeV respectively. The transfer pickup was estimated in a DWBA calculation and the parts subtracted were 12.5 mb, 12.0 mb and 5.0 mb for 22.0 MeV, 19.8 MeV and 13.2 MeV respectively. Finally, the sixth column includes total reaction cross sections by summing fusion cross sections and direct cross sections (the fifth column of this table and the fourth column of Table 4.7).

| Energy (MeV) | $\sigma_{total}^\alpha$ (mb) | $\sigma_{direct}^\alpha$ (mb) | $\sigma_{direct}^{3\text{He}}$ (mb) | $\sigma_{direct}$ (mb) | $\sigma_{\alpha\text{-production}}$ (mb) |
|--------------|------------------------------|-------------------------------|-------------------------------------|------------------------|--|
| 22.0         | $763 \pm 69$                 | $252 \pm 111$                 | $114 \pm 17$                        | $340 \pm 112$          | $1206 \pm 195$                           |
| 19.8         | $653 \pm 72$                 | $234 \pm 127$                 | $101 \pm 19$                        | $312 \pm 128$          | $1103 \pm 242$                           |
| 13.2         | $131 \pm 26$                 | $81 \pm 32$                   | $30 \pm 8$                          | $103 \pm 33$           | $250 \pm 63$                             |

Table 4.9: Total reaction cross sections for  ${}^7\text{Be} + {}^{28}\text{Si}$  extracted from the  $\alpha$ -production analysis,  $\sigma_{\alpha\text{-production}}$ , are compared with values deduced in the present optical model analysis,  $\sigma_{opt}$ , as well as with the theoretical values extracted from our CDCC calculations,  $\sigma_{CDCC}$  and a phenomenological prediction [68],  $\sigma_{pred}$ . The first column includes projectile energies incident in front of the target and the second column breakup cross sections,  $\sigma_{bu}$ , deduced from our CDCC calculations.

| $E_{lab}$ (MeV) | $\sigma_{bu}$ (mb) | $\sigma_{\alpha\text{-production}}$ (mb) | $\sigma_{opt}$ (mb) | $\sigma_{CDCC}$ (mb) | $\sigma_{pred}$ (mb) |
|-----------------|--------------------|--|---------------------|----------------------|----------------------|
| 22.0            | 13.4               | $1206 \pm 195$                           | $1124 \pm 148$      | 1130                 | 1118                 |
| 19.8            | 10.5               | $1103 \pm 242$                           | $1072 \pm 163$      | 1020                 | 990                  |
| 17.2            | 7.4                | -  | $738 \pm 190$       | 831                  | 779                  |
| 13.2            | 3.4                | $250 \pm 63$                             | $355 \pm 95$        | 401                  | 347                  |

than those for  ${}^6\text{Li}$ . This indicates larger contribution of direct processes for the two mirror nuclei than for  ${}^6\text{Li}$ . Approaching the barrier from higher to lower energies, direct channels exhaust the largest part of the total reaction cross section (70% of the total reaction cross section) and this may be the reason for fusion hindrance, observed for  ${}^7\text{Li}$  and  ${}^7\text{Be}$  compared to  ${}^6\text{Li}$  (Figure 4.16). It should be underlined that more data for the  ${}^7\text{Be}$  below barrier are needed, in order to draw firm conclusions.

### 4.2.3 DWBA Calculations

The direct reactions (except the breakup one) leading to  ${}^3\text{He}$  and  ${}^4\text{He}$ - particle production were described in the DWBA framework [123]. In all cases, the potential of the entrance

channel ( ${}^7\text{Be} + {}^{28}\text{Si}$ ) was described using the global  ${}^7\text{Li}$  optical model parameters of Cook [193]. For the rest of the details, we will refer to each reaction separately starting with the  ${}^{28}\text{Si}({}^7\text{Be}, {}^6\text{Be}){}^{29}\text{Si}$  reaction.

Considering the unbound nature of  ${}^6\text{Be}$ , there are no optical model parameters available for reactions involving this nucleus. Instead, the global  ${}^6\text{Li}$  optical model parameters of Cook [193] were used. Stripping to both the  $0^+$  ground state and 1.67 MeV  $2^+$  resonances of  ${}^6\text{Be}$  was included. The spectroscopic factors for the  $\langle {}^7\text{Be} | {}^6\text{Be} + n \rangle$  overlaps were taken from Ref. [194]. The valence neutron was bound to a  ${}^6\text{Be}$  core in a Woods-Saxon well of radius  $1.25 \times A^{1/3}$  fm and diffuseness 0.65 fm. A Thomas-form spin-orbit potential of the same geometry and fixed depth of 6.0 MeV was also included, while the depth of the central well was adjusted such as to reproduce the experimental binding energy. Moreover, stripping to the following states of  ${}^{29}\text{Si}$  was included: 0.0 MeV  $1/2^+$ , 1.27 MeV  $3/2^+$ , 2.03 MeV  $5/2^+$ , 3.62 MeV  $7/2^-$ , 4.94 MeV  $3/2^-$  and 6.20 MeV  $7/2^-$ . The spectroscopic factors for the  $\langle {}^{29}\text{Si} | {}^{28}\text{Si} + n \rangle$  overlaps were taken from Ref. [195].

For the  ${}^{28}\text{Si}({}^7\text{Be}, {}^8\text{Be}){}^{27}\text{Si}$  reaction, since  ${}^8\text{Be}$  is also unbound, the global  ${}^7\text{Li}$  optical model parameters from Ref. [193] were used for the exit channel potential. Pickup to both the  $0^+$  ground state and 3.03 MeV  $2^+$  resonances of  ${}^8\text{Be}$  was included and the spectroscopic factors for the  $\langle {}^8\text{Be} | {}^7\text{Be} + n \rangle$  overlaps were taken from Ref. [194]. The valence neutron was bound to a  ${}^7\text{Be}$  core in a Woods-Saxon well of radius  $1.25 \times A^{1/3}$  fm and diffuseness 0.65 fm. A Thomas-form spin-orbit potential of the same geometry and fixed depth of 6.0 MeV was also included, while the the depth of the central well was adjusted such as to reproduce the experimental binding energy. Moreover, pickup leading to the following states of  ${}^{27}\text{Si}$  was included: 0.0 MeV  $5/2^+$ , 0.78  $1/2^+$  and 0.96 MeV  $3/2^+$ . The spectroscopic factors for the  $\langle {}^{28}\text{Si} | {}^{27}\text{Si} + n \rangle$  overlaps were taken from Ref. [196]. In this reaction, the  ${}^8\text{Be}$  ejectile decays to two  $\alpha$  particles. This was taken into account in producing the angular distributions illustrated in Figure 4.17.

The calculations for the  ${}^{28}\text{Si}({}^7\text{Be}, {}^4\text{He}){}^{31}\text{S}$  reaction are more erratic, since there are no suitable spectroscopic factors available in the literature for the  $\langle {}^{31}\text{S} | {}^{28}\text{Si} + {}^3\text{He} \rangle$  overlaps. The only experimental indication for population of states in  ${}^{31}\text{S}$  comes from a measurement of the  ${}^{28}\text{Si}({}^6\text{Li}, {}^3\text{H}){}^{31}\text{S}$  reaction [197]. Here the 0.0 MeV  $1/2^+$ , 1.25 MeV  $3/2^+$ , and 4.45 MeV  $7/2^-$  states were the main states observed in  ${}^{31}\text{S}$ . The Q-matching conditions for this reaction favor the population of highly excited states ( $E_{exc} > 10$  MeV) close to or above the  ${}^3\text{He}$  emission threshold. Therefore, such calculations were not performed since there is insufficient information available to yield meaningful results.

Finally, in case of the  ${}^{28}\text{Si}({}^7\text{Be}, {}^3\text{He}){}^{32}\text{S}$  reaction the global  ${}^3\text{He}$  optical model parameters

of Ref. [198] were used for the exit channel potential. The spectroscopic factor for the  $\langle {}^7\text{Be} | {}^4\text{He} + {}^3\text{He} \rangle$  overlap was set equal to 1.0 and the  ${}^4\text{He} + {}^3\text{He}$  binding potential was taken from Ref. [199]. Stripping leading to the following states in  ${}^{32}\text{S}$  was included: 0.0 MeV  $0^+$ , 2.23 MeV  $2^+$ , 3.78 MeV  $0^+$ , 4.46 MeV  $4^+$ , 5.01 MeV  $3^-$ , 5.80 MeV  $1^-$ , 6.76 MeV  $3^-$ , 7.43 MeV  $1^-$ , and 8.49 MeV  $1^-$ . Since the last two states are unbound with respect to the  ${}^4\text{He}$  emission threshold of  ${}^{32}\text{S}$ , the form factors in this particular case were calculated using the weak binding energy approximation with a “binding energy” of 0.01 MeV. For these states, spectroscopic factors were considered from the reaction  ${}^{28}\text{Si}({}^6\text{Li},d){}^{32}\text{S}$  reported in Ref. [200].

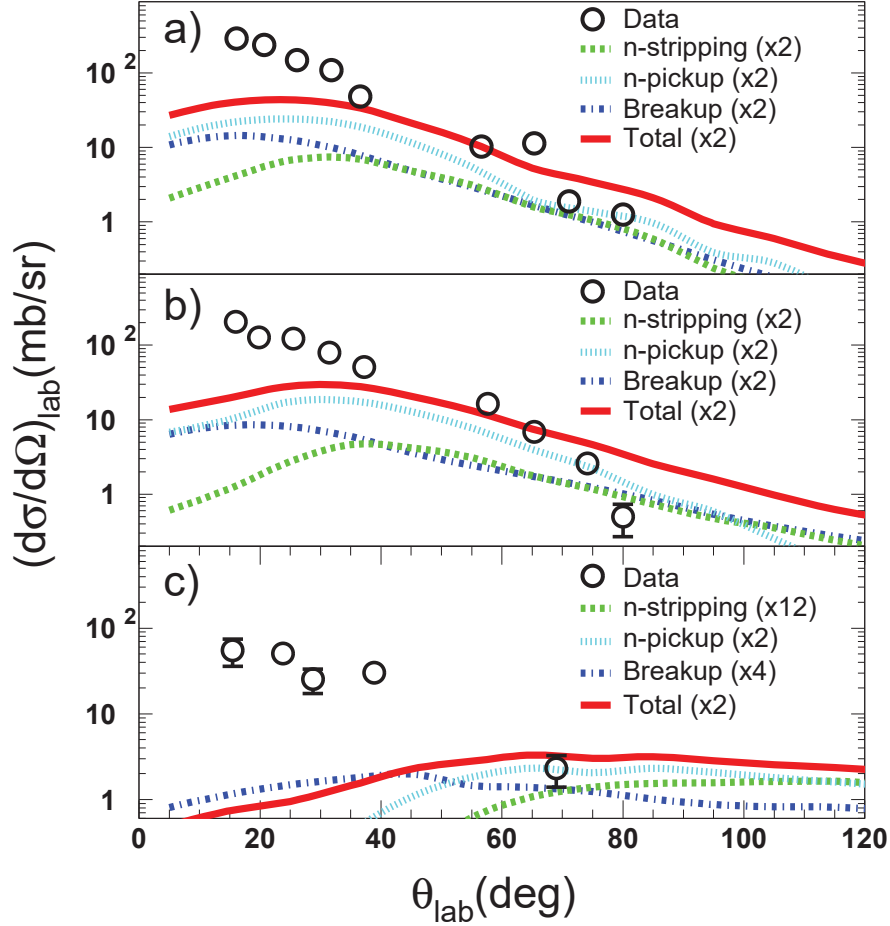


Figure 4.17: Angular distributions for  $\alpha$ -particle production due to direct processes at (a) 22.0 MeV, (b) 19.8 MeV and (c) 13.2 MeV. Experimental data are denoted with the black open circles, DWBA calculations for neutron stripping with the dashed green line and for neutron pickup with the dotted cyan line, while CDCC calculations for the breakup are denoted with the dotted-dashed blue line. The sum of the three processes is depicted with the solid red line. The remaining part may be attributed to  ${}^3\text{He}$  stripping. The multiplication factors are arbitrary for a better display of the various processes. Errors in the data are solely due to the experimental uncertainties of total  $\alpha$  production.

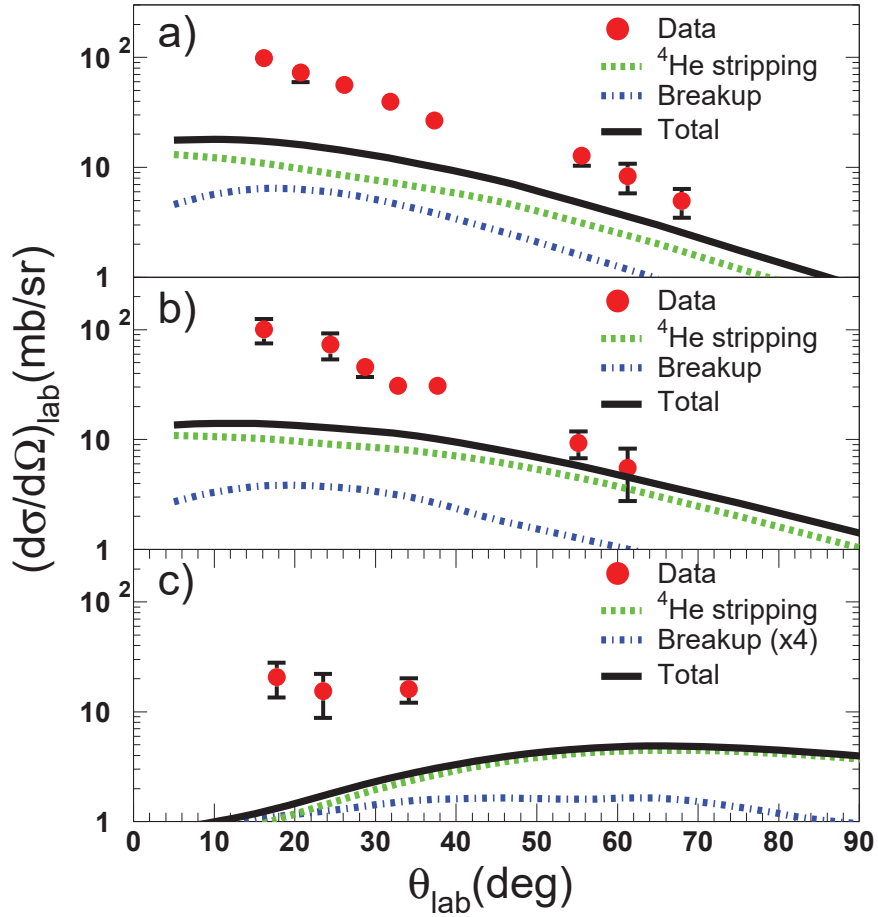


Figure 4.18: Angular distributions for  ${}^3\text{He}$ -particle production at (a) 22.0 MeV, (b) 19.8 MeV and (c) 13.2 MeV. Experimental data are denoted with the red circles, DWBA calculations for the  ${}^4\text{He}$  stripping with the dashed green line and CDCC calculations for the breakup are denoted with the dotted-dashed blue line. The sum of the two processes is depicted with the solid black line. The multiplication factor (panel c) for breakup is arbitrary, for a better visual view.

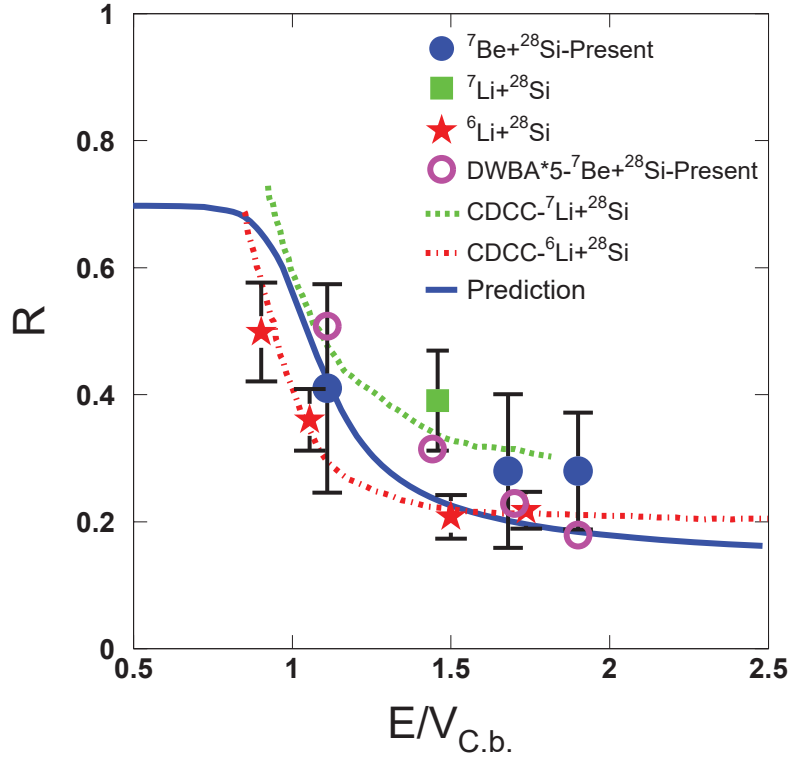


Figure 4.19: Energy evolution of ratios,  $R$ , of direct to total reaction cross sections. The present results for  ${}^7\text{Be} + {}^{28}\text{Si}$ , designated with the solid blue circles, are compared with previous results for  ${}^6\text{Li} + {}^{28}\text{Si}$  (red stars) and  ${}^7\text{Li} + {}^{28}\text{Si}$  (green square) [17]. They are also compared with a phenomenological prediction (solid blue line) for  ${}^7\text{Be} + {}^{28}\text{Si}$ , outlined in Ref. [68]. Previous calculated ratios for  ${}^6\text{Li} + {}^{28}\text{Si}$  and  ${}^7\text{Li} + {}^{28}\text{Si}$  are also shown as the dotted-dashed red line and dotted green line, respectively [78]. These calculations were based on total reaction cross sections deduced from a CDCC calculation and fusion cross sections deduced from a BPM model. In the latter case an energy dependent potential was taken into account, derived from the CDCC calculations according to the prescription of Thompson [201]. The open circles correspond to the present DWBA calculations, multiplied by 5 to match the data.

# Chapter 5

## Conclusions - Summary

In the present work, we have investigated the elastic scattering and the relevant reaction mechanisms for the system  ${}^7\text{Be} + {}^{28}\text{Si}$  at near barrier energies. Angular distribution for the elastically scattered  ${}^7\text{Be}$  ions were obtained at four energies, namely 22.0, 19.8, 17.2 and 13.2 MeV ( $E/V_{C.b.} = 1.14, 1.48, 1.71, 1.90$ ), while angular distribution for the reaction products  ${}^3\text{He}$  and  ${}^4\text{He}$ , the cluster constituents of  ${}^7\text{Be}$ , were obtained at 22.0, 19.8 and 13.2 MeV.

The elastic scattering data were analyzed into a double folding framework by using the BDM3Y1 interaction and the energy evolution of the real and imaginary part of the optical potential was deduced. Due to the large errors, it was not possible to draw firm conclusions solely from the elastic scattering data but only in conjunction with the  $\alpha$  - production ones. However, from the elastic scattering data, the trend seems to be compatible with a standard threshold anomaly at least in what concerns the imaginary part, with a decreasing magnitude as we approach the barrier from higher to lower energies. The agreement of the present data with a dispersion relation cannot be confirmed, as in the critical position of the real potential, where a peak should appear, we possess only one datum. On the other hand, taking into account all information relevant to previous data of  ${}^6,{}^7\text{Li} + {}^{28}\text{Si}$ , analyzed in the same framework as is the present case, we can in principle conclude that both mirror nuclei,  ${}^7\text{Li}$  and  ${}^7\text{Be}$  present the same energy dependence of the optical potential. This is close to the standard threshold anomaly, from the point of view of the decreasing imaginary potential but where possibly the dispersion relation does not hold [19]. This evidence, if combined with the results of the  $\alpha$  - production data, collected at the same experiment and reported in Ref. [160], indicates with some confidence the similarity between the two mirror nuclei. In Ref. [160], the fusion hindrance of both  ${}^7\text{Li}$  and  ${}^7\text{Be}$  versus  ${}^6\text{Li}$  was reported and the similarity between the two mirror nuclei was suggested. Based on the fact that two different reaction channels yielded

the same result, we can confirm in this study the similarity between the two mirror nuclei,  ${}^7\text{Li}$  and  ${}^7\text{Be}$ .

Our optical model analysis also yielded total reaction cross sections which were found to be in very good agreement with the values obtained via the present analysis of  ${}^3,{}^4\text{He}$ -particle production and global phenomenological predictions [68]. As total reaction cross sections are traditionally used to restrict the imaginary part of the optical potential, this compatibility further supports our result for the energy dependence of the optical potential. This raises questions for the dependence of the new or the standard threshold anomaly on the breakup threshold.  ${}^7\text{Be}$  nucleus has a breakup threshold of 1.59 MeV similar to that of  ${}^6\text{Li}$ , 1.47 MeV, and not of  ${}^7\text{Li}$  with 2.47 MeV, but still it resembles rather its mirror encounter and not  ${}^6\text{Li}$ . Further on, our total reaction cross sections were also considered in a systematic framework and were found in very good compatibility with results of other weakly bound, stable as well as radioactive, projectiles on similar mass targets.

For a more global description of the elastic scattering data, we have performed one, two channel and full CDCC calculations. It was found that the coupling to inelastic excitations of  ${}^7\text{Be}$  is unimportant, while couplings to continuum are substantial but not very strong.

From the point of view of reaction mechanisms, according to the measured light-particle production and the calculations of relevant compound-nucleus and direct single neutron stripping and pickup reaction processes, large  ${}^3\text{He}$ - and  ${}^4\text{He}$ -stripping channels may be inferred. These were obtained by subtracting from total direct cross sections the single neutron stripping and pickup channel contribution. It should be noted that the DWBA calculations [123] of single neutron stripping and pickup should be reasonably quantitatively accurate, since such processes are usually well described. Also, the contribution of the breakup to the  ${}^3,{}^4\text{He}$ -particle production is estimated to be small according to our CDCC calculations. Therefore, strong  ${}^3\text{He}$ - ${}^4\text{He}$  reaction channels are inferred.

The relevant DWBA calculations for the  ${}^{28}\text{Si}({}^7\text{Be}, {}^4\text{He}){}^{31}\text{S}$  and  ${}^{28}\text{Si}({}^7\text{Be}, {}^3\text{He}){}^{32}\text{S}$  reactions which might shed more light on the large  ${}^3\text{He}$ - and  ${}^4\text{He}$ - particle production are erratic. The optimum Q-values vary from -4 to -8 MeV and -4 to  $\sim$ -9 for the first and the second reaction respectively, for incident energies of 13.2 to 22.0 MeV. This implies preferential population of states in the residual nucleus at excitation energies where no spectroscopic factors are available. Thus, theoretical calculations for the  ${}^{28}\text{Si}({}^7\text{Be}, {}^4\text{He}){}^{31}\text{S}$  were not performed. In case of the  ${}^{28}\text{Si}({}^7\text{Be}, {}^3\text{He}){}^{32}\text{S}$  reaction, DWBA calculations were performed, using the available spectroscopic factors which however correspond to a limited excitation energy range in the  ${}^{32}\text{S}$  covered by the Q optimum value. It was found that the calculations underpredict the data.

This may be due to the fact that absolute spectroscopic factors for  $\alpha$  transfer reactions are ambiguously determined and in fact, factors of 5 or more between values for the same target obtained with different reactions and at different bombarding energies are common. This may easily explain why, although the DWBA calculations are in reasonable qualitative agreement with the data, underpredict their absolute values.

The compound nucleus contribution to the total  $\alpha$ -particle production was estimated by renormalizing the theoretical angular distributions from evaporated  $\alpha$ -particles, calculated within the statistical model framework [182], to the backward angle data, enabling the direct component to be separated. Subsequently, using the  $\alpha$ -particle multiplicities, calculated in the same statistical framework, and the cross sections due to compound nucleus formation, fusion cross sections were deduced. Fusion cross sections were considered in a systematics involving other, stable weakly bound and radioactive projectiles on the same or similar mass targets and present good consistency between each other as well as the UFF to within an uncertainty band of 10% to 20%. This does not preclude the behavior observed below the barrier for the same projectile but heavier targets, where small to very large enhancements have been reported. It is therefore an open question whether fusion below the barrier for proton rich nuclei is enhanced, in contrast to the behavior of neutron rich nuclei, and whether this is connected with the target mass. It should be underlined, however, that the present results, considered in a systematic framework with the low mass target  $^{28}\text{Si}$ , indicate a hindrance of fusion below the barrier rather than an enhancement. This hindrance was observed before for  $^7\text{Li}$  on various targets [78, 80–83] indicating a similarity between the two mirror nuclei.

Total reaction cross sections were formed as the sum of direct and fusion cross sections and the energy evolution of the ratio direct to total was mapped. The energy evolution for the system under study exhibits the same increasing trend approaching the barrier from higher to lower energies as for the stable weakly bound projectiles  $^6\text{Li}$  and  $^7\text{Li}$  on the same target. However, the results follow in magnitude those for  $^7\text{Li}$ , where we observe larger direct to total ratios due to an enhancement of transfer channels at the expense of fusion. Indeed, the present fusion results for  $^7\text{Be}$ , if compared with those for  $^{6,7}\text{Li}$  on the same target,  $^{28}\text{Si}$ , are in perfect agreement with previous results for  $^7\text{Li}$ . This fact, as it was already mentioned above, together with the results obtained from our optical model analysis present a strong evidence that  $^7\text{Be}$  resembles its mirror nucleus,  $^7\text{Li}$ , and not  $^6\text{Li}$  one.

In summary,

The energy dependence of the optical potential was sought for the system  $^7\text{Be} + ^{28}\text{Si}$  at near

barrier energies via elastic scattering measurements. Comparisons between  ${}^7\text{Be}$  -present data and  ${}^6,{}^7\text{Li}$  -previous data on the same target showed that,  ${}^7\text{Be}$  resembles its mirror nucleus and not  ${}^6\text{Li}$  one. The behavior of imaginary part of the optical potential is compatible with the standard threshold anomaly, while the real part cannot be definitely interpreted into dispersion relations framework, due to the limited data points around Coulomb barrier. It should be noted that the similarity between  ${}^7\text{Be}$  and  ${}^7\text{Li}$  is also validated from the analysis of fusion data, where fusion hindrance is indicated below barrier for both  ${}^7\text{Be}$  and  ${}^7\text{Li}$  nuclei. This may be related to the large transfer cross sections, observed for the two mirror nuclei, which act at expense of the fusion ones. In our case, the bulk of the transfer cross sections is attributed to  ${}^3\text{He}$  and  ${}^4\text{He}$  stripping reactions.

# References

- [1] J. S. Lilley, B. R. Fulton, M. A. Nagarajan et al., Phys. Lett. B **151**, 181 (1985).
- [2] A. Baeza, B. Bilwes, R. Bilwes et al., Nucl. Phys. A **419**, 412 (1984).
- [3] M. A. Nagarajan, C. C. Mahaux and G. R. Satchler, Phys. Rev. Lett. **54**, 1136 (1985).
- [4] C. Mahaux, H. Ngô, G. R. Satchler, Nucl. Phys. A **449**, 354 (1986).
- [5] G. R. Satchler, Phys. Rep. **199**, 147 (1991).
- [6] L. F. Canto, P. R. S. Gomes, R. Donangelo et al., Phys. Rep. **424**, 1 (2006).
- [7] N. Keeley, R. Raabe, N. Alamanos et al., Prog. Part. Nucl. Phys. **59**, 579 (2007).
- [8] N. Keeley, N. Alamanos, K. W. Kemper et al., Prog. Part. Nucl. Phys. **63**, 396 (2009).
- [9] P. R. S. Gomes, J. Lubian, L. F. Canto et al., Few-Body Syst. **57**, 165 (2016).
- [10] C. Beck, Nucl. Phys. A **787**, 251c (2007).
- [11] C. Beck, N. Rowley, P. Papka et al., Nucl. Phys. A **834**, 440c (2010).
- [12] Y. Sakuragi, M. Yahiro and M. Kamimura, Prog. Theor. Phys. **68**, 322 (1982).
- [13] Y. Sakuragi, M. Yahiro and M. Kamimura, Prog. Theor. Phys. **70**, 322 (1983).
- [14] N. Keeley, S. J. Bennett, N. M. Clarke et al., Nucl. Phys. A **571**, 326 (1994).
- [15] A. M. M. Maciel, P. R. S. Gomes, J. Lubian et al., Phys. Rev. C **59**, 2103 (1999).
- [16] A. Pakou, N. Alamanos, A. Lagoyannis et al., Phys. Lett. B **556**, 21 (2003).
- [17] A. Pakou, N. Alamanos, G. Doukelis et al., Phys. Rev. C **69**, 054602 (2004).
- [18] K. Zerva, N. Patronis, A. Pakou et al., Phys. Rev. C **80**, 017601 (2009).

- [19] K. Zerva, A. Pakou, K. Rusek et al., Phys. Rev. C **82**, 044607 (2010).
- [20] K. Zerva, A. Pakou, N. Patronis et al., Eur. Phys. Journal A **48**, 102 (2012).
- [21] M. S. Hussein, P. R. S. Gomes, J. Lubian et al., Phys. Rev. C **73**, 044610 (2006); Erratum, Phys. Rev. C **76**, 019902(E) (2007).
- [22] J. M. Figueira, D. Abriola, J. O. Fernández Niello et al., Phys. Rev. C **73**, 054603 (2006).
- [23] M. Biswas, Subinit Roy, M. Sinha et al., Nucl. Phys. A **802**, 67 (2008).
- [24] F. A. Souza, L. A. S. leal, N. Carlin et al., Phys. Rev. C **75**, 044601 (2007).
- [25] M. Zadro, P. Figuera, A. Di Pietro et al., Phys. Rev. C **80**, 064610 (2009).
- [26] L. Fimiani, J. M. Figueira, G. V. Martí et al., Phys. Rev. C **86**, 044607 (2012).
- [27] H. Kumawat, V. Jha, B. J. Roy et al., Phys. Rev. C **78**, 044617 (2008).
- [28] N. N. Deshmukh, S. Mukherjee, D. Patel et al., Phys. Rev. C **83**, 024607 (2011).
- [29] J. M. Figueira, J. O. Fernández Niello, A. Arazi et al., Phys. Rev. C **81**, 024613 (2010).
- [30] S. Santra, S. Kailas, K. Ramachandran et al., Phys. Rev. C **83**, 034616 (2011).
- [31] Shradha Dubey, S. Mukherjee, D. C. Biswas et al., Phys. Rev. C **89**, 014610 (2014).
- [32] L. F. Canto, P. R. S. Gomes, R. Donangelo et al., Phys. Rep. **596**, 1 (2015).
- [33] A. M. Sánchez-Benítez, D. Escrig, M. A. G. Álvarez et al., Nucl. Phys. A **803**, 30 (2008).
- [34] L. Acosta, A. M. Sánchez-Benítez, M. E. Gómez et al., Phys. Rev. C **84**, 044604 (2011).
- [35] A. R. Garcia, J. Lubian, I. Padron et al., Phys. Rev. C **76**, 067603 (2007).
- [36] A. Gómez Camacho, E. F. Aguilera, E. Martínez Quiroz et al., Nucl. Phys. A **833**, 156 (2010).
- [37] A. Gómez Camacho, E. F. Aguilera, P. R. S. Gomes et al., Phys. Rev. C **84**, 034615 (2011).
- [38] A. Gómez Camacho and E. F. Aguilera, Phys. Rev. C **90**, 064607 (2014).
- [39] V. Morcelle, R. Lichtenthäler, R. Linares et al., Phys. Rev. C **89**, 044611 (2014).

- [40] A. Di Pietro, V. Scuderi, A. M. Moro et al., *Phys. Rev. C* **85**, 054607 (2012).
- [41] M. Cubero, J. P. Fernández-García, M. Rodríguez-Gallardo et al., *Phys. Rev. Lett.* **109**, 262701 (2012).
- [42] J. P. Fernández-García, M. Cubero, L. Acosta et al., *Phys. Rev. C* **92**, 044608 (2015).
- [43] K. Rusek, N. Keeley, K. W. Kemper et al., *Phys. Rev. C* **67**, 041604(R) (2003).
- [44] Y. Kucuk, I. Boztosun and N. Keeley, *Phys. Rev. C* **79**, 067601 (2009).
- [45] N. Keeley, N. Alamanos, K. Rusek et al., *Phys. Rev. C* **71**, 014611 (2005).
- [46] A. Pakou, N. Alamanos, N. M. Clarke et al., *Phys. Lett. B* **633**, 691 (2006).
- [47] F. A. Souza, C. Beck, N. Carlin et al., *Nucl. Phys. A* **821**, 36 (2009).
- [48] F. A. Souza, N. Carlin, C. Beck et al., *Nucl. Phys. A* **834**, 420c (2010).
- [49] F. A. Souza, N. Carlin, C. Beck et al., *Eur. Phys. Journal A* **44**, 181 (2015).
- [50] C. Signorini, A. Edifizi, M. Mazzocco et al., *Phys. Rev. C* **67**, 044607 (2003).
- [51] D. H. Luong, M. Dasgupta, D. J. Hinde et al., *Phys. Rev. C* **88**, 034609 (2013).
- [52] S. Santra, V. V. Parkar, K. Ramachandran et al., *Phys. Lett. B* **677**, 139 (2009).
- [53] J. J. Kolata, H. Amro, F. D. becchetti et al., *Phys. Rev. C* **75**, 031302(R) (2007).
- [54] A. Pakou, K. Rusek, N. Alamanos et al., *Phys. Rev. C* **76**, 054601 (2007).
- [55] D. Gupta, C. Samanta, R. Kanungo et al., *Nucl. Phys. A* **646**, 161 (1999).
- [56] A. Shrivastava, A. Navin, N. Keeley et al., *Phys. Lett. B* **633**, 463 (2006).
- [57] S. K. Pandit, A. Shrivastava, K. Mahata et al., *Phys. Rev. C* **93**, 061602(R) (2016).
- [58] D. Gupta, C. Samanta, A. Chatterjee et al., *Nucl. Phys. A* **683**, 3 (2001).
- [59] A. Pakou, N. Alamanos, A. Gillibert et al., *Phys. Rev. Lett.* **90**, 202701 (2003).
- [60] A. Pakou, N. G. Nicolis, K. Rusek et al., *Phys. Rev. C* **71**, 064602 (2005).
- [61] H. Kumawat, V. Jha, V. V. Parkar et al., *Phys. Rev. C* **81**, 054601 (2010).
- [62] C. S. Palshetkar, S. Santra, A. Shrivastava et al., *Phys. Rev. C* **89**, 064610 (2014).

- [63] V. Scuderi, A. Di Pietro, P. Figuera et al., Phys. Rev. C **84**, 064604 (2011).
- [64] A. Di Pietro, P. Figuera, F. Amorini et al., Phys. Rev. C **69**, 044613 (2004)
- [65] E. F. Aguilera, J. J. Kolata, F. M. Nunes et al., Phys. Rev. Lett. **84**, 5058 (2000).
- [66] D. Escrig, A. M. Sánchez-Benítez, A. M. Moro et al., Nucl. Phys. A **792**, 2 (2007).
- [67] M. Mazzocco, D. Torresi, D. Pierroutsakou et al., Phys. Rev. C **92**, 024615 (2015).
- [68] A. Pakou, D. Pierroutsakou, M. Mazzocco et al., Eur. Phys. Journal A **51**, 55 (2015).
- [69] J. J. Kolata, V. Guimarães, D. Peterson et al., Phys. Rev. Lett. **81**, 4580 (1998).
- [70] E. Martinez-Quiroz, E. F. Aguilera, D. Lizcano et al., Phys. Rev. C **90**, 014616 (2014).
- [71] R. Raabe, J. L. Sida, J. L. Charvet et al., Nature (London) **431**, 823 (2004).
- [72] A. Lemasson, A. Shrivastava, A. Navin et al., Phys. Rev. Lett. **103**, 232701 (2009).
- [73] R. Raabe, C. Angulo, J. L. Charvet et al., Phys. Rev. C **74**, 044606 (2006).
- [74] C. Y. Wong, Phys. Rev. Lett. **31**, 766 (1973).
- [75] A. Pakou and K. Rusek, Phys. Rev. C **69**, 057602 (2004).
- [76] A. Pakou, Phys. Rev. C **78**, 067601 (2008).
- [77] D. Roubos, A. Pakou, N. Alamanos et al., Phys. Rev. C **73**, 051603(R) (2006).
- [78] A. Pakou, K. Rusek, N. Alamanos et al., Eur. Phys. Journal A **39**, 187 (2009).
- [79] A. Pakou, A. Musumarra, D. Pierroutsakou et al., Nucl. Phys. A **784**, 13 (2007).
- [80] C. Beck, F. A. Souza, N. Rowley et al., Phys. Rev. C **67**, 054602 (2003).
- [81] A. Di Pietro, P. Figuera, E. Strano et al., Phys. Rev. C **87**, 064614 (2013).
- [82] M. Ray, A. Mukherjee, M. K. Pradhan et al., Phys. Rev. C **78**, 064617 (2008).
- [83] M. Sinha, H. Majumdar, P. Basu et al., Eur. Phys. Journal A **44**, 403 (2010).
- [84] K. S. Krane, Introductory Nuclear Physics, John Wiley & Sons, Inc. (1988).
- [85] S. S. M. Wong, Introductory Nuclear Physics, Wiley - VCH Verlag GmbH and & Co. KGaA, second edition (2004).

- [86] L.S. Rodberg and R. M. Thaler, Introduction to the Quantum Theory of Scattering, Academic Press New York and London (1967).
- [87] P. E. Hodgson, E. Gadioli and E. Gadioli Erba, Introductory Nuclear Physics, Oxford University Press Inc., New York, second edition (1997).
- [88] J. R. Cox, Can. J. Math. Phys **5**, 1065 (1964).
- [89] T. Tamura, Annu. Rev. Nucl. Sci. **19**, 99 (1969)
- [90] G. H. Rawitscher, Phys. Rev. C **9**, 2210 (1974).
- [91] N. Austern, Y. Iseri, M. Kamimura et al., Phys. Rep. **154**, 125 (1987).
- [92] F. M. Nunes, Scholarpedia 6, 10497 (2011).
- [93] N. L. Upadhyay, A. Deltuva and F. M. Nunes, Phys. Rev. C **85**, 054621 (2012).
- [94] K. Rusek, K. W. Kemper, R. Wolski, Phys. Rev. C **64**, 044602 (2001).
- [95] V. Soukeras, A. Pakou, F. Cappuzzello et al., Phys. Rev. C **91**, 057601 (2015).
- [96] A. Pakou, V. Soukeras, F. Cappuzzello et al., Phys. Rev. C **94**, 014604 (2016).
- [97] Y. Sakuragi, M. Yahiro and M. Kamimura, Prog. Theor. Phys. Suppl. **89**, 136 (1986).
- [98] I. J. Thompson, Comput. Phys. Rep. **7**, 167 (1988).
- [99] R. R. Roy and B. P. Nigam, Nuclear Physics Theory and Experiment, John Wiley and Sons, Inc. (1967).
- [100] A. G. Sitenko, Theory of Nuclear reactions, World Scientific Publishing Co. Pte. Ltd. (1990).
- [101] R. D. Woods and D. S. Saxon, Phys. Rev. **95**, 577 (1954).
- [102] G. Igo, Phys. Rev. **115**, 1665 (1959).
- [103] M. E. Cage, A. J. Cole and G. J. Pyle, Nucl. Phys. A **201**, 418 (1973).
- [104] D. H. Feng, A. R. Barnett, L. J. B. Goldfarb, Phys. Rev. C **13**, 1151 (1976).
- [105] M. M. Shalaby and G. R. Satchler, Nucl. Phys. A **442**, 469 (1985).
- [106] A. R. barnett and J. S. Lilley, Phys. Rev. C **9**, 2010 (1974).

- [107] C. Tenreiro, J. C. Acquadro, P. A. B. Freitas et al., *Phys. Rev. C* **53**, 2870 (1996).
- [108] A. Zerwekh, R. L. Neto, N. Added et al., *Phys. Rev. C* **58**, 3445 (1998).
- [109] S. Dubey, S. Mukherjee, D. Patel et al., *Eur. Phys. Journal Web Conf.* **86**, 00008 (2015).
- [110] J. G. Cramer and R. M. DeVries, *Phys. Rev. C* **22**, 91 (1980).
- [111] K. Rusek, Z. Moroz, R. Čaplar et al., *Nucl. Phys. A* **407**, 208 (1983).
- [112] V. Soukeras, Master Thesis: Elastic scattering for the system  $^{20}\text{Ne} + ^{28}\text{Si}$  at near barrier energies, University of Ioannina, (2013).
- [113] G. R. Satchler and W. G. Love, *Phys. Rep.* **55**, 183 (1979).
- [114] N. Alamanos and P. Roussel-Chomaz, *Ann. Phys. Fr.* **21**, 601 (1996).
- [115] G. Bertsch, J. Borysowicz, H. McManus, *Nucl. Phys. A* **284**, 399 (1977).
- [116] D. T. Khoa and W. von Oertzen, *Phys. Lett. B* **304**, 8 (1993).
- [117] D. T. Khoa and W. von Oertzen, *Phys. Lett. B* **342**, 6 (1995).
- [118] D. J. Griffiths, *Introduction to Electrodynamics*, Prentice-Hall, Inc., third edition (1999).
- [119] A. R. Forouhi, I. Bloomer, *Phys. Rev. B* **34**, 7018 (1986).
- [120] H. M. Nussenzveig, *Causality and Dispersion Relations*, Academic, New York (1972).
- [121] G. R. Satchler, *Introduction to Nuclear Reactions*, second edition (1990).
- [122] W. D. M. Rae, A. J. Cole, B. G. Harvey et al., *Phys. Rev. C* **30**, 158 (1984).
- [123] N. Keeley. Private communication.
- [124] P. E. Hodgson, *Rep. Prog. Phys.* **50**, 1171 (1987).
- [125] W. Hauser and H. Feshbach, *Phys. Rev.* **87**, 366 (1952).
- [126] V. Weisskopf, *Phys. Rev.* **52**, 295 (1937).
- [127] V. F. Weisskopf and D. H. Ewing, *Phys. Rev.* **57**, 472 (1940).
- [128] H. L. Pai, *Can. J. Phys.* **54**, 1421 (1976).
- [129] H. A. Bethe, *Phys. Rev.* **50**, 332 (1936).

- [130] A. Gilbert and A. G. W. Cameron, *Can. J. Phys.* **43**, 1446 (1965).
- [131] F. Pühlhofer, *Nucl. Phys. A* **280**, 267 (1977).
- [132] A. Gavron, *Phys. Rev. C* **21**, 230 (1980).
- [133] V. Z. Maidikov, T. Glodariu, M. La Commara et al., *Nucl. Phys. A* **746**, 389c (2004).
- [134] D. Pierroutsakou, B. Martin, T. Glodariu et al., *Eur. Phys. J. Special Topics* **150**, 47 (2007).
- [135] F. Farinon, T. Glodariu, M. Mazzocco et al., *Nucl. Instr. and Meth. B* **266**, 4097 (2008).
- [136] M. Mazzocco, F. Farinon, T. Glodariu et al., *Nucl. Instr. and Meth. B* **266**, 4665 (2008).
- [137] M. Mazzocco, D. Torresi, E. Strano et al., *Nucl. Instr. and Meth. B* **317**, 223 (2013).
- [138] E. Strano, A. Anastasio, M. Bettini et al., *Nucl. Instr. and Meth. B* **317**, 657 (2013).
- [139] D. Pierroutsakou, A. Boiano, C. Boiano et al., *Nucl. Instr. and Meth. A* **834**, 46 (2016).
- [140] M. Mazzocco, *AIP Conf. Proc.* **1595**, 178 (2014).
- [141] W. R. Leo, *Techniques for Nuclear and Particle Physics Experiments: A How-to Approach*, Springer-Verlag, second revised edition (1994).
- [142] G. F. Knoll, *Radiation Detection and Measurements*, John Wiley & Sons, Inc., third edition (2000).
- [143] G. Marquínez-Durán, L. Acosta, R. Berjillos et al., *Nucl. Instr. and Meth. A* **755**, 69 (2014).
- [144] G. Marquínez-Durán, Master Thesis: Dispersion Elastica del sistema  ${}^8\text{He}+{}^{208}\text{Pb}$  a energia  $E_{lab}= 22$  MeV, Universidad de Huelva, (2012).
- [145] Y. Blumenfeld, F. Auger, J. E. Sauvestre et al., *Nucl. Instr. and Meth. A* **421**, 471 (1999).
- [146] E. Pollaco, D. Beaumel, P. Roussel-Chomaz et al., *Eur. Phys. Journal A* **25**, (s01), 287 (2005).
- [147] M. Labiche, W. N. Catford, R. C. Lemmon et al., *Nucl. Instr. and Meth. A* **614**, 439 (2010).

- [148] B. Davin, R. T. de Souza, R. Yanez et al., Nucl. Instr. and Meth. A **473**, 302 (2001).
- [149] M. S. Wallace, M. A. Famiano, M. -J. van Goethem et al., Nucl. Instr. and Meth. A **583**, 302 (2007).
- [150] T. Davinson, W. Bradfiel-Smith, S. Cherubini et al., Nucl. Instr. and Meth. A **454**, 350 (2000).
- [151] C. Boiano, A. Guglielmetti, S. Riboldi, 2012 IEEE Nuclear Science Symposium and Medical Imaging Conference Record (NSS/MIC), **vol. N14-34**, p. 865 (2012).
- [152] G. L. Engel, M. Sadasivam, M. Nethi et al., Nucl. Instr. and Meth. A **573**, 418 (2007).
- [153] V. I. Zagrebaev, A. S. Denikin, A. P. Alekseev et al., OM code of NRV, <http://nrv.jinr.ru/nrv/>
- [154] O. B. Tarasov, D. Bazin, Nucl. Instr. and Meth. B **266**, 4657 (2008).
- [155] R. Brun, F. Rademakers, Nucl. Instr. and Meth. A **389**, 81 (1997).
- [156] O. Sgouros, A. Pakou, D. Pierroutsakou et al., Phys. Rev. C **95**, 054609 (2017).
- [157] O. Sgouros, A. Pakou, D. Pierroutsakou et al., AIP Conf. Proc. **1645**, 397, (2015) and INFN - LNL Report **241**, 54 (2015).
- [158] Application software group, Computer and Networks Division, CERN Program Library, PAW-Physics Analysis Workstation, CERN, Geneva, 1995.
- [159] K. K. Olimov, K. Olimov, V. V. Lugovoi et al., Int. Jour. Mod. Phys. E **25**, 1650021 (2016).
- [160] O. Sgouros, A. Pakou, D. Pierroutsakou et al., Phys. Rev. C **94**, 044623 (2016).
- [161] A. Pakou. Private communication.
- [162] J. Raynal, Phys. Rev. C **23**, 2571 (1981).
- [163] H. D. DeVries, C. W. Jager and C. DeVries, Atomic data and Nuclear Data Tables **14**, 479 (1974).
- [164] A. Bhagwat, Y. K. Gambhir and S. H. Patil, Eur. Phys. Journal A **8**, 511 (2000).
- [165] Y. Sert and I. Boztosun, Int. Jour. Mod. Phys. E **25**, 1650071 (2016).

- [166] M. Biswas, Phys. Rev. C **77**, 017602 (2008).
- [167] K. Zerva, PhD Thesis: Optical potential and reaction mechanisms of weakly bound nuclei at near barrier energies, University of Ioannina, (2013).
- [168] P. R. S. Gomes, G. Lubian, I. Padron et al., Phys. Rev. C **71**, 017601 (2005).
- [169] L. R. Gasques, L. C. Chamon, D. Pereira et al., Phys. Rev. C **69**, 034603 (2004).
- [170] L. F. Canto, P. R. S. Gomes, J. Lubian et al., J. Phys. G **36**, 015109 (2009).
- [171] L. F. Canto, P. R. S. Gomes, J. Lubian et al., Nucl. Phys. A **821**, 51 (2009).
- [172] L. F. Canto, D. R. Mendes Junior, P. R. S. Gomes et al., Phys. Rev. C **92**, 014626 (2015).
- [173] J. M. B. Shorto, P. R. S. Gomes, J. Lubian et al., Phys. Lett. B **678**, 77 (2009).
- [174] P. R. Christensen and A. Winther, Phys. Lett. B **65**, 19 (1976).
- [175] E. A. Benjamin, A. Lépine-Szily, D. R. Mendes Junior et al., Phys. Lett. B **647**, 30 (2007).
- [176] J. M. Figueira, J. O. Fernández Niello, D. Abriola et al., Phys. Rev. C **75**, 017602 (2007).
- [177] K. Kalita, S. Verma, R. Singh et al., Phys. Rev. C **73**, 024609 (2006).
- [178] V. Morcelle, R. Lichtenthäler, A. Lépine-Szily et al., Phys. Rev. C **95**, 014615 (2017).
- [179] N. Keeley, K. W. Kemper and K. Rusek, Phys. Rev. C **66**, 044605 (2002).
- [180] W. Wühr, A. Hofmann, and G. Philipp, Z. Physik **269**, 365 (1974).
- [181] B. H. Wildenthal and P. W. M. Glaudemans, Nucl. Phys. A **92**, 353 (1967).
- [182] N. G. Nicolis. Private communication.
- [183] J. R. Huizenga and G. Igo, Nucl. Phys. **29**, 462 (1962).
- [184] R. Bass, Phys. Rev. Lett. **39**, 265 (1977).
- [185] E. F. Aguilera, P. Amador-Valenzuela, E. Martinez-Quiroz et al., Phys. Rev. C **93**, 034613 (2016).
- [186] L. McFadden and G. R. Satchler, Nucl. Phys. **84**, 177 (1966).

- [187] G. R. Satchler, Nucl. Phys. **70**, 177 (1965).
- [188] A. Pakou, K. Rusek, N. Alamanos et al., internal report, Nuclear Physics Laboratory, University of Ioannina, 2008 (unpublished), <http://npl.physics.uoi.gr/preprints.htm>
- [189] A. Pakou, E. Stiliaris, D. Pierroutsakou et al., Phys. Rev. C **87**, 014619 (2013).
- [190] M. Sinha, H. Majumdar, R. Bhattacharya et al., Phys. Rev. C **76**, 027603 (2007).
- [191] M. Sinha, H. Majumdar, P. Basu et al., Phys. Rev. C **78**, 027601 (2008).
- [192] G. V. Martí, P. R. S. Gomes, M. D. Rodríguez et al., Phys. Rev. C **71**, 027602 (2005).
- [193] J. Cook, Nucl. Phys. A **388**, 153 (1982).
- [194] S. Cohen and D. Kurath, Nucl. Phys. A **101**, 1 (1967).
- [195] M. C. Mermaz, C. A. Whitten, Jr., J. W. Champlin et al., Phys. Rev. C **4**, 1778 (1971).
- [196] C. A. Whitten, Jr., M. C. Mermaz and D. M. Bromley, Phys. Rev. C **1**, 1455 (1970).
- [197] C. W. Woods, N. Stein and J. W. Sunier, Phys. Rev. C **17**, 66 (1978).
- [198] D. Y. Pang, P. Roussel-Chomaz, H. Savajols et al., Phys. Rev. C **79**, 024615 (2009).
- [199] B. Buck and A. C. Merchant, J. Phys. G **14**, L211 (1988).
- [200] T. Madhusoodhanan, S. Mandal, R. Shyam et al., J. Phys. G **25**, 1897 (1999).
- [201] I. J. Thompson, M. A. Nagarajan, J. S. Lilley et al., Nucl. Phys. A **505**, 84 (1989).
- [202] G. Marquínez-Durán and A. M. Sánchez-Benítez. Private communication.

# Appendix A

## Event by event analysis code

The event by event analysis was performed with the data analysis package ROOT [155]. For that, the information provided by the two PPAC's and the DSSSD detectors was used in order to determine the scattering angle for each event. Three different subroutines were written in C language. The philosophy of the subroutines implemented in the ROOT code is described in the following three steps:

### 1. Beam particle trajectory reconstruction between PPAC's-target

The first step is referred to the reconstruction of the beam particle trajectories via the information of the two PPAC's and therefore to the incident angle in the target. The two PPAC's are X-Y position sensitive detectors. When the beam particles are passing through the sensitive volume of a PPAC, an electron avalanche is created and the charge is collected by the anode wires. The signal produced by the avalanche is traveling through the anode wires towards the delay lines both on X and Y directions. Reaching the delay line, the signal is splitted into two direction (up and down or left and right). The time difference of the arrival time of the signal between the two ends of the delay line is proportional to the position of the incident particle. Absolute measurements of the position of the particles are obtained after calibrating the PPAC's as it was described in Chapter 2. Subsequently, by plotting the differences (Up-Down) and (Left-Right) we are able to determine the coordinates necessary to reconstruct the beam particle trajectories for each particle  $(X_A, Y_A, Z_A)$  and  $(X_B, Y_B, Z_B)$  for PPAC<sub>A</sub> and PPAC<sub>B</sub> respectively with Z the distance from the target. The equation of a trajectory (straight line) that passes through the points A( $X_A, Y_A, Z_A$ ) of PPAC<sub>A</sub> and B( $X_B, Y_B, Z_B$ ) of PPAC<sub>B</sub> is given by the expression:

$$\frac{X - X_B}{X_B - X_A} = \frac{Y - Y_B}{Y_B - Y_A} = \frac{Z - Z_B}{Z_B - Z_A}. \quad (\text{A.1})$$

By using equation A.1 we can determine the reaction position on the target  $(X_t, Y_t)$  as follows:

$$\begin{aligned} X_t &= X_B + \frac{Z_t - Z_B}{Z_B - Z_A} (X_B - X_A) \\ Y_t &= Y_B + \frac{Z_t - Z_B}{Z_B - Z_A} (Y_B - Y_A) \end{aligned} \quad (\text{A.2})$$

where  $Z_t$  has to be substituted with the known coordinate in the target position,  $Z_t = 0$ .

## 2. Determination of the scattering angle assuming a point like beam spot

After the reaction occurs on the silicon target, the  ${}^7\text{Be}$  ions are scattered at various angles and are detected by six  $\Delta\text{E-E}$  DSSSD telescopes. For the determination of the scattering angle we need for each event to know the coordinates on the target as well as the coordinates on the strip that the event is detected. For reasons of simplicity in this step we consider the beam to be pencil like and the reaction to occur in the middle of the target. Subsequently, the coordinates of the strips have to be determined and will be described below.

The position information is represented by two numbers, corresponding to the combination of the vertical and the horizontal strips (pixel) that a particular event is detected. In order to obtain this information in absolute values, we have to determine the coordinates corresponding to each vertical and horizontal strip with respect to the target position. Starting with the coordinates of the central pixel of the detector, we may write [202]:

$$\begin{aligned} X_c &= \ell \sin(\theta_c) - \left[ \frac{0.50 * X_{dim}}{N} \cos(\theta_c) \right] \\ Y_c &= \frac{0.50 * Y_{dim}}{N} \\ Z_c &= \ell \cos(\theta_c) + \left[ \frac{0.50 * X_{dim}}{N} \sin(\theta_c) \right], \end{aligned} \quad (\text{A.3})$$

where  $\ell$  is the distance between the target and the center of each telescope,  $\theta_c$  is the mean

polar angle of each telescope (see Table 2.2),  $X_{dim}$  and  $Y_{dim}$  is the width and the height of the detector respectively and  $N$  is the number of strips included to the detector. Then, assuming a point like beam spot on the target position, using the following recursion relations the coordinates of each strip are determined with respect to the target position  $O(0,0,0)$  as [202]:

$$X_s(n) = \begin{cases} X_c - \left[ \frac{(7 - n/2) * X_{dim}}{N} \cos(\theta_c) \right], & \text{if } n = 0, 2, 4, \dots, 12 \\ X_c, & \text{if } n = 14 \\ X_c + \left[ \frac{(n/2 - 7) * X_{dim}}{N} \cos(\theta_c) \right], & \text{if } n = 16, 18, \dots, 32 \end{cases} \quad (\text{A.4})$$

$$Y_s(k) = \begin{cases} Y_c + 0.40 * (7 - k/2), & \text{if } k = 0, 2, 4, \dots, 12 \\ Y_c, & \text{if } k = 14 \\ Y_c - 0.40 * (k/2 - 7), & \text{if } k = 16, 18, \dots, 32 \end{cases} \quad (\text{A.5})$$

$$Z_s(n) = \begin{cases} Z_c + \left[ \frac{(7 - n/2) * X_{dim}}{N} \sin(\theta_c) \right], & \text{if } n = 0, 2, 4, \dots, 12 \\ Z_c, & \text{if } n = 14 \\ Z_c - \left[ \frac{(n/2 - 7) * X_{dim}}{N} \sin(\theta_c) \right], & \text{if } n = 16, 18, \dots, 32 \end{cases} \quad (\text{A.6})$$

where  $n(k) \in [0, 32]$  is the number of each vertical (horizontal) strip as it is registered in the root file.

### 3. Determination of the scattering angle using a finite dimensions beam spot

Step 2 refers to the ideal case of a point like beam spot on the target. However, the beam spot has finite dimensions and thus the reaction position on the target is different from the  $O(0,0,0)$  one. The correct position was already determined in step 1. Using this information, the position on the strip has to be corrected. The coordinates of each strip now with respect to the real reaction position for each event are given as:

$$\begin{aligned}
X(n) &= X_s(n) - X_t \\
Y(k) &= Y_s(k) - Y_t \\
Z(n) &= Z_s(n)
\end{aligned}
\tag{A.7}$$

Having obtained the coordinates of each strip with respect to the reaction vertex on the target, we can associate to each event a scattering angle  $\theta$  based on the coordinates of the pixel(n,k) that the particular event is detected as follows:

$$\theta = \cos^{-1} \left[ \frac{Z(n)}{\sqrt{X(n)^2 + Y(k)^2 + Z(n)^2}} \right]
\tag{A.8}$$

#### 4. Determination of the differential cross sections

Events with the same angle or with an angle inside an angular range corresponding to a particular vertical strip of each EXPADES detector ( $\Delta\theta \sim 2^\circ$ ) are summed up both for the elastic scattering on the silicon target as well as for the elastic scattering on a lead target used for the determination of the solid angles, and the differential cross sections are deduced via the following equation:

$$Ratio \equiv \frac{\sigma}{\sigma_{Ruth}^{Si}} = \frac{N_{Si}}{N_{Pb}} * K,
\tag{A.9}$$

where  $N_{Si}$  and  $N_{Pb}$  are the event by event counts corresponding to every strip ( $\Delta\theta \sim 2^\circ$ ) collected with the silicon and lead targets respectively and the constant K is determined assuming that at small scattering angles the ratio  $\sigma/\sigma_{Ruth}^{Si}$  between elastic scattering cross sections and Rutherford cross sections is 1.0.

# Appendix B

## Simulation Code

To obtain the alpha energy spectra arising from the decay of  ${}^6\text{Be}$  nucleus ( ${}^6\text{Be} \rightarrow \alpha + \text{p} + \text{p}$ ), a Monte Carlo simulation code was employed. The simulation code proceeds in four steps:

1. The angular distribution of the  ${}^7\text{Be} + {}^{28}\text{Si} \rightarrow {}^6\text{Be} + {}^{29}\text{Si}$  reaction, calculated in the center of mass system via code FRESKO [98], is fed as an input to the Monte Carlo code. Then,  $\theta_{c.m.}$  angles are randomly generated for the heavy ejectile  ${}^6\text{Be}$  with a frequency restricted by the probability of the reaction. Pairs  $(\theta_{c.m.}, P_{c.m.})$  are formed taking into account the following relation:

$$P_{c.m.} = M_{6Be} \sqrt{\frac{2M_{29Si}(E_{c.m.} + Q - E_x)}{M_{6Be}(M_{6Be} + M_{29Si})}}, \quad (\text{B.1})$$

where  $M_{6Be}$  and  $M_{29Si}$  is the mass of  ${}^6\text{Be}$  and  ${}^{29}\text{Si}$  respectively,  $E_{c.m.}$  is the energy of the two-body reaction in the center of mass system,  $Q$  is the Q-value of the two-body reaction and  $E_x$  is the excitation energy of  ${}^6\text{Be}$  nucleus. Subsequently, the pairs from the center of mass system are transformed to the laboratory system  $(\theta_{lab}, P_{lab})$  by using the appropriate jacobians.

2. The breakup process of the  ${}^6\text{Be}$  nucleus in its rest frame  $K$  is now considered.  ${}^6\text{Be}$  breaks up to three particles  $\alpha + \text{p} + \text{p}$ . The momentum for the two fragments is randomly generated but restricted to a maximum energy equal to the binding energy of  ${}^6\text{Be}$ . Also, the polar and azimuthal angles  $(\theta, \phi)$  are randomly generated and therefore the momentum components  $(P_{ix}, P_{iy}, P_{iz})$  where  $i=[1 \rightarrow \alpha, 2 \rightarrow \text{p}_1]$ , are defined. The momentum component of the third particle ( $i=3 \rightarrow \text{p}_2$ ) is finally defined by applying conservation laws of

momentum:

$$P_{3x} = -(P_{1x} + P_{2x}) \quad (\text{B.2})$$

$$P_{3y} = -(P_{1y} + P_{2y}) \quad (\text{B.3})$$

$$P_{3z} = -(P_{1z} + P_{2z}) \quad (\text{B.4})$$

3. In this third step we combine information from the first two steps, that is the momentum of  ${}^6\text{Be}$  in the laboratory frame and the momenta of the fragments in the rest frame of  ${}^6\text{Be}$ , for transforming the momentum components from system K to K' according to the prescription of Olimov et al. [159]. In this model the Z axis in the K system, is considered at the same direction as  $\mathbf{P}_{lab}$  (momentum of the  ${}^6\text{Be}$  nucleus in the laboratory system). K' is a system which is moving parallel to the K with relative velocity  $-V_{lab}$  with  $V_{lab}$  the velocity of the  ${}^6\text{Be}$  nucleus in the laboratory system. The momentum components from system K to K' system are evaluated applying a Galilean transformation through the relations:

$$P'_{ix} = P_{ix} \quad (\text{B.5})$$

$$P'_{iy} = P_{iy} \quad (\text{B.6})$$

$$P'_{iz} = P_{iz} + P_{lab}, \quad (\text{B.7})$$

where  $P'_{ix}$ ,  $P'_{iy}$  and  $P'_{iz}$  are the momentum components of each fragment in the X', Y' and Z' axes respectively and  $P_{lab}$  is the momentum of the  ${}^6\text{Be}$  in the laboratory reference frame. Again the Z' axis is considered at the same direction as  $\mathbf{P}_{lab}$ .

4. After the evaluation of the momenta in the K' system, a two-dimensional axes rotation is made in order to transform the momentum components to the laboratory system using the formulas:

$$P_{ix}^{lab} = P'_{ix} \quad (\text{B.8})$$

$$P_{iy}^{lab} = P'_{iz} \sin(\theta_{lab}) + P'_{iy} \cos(\theta_{lab}) \quad (\text{B.9})$$

$$P_{iz}^{lab} = P'_{iz} \cos(\theta_{lab}) - P'_{iy} \sin(\theta_{lab}), \quad (\text{B.10})$$

where  $P_{ix}^{lab}$ ,  $P_{iy}^{lab}$  and  $P_{iz}^{lab}$  are the momentum components of each fragment in the  $X_{lab}$ ,  $Y_{lab}$  and  $Z_{lab}$  axes respectively, while  $\theta_{lab}$  is the angle of the  ${}^6\text{Be}$  in the the laboratory frame.

Having known the momenta of the fragments in the laboratory frame, the energy  $E_i^{lab}$  and the angle  $\theta_i^{lab}$  of each fragment are obtained through the relations:

$$E_i^{lab} = \frac{(P_i^{lab})^2}{2m_i} \quad (\text{B.11})$$

$$\theta_i^{lab} = \arccos\left(\frac{P_{iz}^{lab}}{P_i^{lab}}\right), \quad (\text{B.12})$$

where  $i=[1 \rightarrow \alpha, 2 \rightarrow p_1, 3 \rightarrow p_2]$  and  $P_i^{lab}$  is the the total momentum,  $P_{iz}^{lab}$  is the momentum component in the  $Z_{lab}$  axis, and  $m_i$  is the mass of each fragment. Finally, choosing the angular range covered by our detectors, the data are sorted into energy bins with the appropriate widths and thus, we are able to construct the energy spectrum of our interest.



# Appendix C

## Tabulated cross sections

Table C.1: *Quasi-elastic scattering ratios  $\sigma/\sigma_{Ruth}$  for the system  ${}^7\text{Be} + {}^{28}\text{Si}$  at the energy of 22.0 MeV.*

| $\theta_{c.m.}$ (deg) | $\sigma/\sigma_{Ruth}$ | Error  |
|-----------------------|------------------------|--------|
| 17.80                 | 1.0900                 | 0.0614 |
| 19.91                 | 1.1102                 | 0.0639 |
| 22.01                 | 1.1018                 | 0.0649 |
| 24.11                 | 1.0609                 | 0.0642 |
| 28.31                 | 0.9491                 | 0.0615 |
| 30.39                 | 0.8911                 | 0.0601 |
| 32.48                 | 0.7943                 | 0.0565 |
| 34.56                 | 0.6726                 | 0.0513 |
| 38.69                 | 0.6464                 | 0.0544 |
| 40.75                 | 0.5145                 | 0.0483 |
| 42.81                 | 0.4293                 | 0.0448 |
| 45.88                 | 0.2920                 | 0.0454 |
| 48.92                 | 0.2231                 | 0.0350 |
| 65.10                 | 0.1048                 | 0.0370 |
| 67.48                 | 0.1419                 | 0.0448 |
| 69.83                 | 0.1185                 | 0.0423 |
| 72.18                 | 0.0464                 | 0.0342 |

Table C.2: *Quasi-elastic scattering ratios  $\sigma/\sigma_{Ruth}$  for the system  ${}^7\text{Be} + {}^{28}\text{Si}$  at the energy of 19.80 MeV.*

| $\theta_{c.m.}$ (deg) | $\sigma/\sigma_{Ruth}$ | Error  |
|-----------------------|------------------------|--------|
| 17.42                 | 0.9729                 | 0.0978 |
| 21.33                 | 1.0536                 | 0.0567 |
| 26.50                 | 1.0685                 | 0.0794 |
| 30.77                 | 0.9503                 | 0.1510 |
| 37.66                 | 0.7343                 | 0.3008 |
| 42.81                 | 0.5786                 | 0.0612 |
| 46.89                 | 0.5022                 | 0.0669 |
| 65.10                 | 0.1922                 | 0.0508 |
| 67.48                 | 0.1489                 | 0.0406 |
| 69.83                 | 0.1728                 | 0.0555 |
| 72.18                 | 0.1115                 | 0.0426 |

Table C.3: *Quasi-elastic scattering ratios  $\sigma/\sigma_{Ruth}$  for the system  ${}^7\text{Be} + {}^{28}\text{Si}$  at the energy of 17.20 MeV.*

| $\theta_{c.m.}$ (deg) | $\sigma/\sigma_{Ruth}$ | Error  |
|-----------------------|------------------------|--------|
| 14.11                 | 0.9655                 | 0.0452 |
| 16.33                 | 1.0095                 | 0.0475 |
| 18.57                 | 1.0371                 | 0.0489 |
| 20.78                 | 1.0517                 | 0.0498 |
| 24.10                 | 1.0757                 | 0.0363 |
| 27.42                 | 1.0826                 | 0.0520 |
| 29.61                 | 1.0984                 | 0.0532 |
| 31.80                 | 1.1203                 | 0.0546 |
| 33.98                 | 1.0668                 | 0.0526 |
| 36.16                 | 1.0546                 | 0.0525 |
| 38.22                 | 1.0660                 | 0.0538 |
| 42.66                 | 0.9624                 | 0.0768 |
| 64.79                 | 0.4279                 | 0.0475 |
| 67.18                 | 0.3942                 | 0.0525 |
| 69.60                 | 0.3320                 | 0.0541 |
| 71.95                 | 0.2663                 | 0.0485 |
| 76.73                 | 0.2350                 | 0.0355 |

Table C.4: *Quasi-elastic scattering ratios  $\sigma/\sigma_{Ruth}$  for the system  ${}^7\text{Be} + {}^{28}\text{Si}$  at the energy of 13.20 MeV.*

| $\theta_{c.m.}$ (deg) | $\sigma/\sigma_{Ruth}$ | Error  |
|-----------------------|------------------------|--------|
| 18.86                 | 1.0000                 | 0.0164 |
| 23.06                 | 1.0206                 | 0.0202 |
| 29.35                 | 0.9935                 | 0.0270 |
| 33.52                 | 0.9610                 | 0.0327 |
| 37.66                 | 1.0172                 | 0.0414 |
| 41.78                 | 0.9879                 | 0.0496 |
| 66.34                 | 0.9900                 | 0.1560 |
| 71.00                 | 0.8945                 | 0.1558 |
| 75.80                 | 0.8110                 | 0.1532 |

Table C.5: *Differential cross sections for the total  $\alpha$ -production,  $(d\sigma_\alpha/d\Omega)_{total}^{lab}$ , for the system  ${}^7\text{Be} + {}^{28}\text{Si}$  at the energy of 22.0 MeV.*

| $\theta_{lab}$ (deg) | $(d\sigma_\alpha/d\Omega)_{total}^{lab}$ (mb/sr) | Error (mb/sr) |
|----------------------|--|---------------|
| 16.16                | 384.50   | 25.03         |
| 20.71                | 323.05   | 27.46         |
| 26.12                | 224.30   | 12.80         |
| 31.83                | 177.42   | 8.70          |
| 36.54                | 110.67   | 7.04          |
| 56.61                | 54.49  | 4.26          |
| 65.31                | 52.60  | 6.19          |
| 71.07                | 39.42  | 8.22          |
| 80.00                | 35.75  | 8.51          |
| 100.23               | 35.02  | 7.15          |
| 110.85               | 31.93  | 5.36          |
| 117.93               | 27.48  | 5.50          |
| 124.22               | 32.73  | 7.23          |

Table C.6: *Differential cross sections for the total  $\alpha$ -production,  $(d\sigma_\alpha/d\Omega)_{total}^{lab}$ , for the system  ${}^7\text{Be} + {}^{28}\text{Si}$  at the energy of 19.8 MeV.*

| $\theta_{lab}$ (deg) | $(d\sigma_\alpha/d\Omega)_{total}^{lab}$ (mb/sr) | Error (mb/sr) |
|----------------------|--|---------------|
| 16.16                | 284.06   | 24.91         |
| 20.37                | 201.82   | 28.41         |
| 25.56                | 189.31   | 11.36         |
| 31.45                | 137.99   | 9.37          |
| 37.08                | 101.60   | 11.66         |
| 57.64                | 51.70  | 7.23          |
| 65.31                | 38.85  | 6.29          |
| 74.16                | 32.75  | 6.11          |
| 80.00                | 29.50  | 13.37         |
| 100.99               | 25.84  | 12.83         |
| 109.34               | 32.33  | 10.66         |
| 116.42               | 23.23  | 8.15          |

Table C.7: *Differential cross sections for the total  $\alpha$ -production,  $(d\sigma_\alpha/d\Omega)_{total}^{lab}$ , for the system  ${}^7\text{Be} + {}^{28}\text{Si}$  at the energy of 13.2 MeV.*

| $\theta_{lab}$ (deg) | $(d\sigma_\alpha/d\Omega)_{total}^{lab}$ (mb/sr) | Error (mb/sr) |
|----------------------|--|---------------|
| 15.47                | 62.30  | 21.73         |
| 23.80                | 57.40  | 7.07          |
| 28.75                | 31.58  | 9.99          |
| 38.88                | 35.61  | 5.57          |
| 69.00                | 6.40   | 1.94          |
| 111.00               | 4.15   | 1.45          |

Table C.8: *Differential cross sections for the  $\alpha$ -production due to direct processes,  $(d\sigma_\alpha/d\Omega)_{direct}^{lab}$ , for the system  ${}^7\text{Be} + {}^{28}\text{Si}$  at the energy of 22.0 MeV.*

| $\theta_{lab}$ (deg) | $(d\sigma_\alpha/d\Omega)_{direct}^{lab}$ (mb/sr) | Error (mb/sr) |
|----------------------|---|---------------|
| 16.16                | 290.73  | 18.92         |
| 20.71                | 236.97  | 20.14         |
| 26.12                | 149.30  | 8.52          |
| 31.83                | 108.50  | 5.32          |
| 36.54                | 47.96   | 3.05          |
| 56.61                | 10.25   | 0.80          |
| 65.31                | 11.41   | 1.34          |
| 71.07                | 1.89  | 0.39          |
| 80.00                | 1.25  | 0.30          |

Table C.9: *Differential cross sections for the  $\alpha$ -production due to direct processes,  $(d\sigma_\alpha/d\Omega)_{direct}^{lab}$ , for the system  ${}^7\text{Be} + {}^{28}\text{Si}$  at the energy of 19.8 MeV.*

| $\theta_{lab}$ (deg) | $(d\sigma_\alpha/d\Omega)_{direct}^{lab}$ (mb/sr) | Error (mb/sr) |
|----------------------|---|---------------|
| 16.16                | 205.21  | 18.00         |
| 20.37                | 127.32  | 17.92         |
| 25.56                | 122.63  | 7.36          |
| 31.45                | 79.78   | 5.42          |
| 37.08                | 50.74   | 5.82          |
| 57.64                | 16.36   | 2.29          |
| 65.31                | 6.85  | 1.11          |
| 74.16                | 2.60  | 0.49          |
| 80.00                | 0.50  | 0.23          |

Table C.10: *Differential cross sections for the  $\alpha$ -production due to direct processes,  $(d\sigma_\alpha/d\Omega)_{direct}^{lab}$ , for the system  ${}^7\text{Be} + {}^{28}\text{Si}$  at the energy of 13.2 MeV.*

| $\theta_{lab}$ (deg) | $(d\sigma_\alpha/d\Omega)_{direct}^{lab}$ (mb/sr) | Error (mb/sr) |
|----------------------|---|---------------|
| 15.47                | 55.19   | 19.25         |
| 23.80                | 50.55   | 6.23          |
| 28.75                | 25.28   | 8.00          |
| 38.88                | 30.27   | 4.74          |
| 69.00                | 2.32  | 0.93          |

Table C.11: *Differential cross sections for the  ${}^3\text{He}$ -production,  $(d\sigma_{{}^3\text{He}}/d\Omega)_{lab}$ , for the system  ${}^7\text{Be} + {}^{28}\text{Si}$  at the energy of 22.0 MeV.*

| $\theta_{lab}$ (deg) | $(d\sigma_{{}^3\text{He}}/d\Omega)_{lab}$ (mb/sr) | Error (mb/sr) |
|----------------------|---|---------------|
| 16.16                | 98.22   | 10.75         |
| 20.71                | 72.80   | 13.31         |
| 26.12                | 56.30   | 9.32          |
| 31.83                | 39.57   | 6.72          |
| 37.28                | 26.57   | 2.94          |
| 55.58                | 12.70   | 2.33          |
| 61.26                | 8.31  | 2.49          |
| 67.97                | 4.93  | 1.45          |

Table C.12: *Differential cross sections for the  ${}^3\text{He}$ -production,  $(d\sigma_{{}^3\text{He}}/d\Omega)_{lab}$ , for the system  ${}^7\text{Be} + {}^{28}\text{Si}$  at the energy of 19.8 MeV.*

| $\theta_{lab}$ (deg) | $(d\sigma_{{}^3\text{He}}/d\Omega)_{lab}$ (mb/sr) | Error (mb/sr) |
|----------------------|---|---------------|
| 16.16                | 100.23  | 24.89         |
| 24.39                | 72.98   | 19.39         |
| 28.70                | 45.76   | 8.69          |
| 32.77                | 30.95   | 4.51          |
| 37.72                | 30.86   | 5.31          |
| 55.16                | 9.31  | 2.56          |
| 61.26                | 5.52  | 2.77          |

Table C.13: *Differential cross sections for the  ${}^3\text{He}$ -production,  $(d\sigma_{{}^3\text{He}}/d\Omega)_{lab}$ , for the system  ${}^7\text{Be} + {}^{28}\text{Si}$  at the energy of 13.2 MeV.*

| $\theta_{lab}$ (deg) | $(d\sigma_{{}^3\text{He}}/d\Omega)_{lab}$ (mb/sr) | Error (mb/sr) |
|----------------------|---|---------------|
| 17.73                | 20.73   | 7.24          |
| 23.49                | 15.46   | 6.64          |
| 34.12                | 16.13   | 4.01          |

# Appendix D

## Error calculation formulas

The ratios  $\sigma/\sigma_{Ruth}^{Si}$  were deduced according to the following expression:

$$R \equiv \frac{\sigma}{\sigma_{Ruth}^{Si}} = \frac{N_{Si}}{N_{Pb}} * K, \quad (D.1)$$

where  $N_{Si}$  and  $N_{Pb}$  are the event by event counts corresponding to every strip collected with the silicon and lead targets respectively and  $K$  is a constant which was determined assuming that at small scattering angles the ratio  $\sigma/\sigma_{Ruth}^{Si}$  between elastic scattering cross sections and Rutherford cross sections is  $\sim 1.0$ . Using the error propagation formula [142], the error in the ratio is calculated as follows:

$$\begin{aligned} \Sigma &= \pm \sqrt{\left(\frac{\partial R}{\partial N_{Si}} \Sigma_{N_{Si}}\right)^2 + \left(\frac{\partial R}{\partial N_{Pb}} \Sigma_{N_{Pb}}\right)^2} \\ \Sigma &= \pm \sqrt{\left(\frac{K}{N_{Pb}} \sqrt{N_{Si}}\right)^2 + \left(-\frac{N_{Si}K}{N_{Pb}^2} \sqrt{N_{Pb}}\right)^2} \\ \Sigma &= \pm \sqrt{\left(\frac{N_{Si}}{N_{Pb}^2} K^2\right) + \left(\frac{N_{Si}^2}{N_{Pb}^3} K^2\right)} \end{aligned} \quad (D.2)$$

$$\begin{aligned}
\Sigma &= \pm \sqrt{\left(\frac{N_{Si}^2}{N_{Pb}^2} K^2 \frac{1}{N_{Si}}\right) + \left(\frac{N_{Si}^2}{N_{Pb}^2} K^2 \frac{1}{N_{Pb}}\right)} \\
\Sigma &= \pm \sqrt{\left(R^2 \frac{1}{N_{Si}}\right) + \left(R^2 \frac{1}{N_{Pb}}\right)} \\
\Sigma &= \pm R * \sqrt{\left(\frac{1}{N_{Si}}\right) + \left(\frac{1}{N_{Pb}}\right)}.
\end{aligned} \tag{D.3}$$

The differential cross sections either for  $^4\text{He}$ - or  $^3\text{He}$ - particle production were evaluated through the following expression:

$$\frac{d\sigma}{d\Omega} = \frac{N}{N_{Pb}} * K', \tag{D.4}$$

where N is either the  $^4\text{He}$  or  $^3\text{He}$  yield for each strip,  $N_{Pb}$  are the counts for each strip collected from  $^7\text{Be}$  quasi - elastic scattering to the lead target and the constant  $K'$  corresponds to

$$K' = K * \sigma_{Ruth}^{Si} \tag{D.5}$$

with K being a constant determined by the quasi - elastic scattering data as it was described in Section 3.2 and  $\sigma_{Ruth}^{Si}$  is the calculated Rutherford cross section in the laboratory reference system for the elastic scattering of  $^7\text{Be}$  on  $^{28}\text{Si}$ . Working in the same way as previously, the error in the differential reaction cross section is calculated as follows:

$$\begin{aligned}
\Sigma_{react} &= \pm \sqrt{\left(\frac{\partial\left(\frac{d\sigma}{d\Omega}\right)}{\partial N} \Sigma_N\right)^2 + \left(\frac{\partial\left(\frac{d\sigma}{d\Omega}\right)}{\partial N_{Pb}} \Sigma_{N_{Pb}}\right)^2} \\
\Sigma_{react} &= \pm \sqrt{\left(\frac{K'}{N_{Pb}} \sqrt{N}\right)^2 + \left(-\frac{NK'}{N_{Pb}^2} \sqrt{N_{Pb}}\right)^2} \\
\Sigma_{react} &= \pm \sqrt{\left(\frac{N}{N_{Pb}^2} K'^2\right) + \left(\frac{N^2}{N_{Pb}^3} K'^2\right)^2}
\end{aligned} \tag{D.6}$$

$$\begin{aligned}
\Sigma_{react} &= \pm \sqrt{\left(\frac{N^2}{N_{Pb}^2} K'^2 \frac{1}{N}\right) + \left(\frac{N^2}{N_{Pb}^2} K'^2 \frac{1}{N_{Pb}}\right)} \\
\Sigma_{react} &= \pm \sqrt{\left[\left(\frac{d\sigma}{d\Omega}\right)^2 \frac{1}{N}\right] + \left[\left(\frac{d\sigma}{d\Omega}\right)^2 \frac{1}{N_{Pb}}\right]} \\
\boxed{\Sigma_{react} &= \pm \frac{d\sigma}{d\Omega} * \sqrt{\left(\frac{1}{N}\right) + \left(\frac{1}{N_{Pb}}\right)}.}
\end{aligned}
\tag{D.7}$$



# Appendix E

## $\Delta E$ -E technique

One important aspect in experimental nuclear physics is the particle identification. During a nuclear collision, different types of reactions may occur leading to various reaction products with different masses and energies. Thus, the discrimination between different ions may be difficult due to overlaps between the energy peaks in the spectrum acquired with a single detector. A widespread technique that allows the distinction between different ions is called  $\Delta E$ -E technique. A  $\Delta E$ -E technique is adopted by using a thin detector followed by thick one (or more). This detector array is called  $\Delta E$ -E telescope. The energy deposition at the first layer of the telescope is rather small compared to that of second stage where usually the particle stops.

The  $\Delta E$ -E technique is based on the fact that the stopping power of the charged particles when they interact with matter, depends upon their atomic number  $\mathbf{Z}$  and mass  $\mathbf{M}$ . When a charged particle passes through a detector, a part of its energy is lost via electromagnetic interactions with the detector material. Thus, for a given material, the higher is the ion charge, the greater is the energy loss. The stopping power of an ion inside a detector material is evaluated via the Bethe-Block formula [84]:

$$-\frac{dE}{dx} = \frac{e^4 Z_i^2}{4\pi\epsilon_0 m_e u^2} \frac{Z_m \rho N_A}{A_m} \left[ \ln \frac{2m_e u^2}{I} - \ln \left( 1 - \frac{u^2}{c^2} \right) - \frac{u^2}{c^2} \right] \quad (\text{E.1})$$

where  $\mathbf{Z}_i$  and  $\mathbf{u}$  are the atomic number and the velocity of the incident ion respectively,  $\mathbf{Z}_m$ ,  $\mathbf{A}_m$  and  $\boldsymbol{\rho}$  are the atomic number, the atomic weight and the density of the detector material respectively,  $\mathbf{I}$  is average excitation energy of the atomic electrons,  $\mathbf{m}_e$  is the electron mass,  $\boldsymbol{\epsilon}_0$  is the vacuum permittivity and  $\mathbf{c}$  is the speed of light. It is obvious from Equation E.1 that

the energy loss increases as the square of the atomic number of the incident particle. For a non-relativistic particle, we may express the kinetic energy  $E_0$  as:

$$E_0 = \frac{1}{2}Mu^2 \quad (\text{E.2})$$

where  $M$  is the ion mass. Solving for the velocity  $u$ , Equation E.1 is reduced to

$$-\frac{dE}{dx} = K \frac{Z_i^2 M}{E_0} \left[ \ln \frac{4m_e E_0}{IM} - \ln \left( 1 - \frac{2E_0}{Mc^2} \right) - \frac{2E_0}{Mc^2} \right] \quad (\text{E.3})$$

with  $K$  being a constant for a given material. In case of a  $\Delta E$ -E telescope, the energy deposition on the first stage of the telescope with thickness  $T$  is given by the integral of the energy loss function over the detector thickness.

$$\Delta E = \int_0^T -\frac{dE}{dx} dx$$

$$\Delta E = KT \frac{Z_i^2 M}{E_0} \left[ \ln \frac{4m_e E_0}{IM} - \ln \left( 1 - \frac{2E_0}{Mc^2} \right) - \frac{2E_0}{Mc^2} \right] \quad (\text{E.4})$$

Taking into account that  $\Delta E$  is very small compared to  $E$ , we may write that:

$$(\Delta E + E)\Delta E = E_0 \Delta E$$

$$\Delta E \propto \frac{Z_i^2 M}{E} \quad (\text{E.5})$$

Based on Equation E.5, by plotting the energy loss at the first stage of the telescope as a function of the energy loss at the second stage, ions with the same atomic number and mass will lie on the same geometrical place (hyperbola). Thus, by using  $\Delta E$ -E technique we may identify the different ions produced during nuclear reactions.

